DIPLOMA THESIS

Studies on the $H \rightarrow \tau_l \tau_h$ decay mode exploiting the τ_h substructure with data from the ATLAS experiment at the LHC

Johanna Nagel

Fakultät für Mathematik und Physik
Albert-Ludwigs-Universität Freiburg

Studies on the $H \rightarrow \tau_l \tau_h$ decay mode exploiting the τ_h substructure with data from the ATLAS experiment at the LHC

Diploma Thesis

vorgelegt von

Johanna Nagel

Februar 2013

Prof. Dr. Karl Jakobs
Fakultät für Mathematik und Physik der
Albert-Ludwigs-Universität
Freiburg im Breisgau

Contents

1 Introduction

The *Standard Model* of particle physics has been developed in the second half of the 20th century. It is the foundation of elementary particle physics and describes all currently known elementary particles, like the spin-1/2 fermions which form all known matter and three of the four interactions which are mediated by spin-1 bosons. A description of gravity is not included in the Standard Model. Several predictions, like the existence of the W and Z bosons and the top quark could be confirmed by experiments until the beginning of the new century. However, the particles in the Standard Model acquire their masses through the *Higgs mechanism*. Until last year the last missing piece of the Standard Model, the existence of the *Higgs boson*, had not been confirmed.

In Summer 2012 a new bosonic resonance with a mass of 126 GeV, compatible with the Standard Model Higgs boson, was discovered independently by the ATLAS and CMS collaborations. The ATLAS and CMS experiments are located at the *Large Hadron Collider*, a circular proton-proton collider with a design energy of $\sqrt{s} = 14\,\mathrm{TeV}$. The discovery of the new boson was based on the data taken in 2011 and the first half of 2012 at center-of-mass energies of $\sqrt{s} = 7\,\mathrm{TeV}$ and $\sqrt{s} = 8\,\mathrm{TeV}$, respectively. The most sensitive search channels $H \rightarrow ZZ^* \rightarrow llll$, $H \rightarrow \gamma\gamma$ and $H \rightarrow WW^* \rightarrow l\nu l\nu$ contributed most to the discovery.

So far no observation of the new boson has been possible in the $H \rightarrow \tau^+\tau^-$ or $H \rightarrow b\bar{b}$ search channels. Nevertheless, these channels are of special interest since they are the only channels with noteworthy decay probability in which the Higgs-boson coupling to fermions can be directly probed. The Higgs-boson decay into two tau leptons has a sizeable branching ratio in the low mass region and is the only channel in which the coupling of the Higgs boson to leptons can be directly probed. But since the tau lepton is the only lepton for which the decay into hadrons is kinematically available, the final states of such decays include hadrons and neutrinos. As a result the high sensitivity of the above mentioned discovery channels cannot be reached in $H \rightarrow \tau^+\tau^-$ with the current data.

The $H \rightarrow \tau_l\tau_h$ channel, where one tau decays into an electron or muon and the corresponding neutrinos and the other tau decays into hadrons and a tau neutrino, represents a reasonable compromise between a clean signal, due to one lepton in the final state, and a high probability of occurrence. The categorization of the $H \rightarrow \tau_l\tau_h$ analysis into four categories is geared to the kinematics of possible jets in the event. This thesis aims at the improvement of the sensitivity in two channels of the $H \rightarrow \tau_l\tau_h$ analysis with low jet multiplicity, by exploiting the substructure of the hadronically decaying tau.

The hadronic decay of the tau predominantly results in pions, only a small fraction of τ_h decays into kaons. The decay into pions always results in an odd number of charged and any number of neutral pions. A special algorithm is used to aquire information about the neutral pions in a hadronic tau decay. This information is then used to build subcategories depending on the pions involved in the tau decay. The background compositions and the signal-to-background ratios of these subcategories are investigated. Expexted limits on the

Higgs-boson cross section are derived for the combination of the subcategories for Higgs-boson masses in the range from 115 to 140 GeV. Those are compared to the corresponding limits for the inclusive treatment of the pion-based subcategories. Also a new momentum variable which treats neutral pions seperately to reconstruct the transverse momentum of the tau is examined. It is investigated if this variable results in a better mass resolution when reconstructing the mass of the lepton-τ_h system.

The studies presented in this thesis are based on the data collected by the ATLAS experiment from January 2012 until mid September 2012 at a center-of-mass energy of $\sqrt{s} = 8\,\text{TeV}$. The results of these studies may be generalized to other analyses which include hadronically decaying tau leptons.

In Chapter 2 an introduction to the Standard Model of particle physics as well as an introduction to Higgs-boson physics at the LHC is given. Also the current knowledge of the Higgs boson is discussed. The ATLAS detector is briefly discussed in Chapter 3. Chapter 4 focusses on the reconstruction and identification of objects in the ATLAS detector. Also the algorithm is introduced, which is used to aquire information about neutral pions in a hadronic tau decay. In Chapter 5 an overview of the $H \longrightarrow \tau_l \tau_h$ analysis is given and its results are discussed. The studies and results on the investigation of the τ_{had} substructure are presented in Chapter 6.

2 Theoretical Background

2.1 The Standard Model of particle physics

The *Standard Model of particle physics* (SM) describes the elementary particles - the *quarks* and *leptons*, as well as the subatomic interactions mediated by the *vector bosons*. Developed in the 1960s and 1970s the SM is a quantum field theory which has proven predictive power. Following the SM predictions, the vector bosons $W^{\pm}$ and Z were discovered in the last third of the 20th century at CERN[1]. A new particle has been discovered in the summer of 2012 which is compatible with the Standard Model *Higgs boson* - the last missing particle predicted by the SM.

This chapter gives an overview of the Standard Model, its predictions and limitations. The following discussions are based on the corresponding chapters in Ref. [1].

2.1.1 Particles in the SM

The particle spectrum of the Standard Model includes *quarks* and *leptons*, which are the building blocks of matter, and the *vector bosons*, which carry the interactions. Quarks and leptons carry spin $^1/_2$ and are therefore fermions, whereas the vector bosons carry spin 1. All particles of the Standard Model are believed to be elementary.

Leptons as well as quarks appear in three generations, also called families (cf. Table 2.1). All usual matter consists of particles from the first generation. The *up* (u) and *down* (d) quarks form neutrons and protons, together with *electrons* (e) all atoms can be formed. The second and third generation leptons differ from the first, only by the mass of the particles. Whereas the electron has a mass of 0.511 MeV the *muon* (μ) mass is roughly 200 times, and the *tau* (τ) mass even about 3500 times larger than the electron mass. Each lepton is accompanied by its *neutrino* (ν). The second and third generation of quarks consist of the *charm* (c), *strange* (s), *top* (t) and *bottom*, also called *beauty* (b) quark. From those, the top quark has by far the largest mass, more than 180 times the mass of the proton. In the Standard Model the neutrinos are treated as massless particles, although the discovery of neutrino oscillations proves the opposite. However, the neutrino-mass scales are found to be very small, and do not influence the prediction power of the Standard Model [2], [3].

For each particle exists an antiparticle, which, except for identical mass and spin, has reversed additive quantum numbers.

All fermions underlie the *weak interaction*. Quarks also underlie the *strong interaction* which couples to the so called *color charge*[2]. The three additional degrees of freedom introduced

---

[1] **C**onseil **E**uropéen pour la **R**echerche **N**ucléaire - CERN: located near Geneva in Switzerland.

[2] The color charge as additional degree of freedom has been introduced with the quark model in 1964 and could explain the existence of the Δ^{++}-baryon. This particle has a spin of $^3/_2$ and therefore combines three u quarks with the same spin orientation in their ground state, which is forbidden by the Pauli principle [1]

	generation I	 II	 III	charge
leptons	e	μ	τ	1
	ν_e	ν_μ	ν_τ	0
quarks	u	c	t	+2/3
	d	s	b	-1/3

Table 2.1: Fermions of the Standard Model in three generations with corresponding electric charges. These are given in units if the electron charge $1.6 \cdot 10^{-19}$ C. The symbols are explained and referred to in the text.

by the color charge for quarks are reflected by a SU(3) symmetry group.

The *vector bosons* of the Standard Model correspond to the interactions, and are also considered to be elementary. The *photon* (γ), *gluon* (g) and *W* ($W^{\pm}$) and *Z-boson* (Z) are the mediators of the *electro magnetic-*, *strong-* and *weak interactions*, respectively. Whereas the photon and the gluons are massless, the W and Z bosons are found to have the masses $m_W = 80.385 \pm 0.015\,\mathrm{GeV}$ and $m_Z = 91.1876 \pm 0.0021\,\mathrm{GeV}$ [4]. Those masses as well as the masses of leptons and quarks, can be explained by introducing a so called *Higgs field*. This leads to a spontaneous symmetry breaking which is discussed in more detail in Section 2.1.3.

2.1.2 Fundamental interactions in the SM

The fundamental interactions of the Standard Model are described mathematically using *quantum field theory* and applying *gauge symmetries*. In Lagrangian field theory, particles correspond to excited states of quantum fields and the creation and annihilation of particles is described by operators. Interactions are dictated by local gauge symmetries, which implicates the local conservation of physical quantities[3].
In order to achieve local gauge invariance, the *Lagrangian* $\mathscr{L}$ has to be invariant under the transformation

$$\Psi(x) \to e^{\imath\alpha(x)}\Psi(x), \tag{2.1}$$

where $\alpha(x)$ is a real parameter changing over space time and Ψ represents a spinor, a doublet or a triplet of spinors for the U(1), SU(2) and SU(3) groups, respectively.
The following sections concentrate on the description of how local gauge invariance, with respect to the U(1), SU(2) and SU(3) group or combinations of the latter, can be achieved.

Quantum electrodynamics - QED

The concept of restoring the local gauge invariance by introducing a gauge field shall be explained on *quantum electrodynamics* as an example. In the case of QED, the local phase

---

[3] Resulting from the *Noether theorem*

transformation introduced in equation 2.1 form the unitary abelian group[4] U(1). The goal of this section is therefore, to derive the Lagrangian $\mathscr{L}_{QED}$ which describes the QED interaction and is invariant under rotations in the U(1) space.
Resulting from the Dirac equation[5], the Lagrangian of a free fermion with mass m can be written as:

$$\mathscr{L} = \imath\bar{\psi}(\gamma^\mu\partial_\mu - m)\psi, \tag{2.2}$$

where ψ ($\bar{\psi}$) is the (adjoint) Dirac spinor of a spin 1/2 field and γ^μ are the Dirac matrices [5]. However, the Lagrangian $\mathscr{L}$ of equation 2.2 is not invariant under the phase transformation 2.1:

$$\mathscr{L}' = \imath\bar{\psi'}(\gamma^\mu\partial_\mu - m)\psi' \tag{2.3}$$

$$= \mathscr{L} - \bar{\psi}\gamma^\mu\psi\partial_\mu\alpha(x) \neq \mathscr{L}. \tag{2.4}$$

The local gauge invariance can be restored by replacing ∂_μ with the modified derivative D_μ that includes a massless gauge field A_μ which transforms according to the *gauge transformation*:

$$\partial_\mu \to D_\mu = \partial_\mu + \imath e A_\mu \qquad \text{with} \qquad A_\mu \to A'_\mu = A_\mu - \frac{1}{e}\partial_\mu\alpha(x) \tag{2.5}$$

$$\Rightarrow \qquad \mathscr{L} \overset{\partial_\mu\to D_\mu}{=} \bar{\psi}(\imath\gamma^\mu\partial_\mu - m)\psi + e\bar{\psi}\gamma^\mu\psi A_\mu. \tag{2.6}$$

Now, $\mathscr{L}$ is invariant under local gauge transformations however, $\mathscr{L}$ in 2.6 lacks physical interpretation. In order to identify A_μ as the physical photon field, a kinetic energy term which has to be invariant under local U(1) phase transformations as well, must be added. The term $\frac{1}{4}F_{\mu\nu}F^{\mu\nu}$ with the field strength tensor $F_{\mu\nu} = \partial_\mu A_\nu - \partial_\nu A_\mu$ fulfills this requirement.
Adding the *charge operator Q* to account for the different charges of leptons and quarks, the Lagrangian of QED reads as:

$$\mathscr{L}_{QED} = \imath\bar{\psi}(\gamma^\mu\partial_\mu - m)\psi + eQ\bar{\psi}\gamma^\mu\psi A_\mu - \frac{1}{4}F_{\mu\nu}F^{\mu\nu}. \tag{2.7}$$

The achieved local gauge invariance would break down again by introducing a mass term $\frac{1}{2}m^2A_\mu A^\mu$, therefore the gauge particle of the photon field - the photon - must be massless and the range of the photon field infinite.

Quantum Chromodynamic - QCD

The theory of *quantum chromodynamics* describes the strong interaction, which affects quarks and gluons. The QCD is represented by the non-abelian SU(3) group[6] and Ψ represents a triplet of Dirac spinors ψ_i. Due to SU(3), quarks and gluons have three additional degrees

---

[4] The group multiplication of an abelian group is commutative: $U(\alpha_1)U(\alpha_2) = U(\alpha_2)U(\alpha_1)$

[5] Dirac equation of a free spin-1/2 particle with mass m: $\imath\partial_\mu\gamma^\mu\Psi = m\Psi$ [1]

[6] SU(3) is non-abelian because not all T_a commute with each other: $[T_a, T_b] = \imath f_{abc}T_c$ where f_{abc} are structure constants ($f_{abc} \in \mathbb{R}$)

of freedom which are identified with the concept of colorcharge. The components ψ_i of Ψ correspond to three color fields:

$$\Psi = \begin{pmatrix} \psi_R \\ \psi_G \\ \psi_B \end{pmatrix}. \tag{2.8}$$

In contrary to QED eight gauge fields G^a_μ have to be introduced to restore the symmetry under the phase transformation $\Psi(x) \rightarrow e^{\imath\alpha_a(x)T_a}\Psi(x)$ because of the structure of the SU(3) group[7]. The final gauge invariant Lagrangian for the interaction between quarks ψ and gluons G_μ can be written as:

$$\mathscr{L}_{QCD} = \bar{\Psi}(\imath\gamma^\mu\partial_\mu - m)\Psi - g(\bar{\Psi}\gamma^\mu T_a\Psi)G^a_\mu - \frac{1}{4}G^a_{\mu\nu}G^{\mu\nu}_a, \tag{2.9}$$

where g is a free parameter of the theory and T^a the generator of the $SU(3)$ group. As in QED, g can be identified as coupling constant of the strong interaction, which has to be measured. As in QED, a mass term would lead to a collapse of the gauge symmetry, thus gluons are massless particles.

The field strength tensor $G^a_{\mu\nu}$ in 2.9 has a more complicated structure than $F_{\mu\nu}$ of QED:

$$G^a_{\mu\nu} = \partial_\mu G^a_\nu - \partial_\nu G^a_\mu - g f_{abc} G^b_\mu G^c_\nu. \tag{2.10}$$

Equation 2.10 shows that the energy is not purely kinetic but also includes an induced self-interaction between the gauge bosons, therefore gluons must also carry color charge, otherwise they would not be able to couple to each other. Another consequence of color charged gluons, is the so called *(color) confinement*, which makes it impossible to observe quarks as free particles.

2.1.3 Electroweak symmetry breaking

The combination of electromagnetic and weak interaction is often referred to as the *electroweak unification*. The interaction particles of the *weak interaction*, are the massive gauge bosons $W^\pm$ and Z. Which stand in contrast to the results of the two previous sections, where it was shown that the symmetry would be broken by introducing mass terms. In the following it is shown, how massive gauge bosons can be generated by the principle of *spontaneous electroweak symmetry breaking* and the *Higgs mechanism*.

The electroweak gauge theory is based on the SU(2)×U(1) group. In this gauge theory the left-handed particles are arranged in doublets $\Psi = \chi_L$:

$$\chi_{q,L} = \begin{pmatrix} u \\ d \end{pmatrix}_L \qquad \text{and} \qquad \chi_{l,L} = \begin{pmatrix} \nu_l \\ l^- \end{pmatrix}_L \tag{2.11}$$

---

[7] $\Psi(x) \rightarrow e^{\imath\alpha_a(x)T_a}\Psi(x)$ where T_a correspond to the *Gell-Mann matrices* and $a = 1,\ldots,8$. The Gell-Mann matrices are documented in Ref. [5, p. 282].

whereas the right-handed particles are represented by singlets $\Psi = \psi_R$:

$$\psi_{u,R},\ \psi_{d,R},\ \psi_{l^-,R}. \tag{2.12}$$

The notation u and d refers to the up- and down-type quarks respectively, l represents the three charged leptons e, μ and τ and ν_l the corresponding neutrino. The modified covariant derivative D_μ now includes two gauge fields, W_μ and B_μ from which W_μ only acts on left-handed particles:

$$D_\mu\chi_L = (\partial_\mu + \imath g W_\mu + \imath g' Y_L B_\mu)\chi_L, \qquad D_\mu\psi_R = (\partial_\mu + \imath g' Y_R B_\mu)\psi_R. \tag{2.13}$$

The notation Y has been used for the hypercharge operator. The left-handed doublets χ_L and right-handed singlets ψ_R undergo the gauge transformations

$$\chi_L \to \chi'_L = e^{\imath Y_L \beta(x)} e^{\imath T_i \theta^i(x)} \chi_L, \tag{2.14}$$

$$\psi_R \to \psi'_R = e^{\imath Y_R \beta(x)} \psi_R, \tag{2.15}$$

where $T^i = \sigma^i/2$, $i = 1,2,3$, with the Pauli matrices[8] σ^i, represent the generators of the SU(2) group[9]. The gauge parameters $\theta^i(x)$ and $\beta(x)$ are connected to three SU(2) gauge bosons W^i_μ and one U(1) gauge boson B_μ. The massless gauge bosons W^i_μ and B_μ transform as

$$B_\mu \to B'_\mu = B_\mu - \frac{1}{g'}\partial_\mu\beta, \tag{2.16}$$

$$W_\mu \to W'_\mu = U_L W_\mu U_L^\dagger + \frac{1}{g}(\partial_\mu U_L)U_L^\dagger, \tag{2.17}$$

where the notations $W_\mu = W^i_\mu T^i$ and $U_L = e^{\imath T_i \theta^i(x)}$ have been used. The kinetic energy term $-\frac{1}{4}F^{\mu\nu}F_{\mu\nu}$-$\frac{1}{4}G^{i\mu\nu}G^i_{\mu\nu}$ with

$$G^i_{\mu\nu} = \partial_\mu W^i_\nu - \partial_\nu W^i_\mu - g\varepsilon^{ijk}W^j_\mu W^k_\nu, \tag{2.18}$$

$$F_{\mu\nu} = \partial_\mu B_\nu - \partial_\nu B_\mu \tag{2.19}$$

is invariant under SU(2)×U(1) transformations. This yields the Lagrangian $\mathscr{L}_{EW}$ of the electroweak interaction including the massless gauge fields W_μ and B_μ:

$$\mathscr{L}_{EW} = \imath\bar{\chi}^n_L\gamma_\mu\left(\partial_\mu + \imath g T^i W^i_\mu + \imath g' Y B_\mu\right)\chi^n_L + \imath\bar{\psi}^m_R\gamma_\mu\left(\partial_\mu + \imath g' Y B_\mu\right)\chi^m_R - \frac{1}{4}F_{\mu\nu}F^{\mu\nu} - \frac{1}{4}G^{i\mu\nu}G^i_{\mu\nu}, \tag{2.20}$$

where the indices n and m implicate the summation over the isospin doublets and singulets of the three fermion families.

---

[8] Pauli matrices are listed in Ref. [5]

[9] The T^i do not commute: $\left[T^i, T^j\right] = \imath\varepsilon^{ijk}T^k$

The Higgs mechanism

As mentioned before, introducing a mass term for bosons to the Lagrangian by hand would destroy the local gauge symmetry. The introduction of fermion masses by hand is also not possible for slightly different reasons, as explained later. However, the local gauge invariance can be preserved by adding a SU(2) doublet of complex scalar fields ϕ with hypercharge $Y(\phi) = +1/2$ having the potential $V(\phi)$:

$$\Phi = \frac{1}{\sqrt{2}} \begin{pmatrix} \phi_1 + \imath\phi_2 \\ \phi_3 + \imath\phi_4 \end{pmatrix}, \qquad V(\phi) = \frac{1}{2}\mu^2\phi^*\phi + \frac{1}{4}\lambda(\phi^*\phi)^2. \tag{2.21}$$

The form of the potential $V(\phi)$ strongly depends on the values of μ and λ. For $\mu^2 > 0$, ϕ corresponds to a scalar field with mass μ, that is self interacting with coupling λ and has a ground state $\phi_0 = 0$ which is gauge invariant. However, the potential $V(\phi)$ looks different for $\mu^2 < 0$ and $\lambda > 0$. In this case, $\phi = 0$ does not correspond to the ground state, but an unstable local maximum as shown in Fig. 2.1. Although the new ground state is not invariant under local gauge transformations, the symmetries of the lagrangian are preserved - the symmetry has been spontaneously broken. The generation of the vector boson masses is shown with the concept of the *Higgs mechanism.*

The new ground state can be arbitrarily chosen from the multifold of degenerate states around the bottom of the potential $V(\phi)$:

$$\phi_0 = \frac{1}{\sqrt{2}} \begin{pmatrix} 0 \\ v \end{pmatrix}, \qquad v = \sqrt{-\frac{\mu^2}{\lambda}}, \tag{2.22}$$

where v is the so called *vacuum expectation value* (VEV).

Fluctuations of the vacuum can be expressed by a massive scalar field with mass $m_H = \sqrt{2\lambda}\mu$ - the *Higgs field* $h(x)$ and three massless scalar fields[10]. ϕ can be expressed by

$$\phi = \frac{1}{\sqrt{2}} \begin{pmatrix} 0 \\ v + h(x) \end{pmatrix}. \tag{2.23}$$

The Lagrangian of the scalar Higgs field is given by

$$\mathscr{L}_{Higgs} = (D^\mu\phi)^\dagger(D^\mu\phi) - V(\phi), \tag{2.24}$$

where the covariant derivative D_μ includes the SU(2)$_L$ and U(1)$_Y$ gauge bosons, W_μ and B_μ. Three and four point interactions between the gauge and scalar fields are given by the square of D_μ, with D_μ being:

$$D_\mu\phi = \left(\partial_\mu + \imath g T^i W^i_\mu + \imath\frac{1}{2}g' B_\mu \right)\phi. \tag{2.25}$$

The generation of the gauge boson masses comes from the VEV, so it is sufficient to neglect any $h(x)$ related terms in $(D^\mu\phi)^\dagger(D^\mu\phi)$. Using the structure of the Pauli matrices ($T^i = \sigma^i/2$), this yields

---

[10] These massless scalar fields are also called *Goldstone bosons*

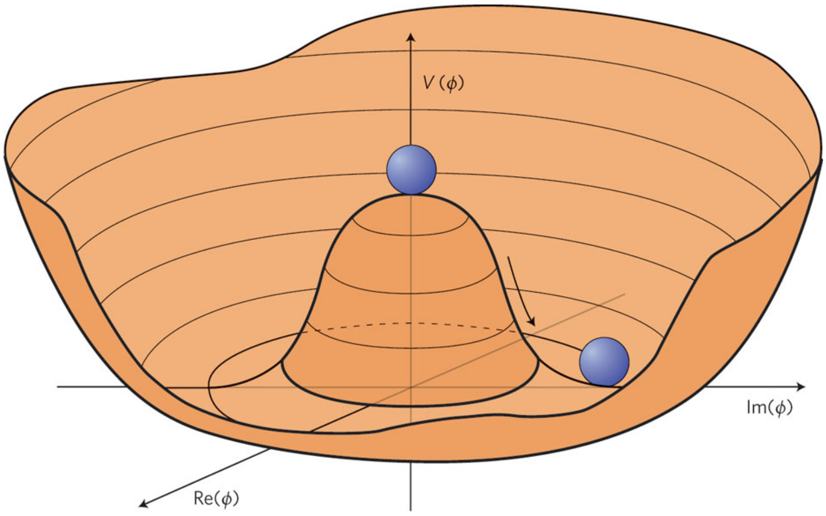

Figure 2.1: Graphical representation of the potential $V(\phi) = \frac{1}{2}\mu^2\phi\phi* + \frac{1}{4}\lambda(\phi\phi*)^2$ for $\mu^2 < 0$ and $\lambda > 0$. The ground state is represented by an arbitrarily chosen point around the bottom of the *mexican hat potential*. The arrow indicates the direction of the quantum fluctuations oscillating between the center and the side of the hat, which correspond to the Higgs boson. [6]

$$
\begin{aligned}
(D^\mu\phi_0)^\dagger(D^\mu\phi_0) &= \left|\left(\partial_\mu + \imath g T^i W^i_\mu + \imath g' Y B_\mu\right)\frac{1}{\sqrt{2}}\begin{pmatrix}0\\ v\end{pmatrix}\right|^2 && (2.26)\\
&= \frac{1}{8}(v,0)\left|\begin{pmatrix}\imath g' B_\mu - \imath g W^3_\mu & -\imath g\left(W^1_\mu - \imath W^2_\mu\right)\\ -\imath g\left(W^1_\mu + \imath W^2_\mu\right) & \imath g' B_\mu + \imath g W^3_\mu\end{pmatrix}\right|^2\begin{pmatrix}0\\ v\end{pmatrix} && (2.27)\\
&= \frac{v^2}{8}\left[g^2\left(\left(W^1_\mu\right)^2 + \left(W^2_\mu\right)^2\right) + \left(g W^3_\mu - g' B_\mu\right)^2\right]. && (2.28)
\end{aligned}
$$

The first term in 2.28 can be rewritten as

$$
\frac{v^2}{8}g^2\left(\left(W^1_\mu\right)^2 + \left(W^2_\mu\right)^2\right) = \frac{1}{2}\left(\frac{gv}{2}^2\right)W^\dagger_\mu W^\mu, \tag{2.29}
$$

with two charged vector bosons

$$
W^\pm_\mu = \frac{1}{\sqrt{2}}\left(W^1_\mu \mp \imath W^2_\mu\right) \tag{2.30}
$$

fulfilling the requirement 2.29. Therefore two charged gauge bosons arise from 2.28 with the same mass

$$
m_W = \frac{gv}{2}. \tag{2.31}
$$

After diagonalizing the matrix in 2.27, the second term in 2.28 can be identified with the neutral vector boson field Z_μ and the photon field A_μ with the corresponding masses:

$$Z_\mu = \frac{1}{\sqrt{g^2+g'^2}}\left(gW^3_\mu - g'B_\mu\right) \qquad m_Z = \frac{v}{2}\sqrt{g^2+g'^2} \tag{2.32}$$

$$A_\mu = \frac{1}{\sqrt{g^2+g'^2}}\left(gW^3_\mu + g'B_\mu\right) \qquad m_A = 0. \tag{2.33}$$

The last step on the way to the final Lagrangian of the Standard Model $\mathscr{L}_{SM}$ is the generation of the fermion masses. The introduction of a mass term of the form $-m\bar{\psi}\psi$ is excluded to maintain Lorentz invariance and local gauge invariance at the same time. But now the SU(2)× U(1) invariant Lagrangian for leptons can be expressed by

$$\mathscr{L}_l = -\lambda_n \bar{\chi}^n_{l,L}\phi\,\psi^n_{l,R} - \lambda_n \bar{\psi}^n_{l,R}\phi\,\chi^n_{l,L}, \tag{2.34}$$

where λ_n with $n = 1,\cdots,3$ stands for the *Yukawa* coupling of the leptons $l = e,\ \mu,\ \tau$ and $\chi_{l,L}$ and ψ_{lR} are the isospin doublets and singlets introduced in 2.11 and 2.12 respectively. To form the Lagrangian for quarks, the massive upper members of the isospin doublets have to be taken into account. This can be achieved by introducing a new Higgs doublet ϕ_C of complex scalar fields:

$$\phi_{C,i} = \delta_{ij}\phi^*_j \underset{breaking}{\longrightarrow} \frac{1}{\sqrt{2}}\begin{pmatrix} v+h(x) \\ 0 \end{pmatrix}, \tag{2.35}$$

where δ_{ij} is the *Kronecker delta* and i, j correspond to the two components of the spinor ϕ. Although ϕ_C has opposite hypercharge $(Y(\phi_C) = -1/2)$, it transforms precisely like ϕ due to the characteristics of the SU(2) group. The quark Lagrangian then can be written as

$$\mathscr{L}_q = -\lambda^{mn}_{q,down}\bar{\chi}^n_{q,L}\phi\,\psi^m_{q,R} - \lambda^{mn}_{q,up}\bar{\chi}^n_{q,L}\phi_C\,\psi^m_{q,R} + h.c. \tag{2.36}$$

where λ^{mn}_q represents the Yukawa couplings of quarks, and $m,n = 1,\ldots,N$ give the number of quark doublets ($N_i = 3$) and quark singlets ($N_j = 6$) respectively.
To generate the fermion masses, it is again sufficient to probe the effect of the Yukawa Lagrangian on the ground state ϕ_0:

$$\mathscr{L}_{Yukawa}(\phi_0) = \mathscr{L}_l(\phi_0) + \mathscr{L}_q(\phi_0) \tag{2.37}$$

$$= \frac{f^n_l v}{\sqrt{2}}\left(\bar{l}^n_L l^n_R + \bar{l}^n_R l^n_L\right) + \frac{f^{nm}_{q_u} v}{\sqrt{2}}\left(\bar{u}^n_L u^n_R + \bar{u}^n_R u^n_L\right) + \frac{f^{nm}_{q_d} v}{\sqrt{2}}\left(\bar{d}^m_L d^m_R + \bar{d}^m_R d^m_L\right), \tag{2.38}$$

where l, u and d refer to the leptons, up- and down-type quarks respectively. The diagonalization of the matrix f^{nm} leads to the *CKM matrix* which links the quark mass eigenstates to the electroweak eigenstates. The fermion masses can now be read off:

$$m_{f_i} = -\frac{f_i v}{\sqrt{2}}. \tag{2.39}$$

The final Lagrangian of the Standard Model therefore is

$$\mathscr{L}_{SM} = \mathscr{L}_{QCD} + \mathscr{L}_{EW} + \mathscr{L}_{Higgs} + \mathscr{L}_{Yukawa}. \tag{2.40}$$

Although it is possible to generate masses for the vector bosons and include mass terms for fermions, the minimal choice of a Higgs doublet does neither allow the prediction of these masses nor of the Higgs mass. It only gives relations of the masses to the vacuum expectation value v.
The masses of the vector bosons and fermions have been measured, but the Higgs-boson mass m_H remains the last free parameter of the Standard Model. In Summer of 2012 a new particle has been discovered which is, with the current knowledge, compatible to the Standard Model Higgs boson (see Section 2.3) [1] [7] [8].

2.2 Higgs-boson physics at the LHC

In contrary to its predecessor[11] the *Large Hadron Collider* (LHC) uses proton-proton collisions to probe the Standard Model and physics beyond. Other than electrons, protons are composite particles. Therefore, collisions in an electron-positron collider have a fixed *center of mass energy* $\sqrt{s}$ whereas collisions in a proton-proton collider have a center of mass energy $\sqrt{\hat{s}} = \sqrt{s x_i x_j}$ depending on the momentum fractions $x_{i,j}$ of the parton collision. This grants observations of collisions over a wide range of energies.

2.2.1 Phenomenology of pp collisions

This section focusses on the phenomenology of proton-proton collisions, more details on the LHC and the ATLAS experiment are given in Chapter 3.
Two opposite running beams are accelerated at the LHC. The protons are concentrated in bunches which are brought to collisions every 50 ns at designated interaction points. Especially interesting are inelastic scattering processes which result in many other particles.
In order to describe scattering processes certain quantities have to be introduced. The *cross section* σ is a measure for the probability of a certain scattering process. It has the dimension of an area and is usually given in *barn* ($1\text{b} = 10^{-28}\,\text{m}^2$). The number of interactions per unit time and per unit area is given by the *instantaneous luminosity* $\mathscr{L}$. The total number of events N for a certain process can be predicted with the cross section σ and the *integrated Luminosity* $\int \mathscr{L} dt$ by

$$N = \sigma \int \mathscr{L} dt. \tag{2.41}$$

For a circular accelerator $\mathscr{L}$ can be calculated with

$$\mathscr{L} = f_r \frac{n_b N_1 N_2}{A}, \tag{2.42}$$

using the rotation frequency f_r, the number of bunches per beam n_b, the number of particles in a bunch of beam i N_i and the transverse area of the beams A.
The Standard Model gives the theoretical background to compute the cross section σ for a certain process. But since the proton is a composite particle, its structure has to be modeled. In addition to the valence quarks (uud), which determine the quantum numbers of the proton, it consists of sea quarks of all flavors and gluons. This composition is modeled by the

---

[11] **L**arge **E**lectron **P**ositron Collider (LEP)

parton distribution functions (PDFs) which have been measured by various experiments. The probability to find a parton q_i with a momentum fraction x_i of the total proton momentum in a collision with a momentum transfer Q^2 is given by the PDF $f_{q_i}(x_i, Q^2)$.

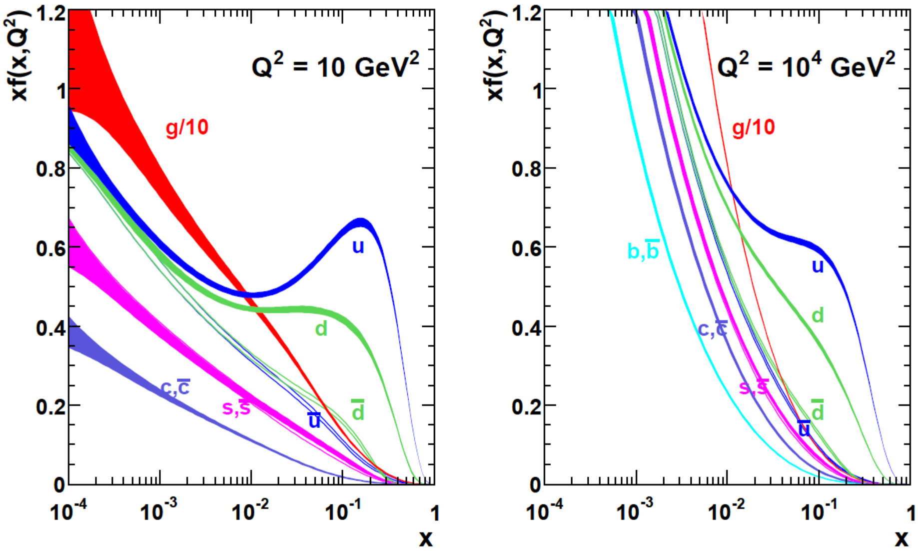

Figure 2.2: NLO parton distribution functions for a momentum transfer of $Q^2 = 10\,GeV^2$ (left) and $Q^2 = 10^4\,GeV^2$ (right). Shown are the PDFs of the valence quarks (u and d), the sea quarks and the gluons. The uncertainty of the PDFs is described by the width of the curves. [9]

The probability of scattering processes including sea quarks or gluons rises with Q^2. The PDFs of the partons for two different values of Q^2 are shown in Fig. 2.2.

In general, the valence quarks dominate the proton for high momentum fractions x_i, whereas the proton is dominated by gluons for small x-values. The sea quarks are only of noteworthy importance for smaller x-values. However, their contribution at low x-values rises strongly for high momentum transfers Q^2 (see Fig. 2.2, right).

Since the hard scattering process happens between two partons of the protons, the cross section $\hat{\sigma}$ of the partonic process has to be known in order to calculate the cross section σ of the proton-proton interaction. The cross section $\hat{\sigma}(q_i q_j \rightarrow X)$ of the partonic process resulting in the final state X can be extended to describe the process $pp \rightarrow X$ by weighing $\hat{\sigma}$ with the corresponding PDFs:

$$\sigma(pp \rightarrow X) = \sum_{ij} \int dx_i dx_j f_{q_i}(x_1, Q^2) f_{q_j}(x_j, Q^2) \hat{\sigma}(q_1 q_j \rightarrow X). \tag{2.43}$$

The cross sections for various production modes at the LHC are shown in Fig. 2.3.

2.2.2 Higgs-boson production at the LHC

Several processes lead to the production of a Higgs boson at the LHC. The Feynman diagrams of the four most important processes and their cross sections as a function of the Higgs-boson mass m_H are shown in Fig. 2.4 and 2.5, respectively. They are discussed briefly in the following.

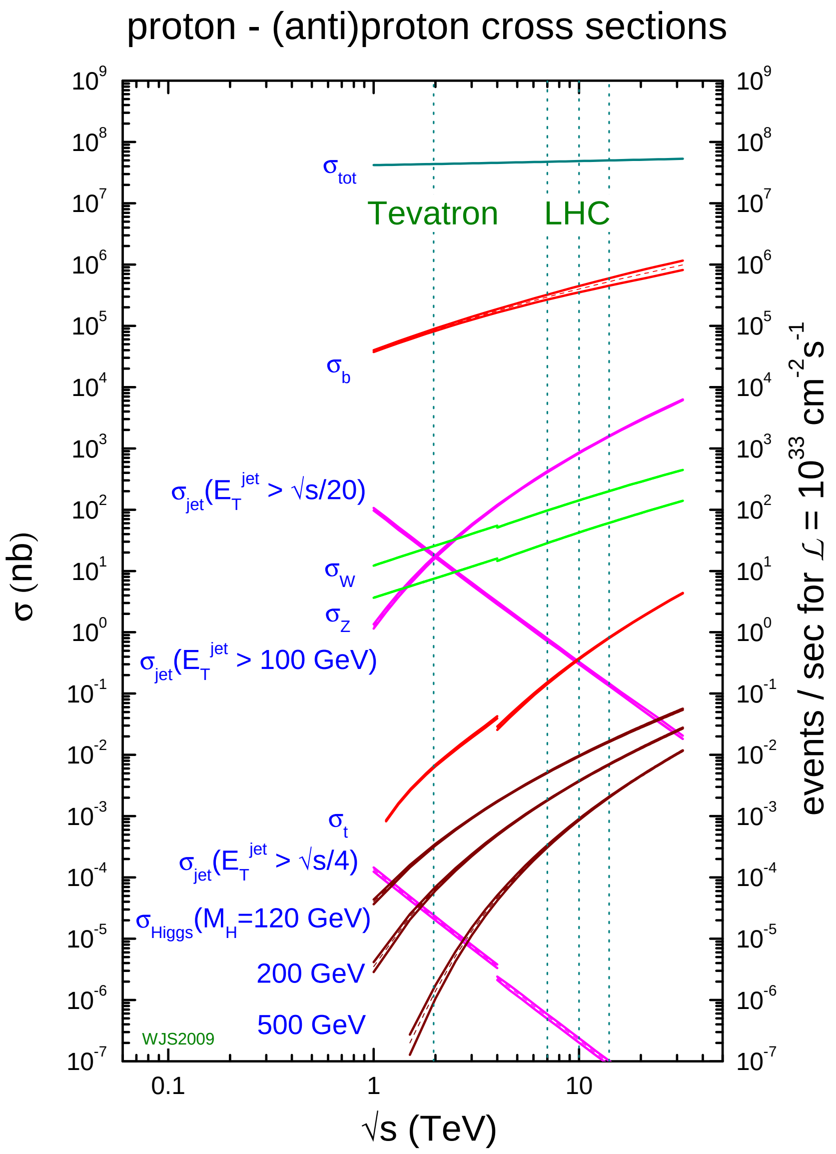

Figure 2.3: Cross sections (in nb, left axis) and number of events produced per second (right axis) for a luminosity of $\mathscr{L} = 10^{33}\,\mathrm{cm}^{-2}\,\mathrm{s}^{-1}$ in proton-(anti)proton collisions are shown for various processes. The center of mass energies $\sqrt{s} = 1.98\,\mathrm{TeV}$ (Tevatron), $\sqrt{s} = 7\,\mathrm{TeV}$ (LHC, run 2011) and $\sqrt{s} = 14\,\mathrm{TeV}$ (LHC, design $\sqrt{s}$) are represented by dashed vertical lines. At $\sqrt{s} = 10\,\mathrm{TeV}$ a line is drawn for comparison. Shown in brown are the cross sections for the Higgs boson production for different masses m_H [10].

The highest cross section of all Higgs-boson production modes has the *gluon fusion* process (ggF). When produced via ggF, the Higgs boson is fused through a quark loop. The top loop contribution is dominant, since the Higgs boson coupling is proportional to the mass of a particle (Fig. 2.4 (a)). In the *vector-boson fusion* production mode (VBF), two vector bosons are radiated by the initial quarks and fuse to a Higgs boson. The jets, produced by the initial quarks in the detector, can be used to suppress backgrounds (figure 2.4 (b)). This production mode is of special interest, because coupling of the Higgs boson to two vector bosons (VVH) can be measured directly. The third highest cross section constitutes the *associated*

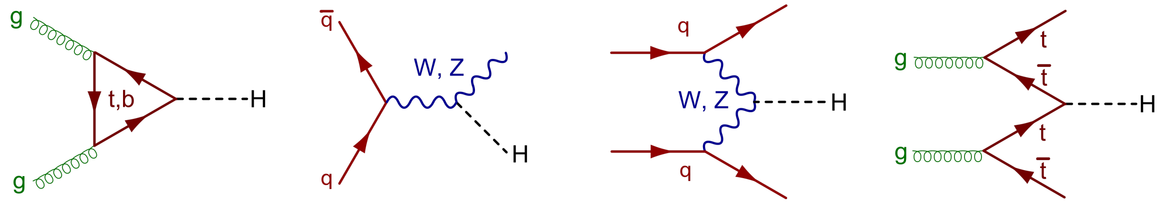

(a) (b) (c) (d)

Figure 2.4: The four most important Higgs production modes at the LHC: *gluon-gluon fusion* (a), *vector boson fusion* (b), *associated production* (c) and *top quark fusion* (d). [11]

production with a vector boson (VH) of the Higgs boson. The two initial quarks fuse to a vector boson (W or Z boson) which radiates a Higgs boson (Fig. 2.4 (c)). The production via a top and antitop quark pair has the smallest cross section of the four. Here, the Higgs is accompanied by two top quarks. Since $t\bar{t}$ processes lead to a high number of jets in the event, this is the most difficult Higgs-boson production mode in terms of signal extraction and background understanding (Fig. 2.4 (d)) [4].

The Higgs boson is not stable, therefore it can only be detected through its decay products. Since its coupling is proportional to a particles mass, the *branching ratios* (BRs) of the Higgs boson depend strongly on its mass. The BRs of different Higgs-boson decay modes as a function of the Higgs-boson mass m_H are shown in Fig. 2.5.

For Higgs-boson masses below 135 GeV the process $H \rightarrow b\bar{b}$ has the highest BR, since the b quark is the heaviest elementary particle kinematically available for a Higgs boson with mass $m_H < 135$ GeV. The process $H \rightarrow WW$, where one W is produced off-shell, has the highest BR for a Higgs-boson mass above 135 GeV. The cleanest signatures in the detector, however, are created by the processes $H \rightarrow \gamma\gamma$ and $H \rightarrow ZZ^* \rightarrow llll$. These so called "golden channels" allow for a complete reconstruction of the Higgs-boson mass, since no energy can leave undetected in form of neutrinos. The process $H \rightarrow ZZ^* \rightarrow lll$ also has an excellent

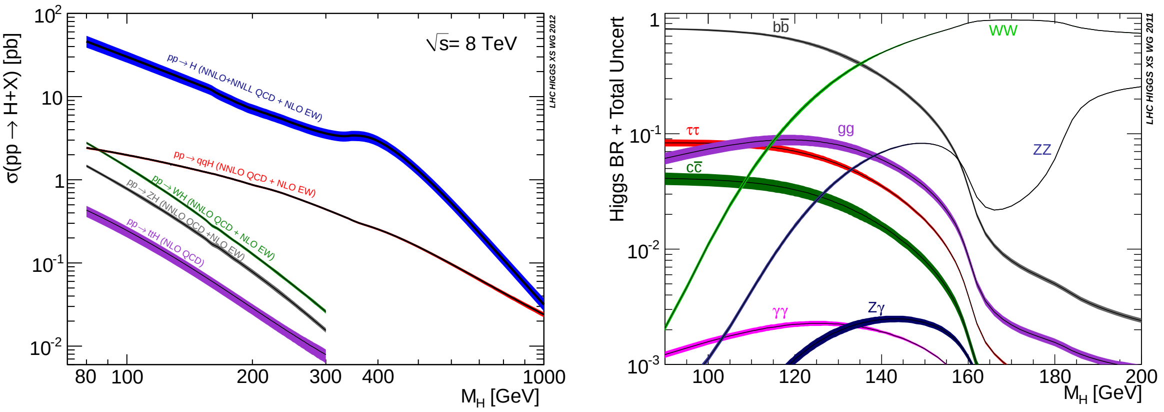

Figure 2.5: Left: cross sections of the four most important Higgs-boson production modes at the LHC for a center of mass energy $\sqrt{s} = 8\,TeV$ as a function of the Higgs-boson mass m_H: *gluon fusion* ($pp \rightarrow H$), *vector boson fusion* ($pp \rightarrow qqH$), *associated production* with a vector boson ($pp \rightarrow WH$ and $pp \rightarrow ZH$) and *top quark fusion* ($pp \rightarrow ttH$). Right: cross section times branching ratio for various Higgs-boson decays. The uncertainties are represented by the width of the lines [12].

signal over background ratio.
The decay of the Higgs boson into two tau leptons ($H \rightarrow \tau\tau$) is discussed in greater detail in the following, since this is the channel investigated in this thesis.

2.2.3 Higgs-boson decay into two τ leptons

The Higgs-boson decay into two τ leptons ($H \rightarrow \tau\tau$) has a branching ratio (BR) of $6.32 \cdot 10^{-02}$ with an relative error of 5.7% for a Higgs-boson mass of $m_H = 125\,\text{GeV}$ [13]. In this range, a Higgs boson like particle has been discovered in Summer 2012 (see Section 2.3).
The tau lepton is the heaviest lepton with a mass of $1776.82 \pm 0.16\,\text{MeV/c}^2$ which is higher than the mass of the lightest hadrons [4]. It is therefore the only lepton that can decay hadronically. However, this decay mode does not have the cleanest signature in a hadron-collider environment. In addition, the tau can decay into a tau neutrino and an electron or muon accompanied by its corresponding neutrino (leptonic decay), or into light quarks (hadronic decay). Therefore, the final state includes at least one neutrino depending on the tau decay, which makes a full Higgs-boson mass reconstruction difficult.
No other leptonic decay channel of the Higgs-boson has a noteworthy significance. The $H \rightarrow \tau\tau$ decay channel is therefore of special interest, since it is the only decay channel in which the Yukawa coupling to leptons can be measured directly. The $qq \overset{VBF}{\rightarrow} H \rightarrow \tau\tau$ cross section times branching ratio ($\sigma \times BR$) is the most prominent of all subchannel production modes in the low Higgs-boson mass range as can be seen in Fig. 2.6. Which makes $qq \overset{VBF}{\rightarrow} H \rightarrow \tau\tau$ the dedicated channel to directly probe the $H \rightarrow \tau\tau$ coupling.

2.3 Current knowledge of the Higgs boson

As mentioned in Section 2.1.3 the mass of the Higgs boson is a free parameter in the Standard Model. Although loose constraints have been put on the Higgs-boson mass by theoretical arguments, its determination relies on experimental measurements [1].
Before the LHC started data taking, experiments located at the *Large Electron Positron Collider* (LEP) and the *Tevatron* excluded Higgs-boson masses below 114.4 GeV (LEP) and between 158 and 175 GeV (Tevatron). Through electroweak precision measurements performed at LEP, it was possible to restrain the Higgs mass indirectly due to loop corrections involving the Higgs boson. The results of these indirect searches are represented by the $\Delta\chi^2$ plot, shown in Fig. 2.7. Low Higgs-boson masses are preferred by these results [14].
Since the cross section of the Higgs-boson production is small, as can be seen in Fig. 2.3, large amounts of data are required to put further constraints on the Higgs-boson mass. The LHC collected approximately $11\,\text{fb}^{-1}$ of data during 2011 and the first half of 2012, which led to the discovery of a new particle in the region of 126 GeV and the exclusion of the Higgs boson in a large mass range above this value. Figure 2.8 shows the combined results of the search channels $H \rightarrow ZZ^* \rightarrow llll$, $H \rightarrow WW^*$, $H \rightarrow \gamma\gamma$, $H \rightarrow b\bar{b}$ and $H \rightarrow \tau\tau$ for the ATLAS (left column) and CMS collaborations (right column), respectively. In the region around 126 GeV the ATLAS and CMS collaborations see a significant excess of events corresponding to a local p_0-value of the order of 10^{-9} (ATLAS) or 10^{-7} (CMS) (cf. top row of Fig. 2.8). The found p_0-values correspond to significances of six and five standard deviations,

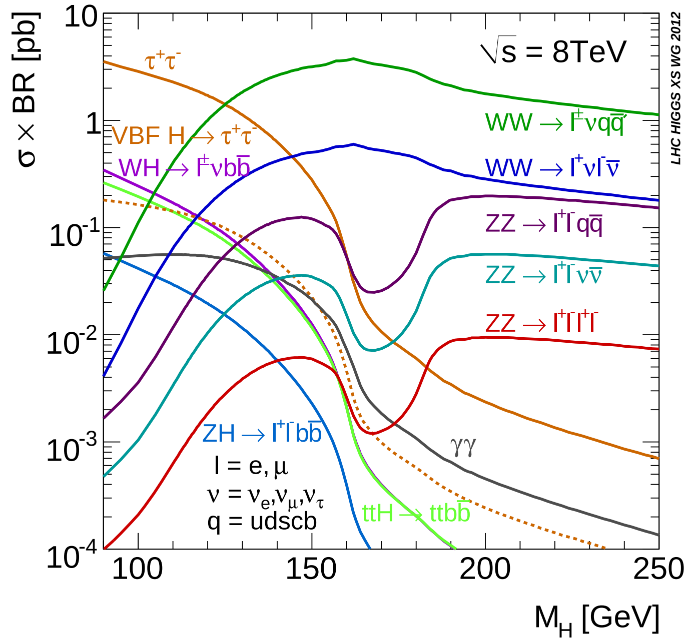

Figure 2.6: Display of the cross section times branching ratio ($\sigma \times BR$) of different Higgs decay modes for different Higgs masses m_H at a center of mass energy of $\sqrt{s} = 8\,TeV$. For the $H \rightarrow \tau\tau$ decay channel the total $\sigma \times BR$ (solid line) as well as the $\sigma \times BR$ for the VBF Higgs production mode only (dashed line) are shown. [12]

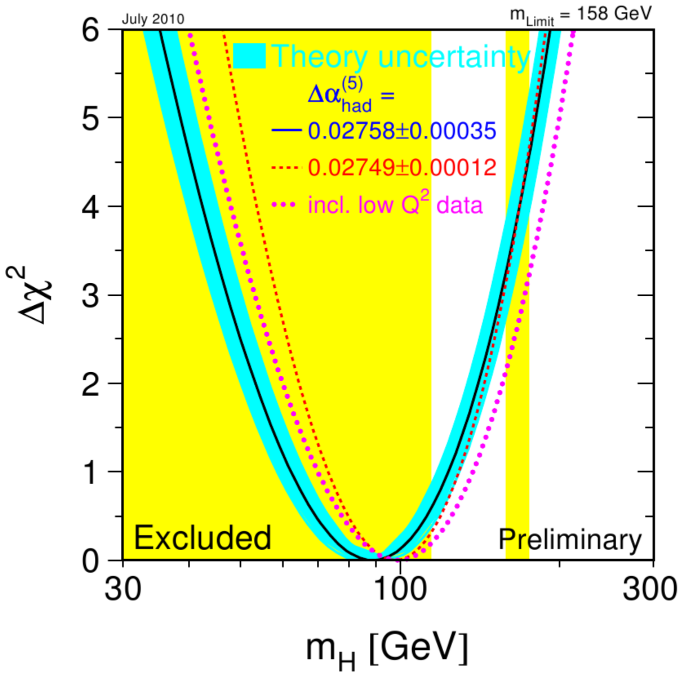

Figure 2.7: Constraints put on the Higgs-boson mass by LEP and Tevatron. The solid line represents the $\Delta\chi^2 = \chi^2 - \chi^2_{min}$ fit as a function of the Higgs-boson mass m_H, combining LEP and Tevatron results. The regions below 114 GeV (LEP) and between 158 and 175 GeV (Tevatron) have been excluded at 95% CL$_s$ [14].

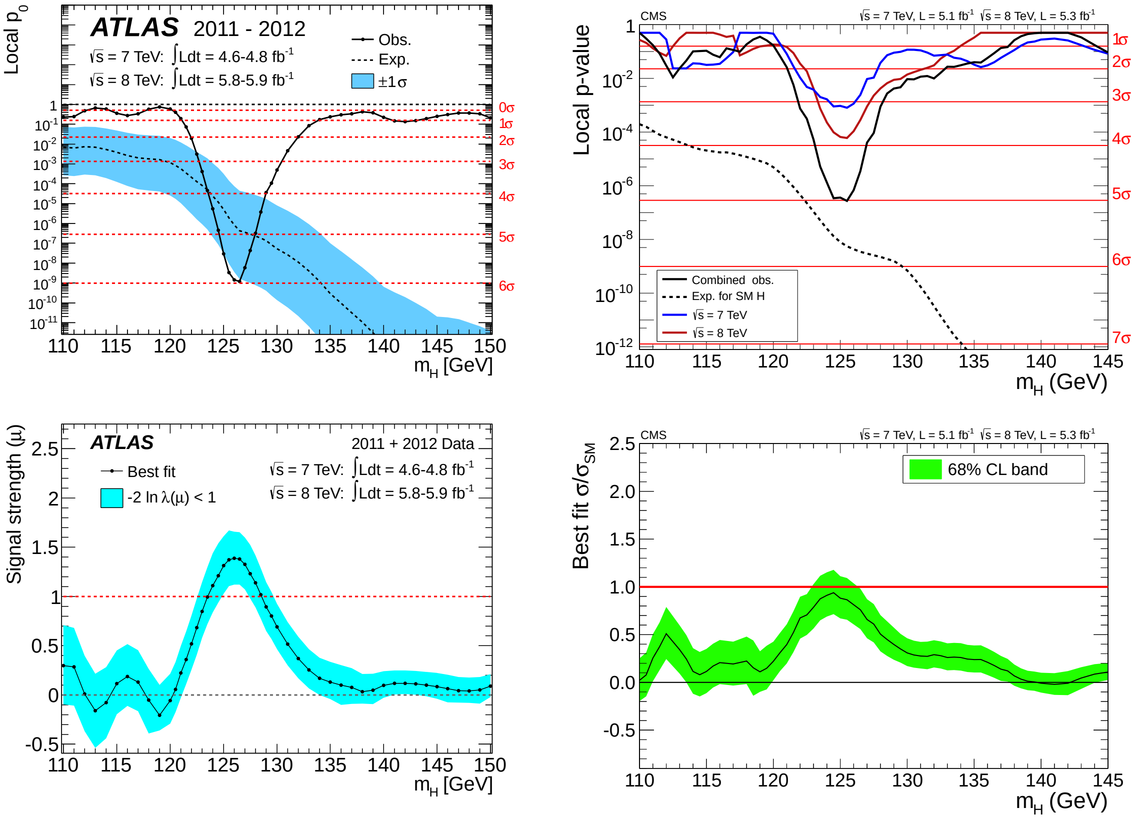

Figure 2.8: Top row: Observed local p_0 value (solid black line) and expected p_0 value (dashed line) under the SM Higgs-boson hypothesis as a function of the Higgs-boson mass m_H for the ATLAS (top left) and CMS experiments (top right). The horizontal red lines denote to the p-values which correspond to a 1-6σ significance. Bottom row: Observed best-fit signal strength $\hat{\mu} = \sigma/\sigma_{SM}$ as a function of the Higgs-boson mass for the combination of the 2011 and 2012 data sets. The blue (green) band corresponds to the $\pm 1\sigma$ uncertainty of the signal strength $\hat{\mu}$ as derived by the ATLAS (CMS) collaboration [7] [8].

respectively. The local p_0 value denotes the probability, that assuming there is no signal, an observed excess is caused by a statistical fluctuation of the background. A complete definition of the local p_0 value is given in Ref. [15]. In the bottom row of Fig. 2.8 the best fit for the signal strength $\mu = \sigma/\sigma_{\mathrm{SM}}$ in units of the SM Higgs-boson signal strength under the background-plus-signal hypothesis is shown. As can be seen in Fig. 2.8 bottom right plot, the CMS collaboration observes a signal strength that is compatible with the signal strength of the SM Higgs boson, which is indicated by the red line. The ATLAS collaboration observes a slightly higher signal strength of $\mu = 1.4 \pm 0.3$. No clear excess could be observed in the $H \rightarrow b\bar{b}$ and $H \rightarrow \tau\tau$ channels [15].

The mass of the newly discovered particle could be constrained to a narrow mass range by the ATLAS as well as the CMS collaboration:

$$m_H^{\mathrm{ATLAS}} = 126.0 \pm 0.4\ (\mathrm{stat.})\ \pm 0.4\ (\mathrm{sys.}), \tag{2.44}$$

$$m_H^{\mathrm{CMS}} = 125.3 \pm 0.4\ (\mathrm{stat.})\ \pm 0.5\ (\mathrm{sys.}). \tag{2.45}$$

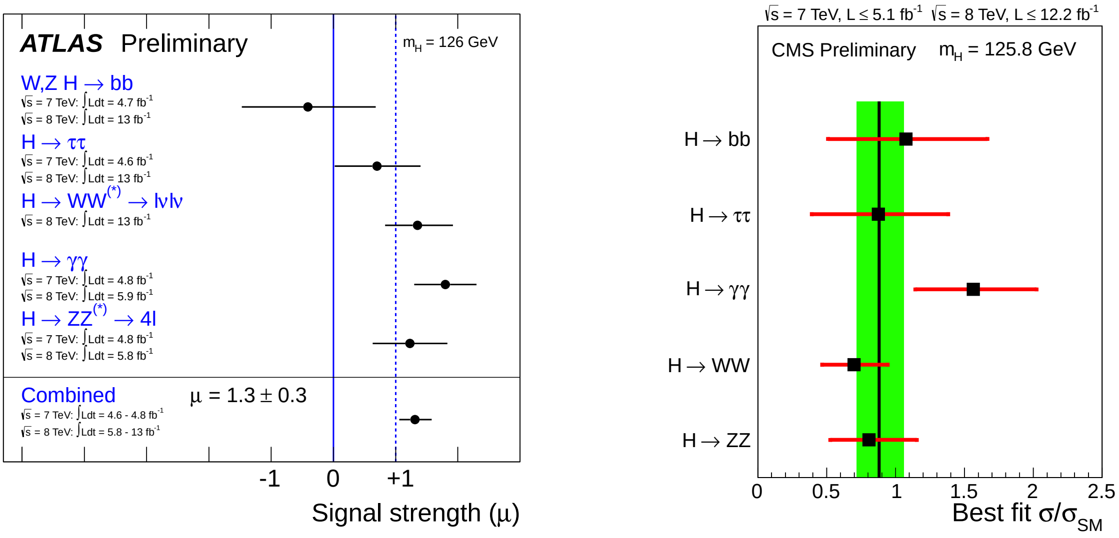

Figure 2.9: Signal strength $\mu = {}^{\sigma}/_{\sigma_{SM}}$ for different Higgs-boson decay modes for the ATLAS (left) and CMS experiments (right). Right: CMS collaboration results of the combination and its uncertainty are represented by the vertical solid black line and green band [17] [16].

Although a significant excess could not be observed in all investigated decay channels, the discovered particle is compatible with the Standard Model Higgs boson. The fact that an excess is observed in the $H \longrightarrow \gamma\gamma$ channel, excludes a boson with spin 1 [7] [8].
An update on the July 2012 results has been made public in November 2012 by the ATLAS and CMS collaborations. The updated results include a larger data set of approximately 13 fb^{-1} for 2012. The ATLAS collaboration has updated the results in the $H \longrightarrow WW^* \longrightarrow l\nu l\nu$, $H \longrightarrow \tau^+\tau^-$ and $H \longrightarrow b\bar{b}$ to the 2012 13 fb^{-1} data set. Results regarding the signal strength $\mu = {}^{\sigma}/_{\sigma_{SM}}$ are shown for the CMS and ATLAS collaborations in Fig. 2.9 left and right, respectively. A signal strength of $\mu = 1$ corresponds to the Standard Model Higgs boson. The combined results of the investigated decay channels are compatible with a Standard Model Higgs boson, although the $H \longrightarrow \gamma\gamma$ decay channel prefers higher values of μ in both experiments [16] [17].

3 The ATLAS detector

The ATLAS Detector (**A** **T**oroidal **L**HC **A**pparatu**S**) is a multi-purpose detector located at the **L**arge **H**adron **C**ollider (LHC) near Geneva in Switzerland.
With a circumference of 27 km the LHC is the largest proton-proton collider ever built. The accelerator lies in a tunnel approximately 100 m below the surface and accelerates protons in two beams running in opposite directions. The proton beams are bent by superconducting dipole magnets which generate magnetic fields with strengths up to 8.3 T and are cooled down to 1.9 K with liquid helium.
The LHC was designed for a center-of-mass energy of $\sqrt{s} = 14$ TeV. In the last two years of data taking the LHC has run with a center-of-mass energy of $\sqrt{s} = 7$ TeV in 2011 and $\sqrt{s} = 8$ TeV in 2012, respectively.
Four experiments are located at the four beam crossings, which are based at linear sections of the collider: ATLAS, ALICE (**A** **L**arge **I**on **C**ollider **E**xperiment), CMS (**C**ompact **M**uon **S**olenoid) and LHCb (**L**arge **H**adron **C**ollider **b**eauty).
As reference for particle reconstruction, a common coordinate system which considers the cylindrical symmetry of the ATLAS detector is used. In this coordinate system the x axis points towards the center of the LHC-ring, the y axis points upwards and the z axis runs

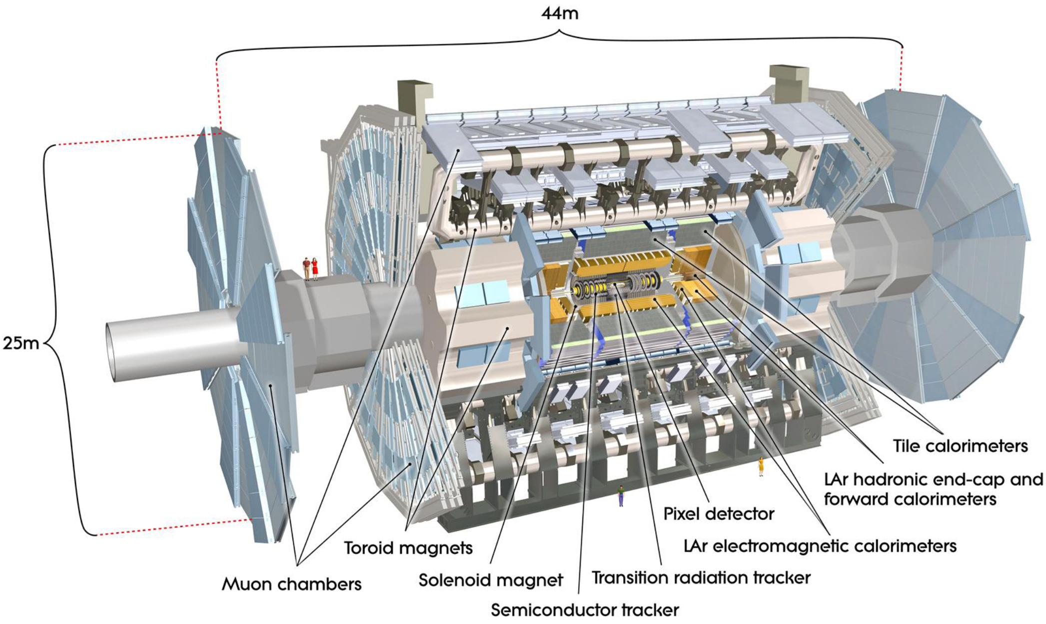

Figure 3.1: A graphic display of the ATLAS detector showing all detector components. Each component is described briefly in the following section [18].

along the beam axis. The azimuthal angle ϕ is measured in the x-y-plane, the polar angle θ measures the inclination to the z axis and R measures the distance from the beam pipe. A common quantity used to describe the angle of a particle relative to the beam axis is the *pseudorapidity* $\eta = -ln\left(\tan\frac{\theta}{2}\right)$.

3.1 Detector components

The ATLAS Experiment is explained in great detail in Ref. [18] and all information about the detector components has been taken from there. Here, only a short description is given.
As mentioned before, the ATLAS Detector is a multi-purpose detector, designed for the discovery of new particles such as the Higgs boson and searches of physics beyond the Standard Model. Due to the high material density of the detector paired with its cylindrical 4π design, an almost complete reconstruction of hard scattering processes is possible. In order to manage the high interaction rates the experiment comes with a multistage trigger system. For more details see Ref. [18].
The ATLAS Detector consists of various subdetectors, each specialized in a different detection task.

3.1.1 Inner Detector

Localized at the inner most section of the ATLAS detector is the *inner detector* consisting of three subdetectors which are briefly described below. It is of cylindrical shape and ranges from $R = 50.5\,\text{mm}$ to $R = 1082\,\text{mm}$. The inner detector has the highest resolution of all detector parts and is crucial for the reconstruction of primary and secondary vertices. It also provides a momentum measurement of charged particles.

Pixel detector Small silicon sensors (*pixels*) are arranged in three layers in a cylindrical fashion around the beam pipe and in disks orthogonal to the beam pipe at the end-caps. This geometry results in a resolution of $10\,\mu$m in the R-ϕ-plane for barrel and end-cap region and $115\,\mu$m in z (R) direction for the barrel region (end-caps).

Semiconductor Tracker (SCT) The SCT is also shaped in a cylindrical geometry and surrounds the pixel detector. Its silicon strip sensors are arranged in four layers around the barrel and nine layers in the end-caps. The strip sensors are slightly twisted around each other to allow a 3D reconstruction of particle tracks. The SCT reaches a resolution of $17\,\mu$m in the R-ϕ plane for barrel and end-cap region and $580\,\mu$m in z (R) direction in the barrel region (end-caps).

Transition Radiation Tracker (TRT) Located at the outermost section of the inner detector is the TRT. It consists of polyimide drift tubes with a diameter of 4 mm. The drift tubes are arranged parallel to the beam axis in the barrel region and radial in the end-caps. Therefore only a resolution of $130\,\mu$m in the R-ϕ plane can be provided. The xenon-based gas mixture in the drift tubes allows an energy measurement which is independent of the calorimeter measurements. Especially electrons, which emit the greatest amount of transition radiation, are identified more easily with the additional information from the TRT.

The inner detector is surrounded by the central solenoid magnet which provides a 2 T axial field. This magnetic field enables a momentum measurement based on the curvature of a charged particles trajectory. To avoid large energy losses before the particles reach the calorimeter system, the central solenoid has been built with minimal material thickness.

3.1.2 Calorimeter system

The calorimeter system is designed for energy measurements. Both, the *electromagnetic* and the *hadronic calorimeter* are sampling calorimeters, meaning they consist of alternating layers of absorber and detector material. Crucial for the energy measurement is the amount of absorber in the calorimeters. It has to be thick enough to enable a full particle energy deposition and avoid leakage into the *muon spectrometer* (see 3.1.3).

Electromagnetic calorimeter (EMcal) The EMcal consists of alternating layers of liquid Argon (LAr) as detector and lead as absorber material. The unusual accordion geometry allows a full ϕ coverage. The barrel section of the EMcal covers a range up to $|\eta| < 1.475$ where the end-cap region is divided into two sections. The central region covers the range of $1.375 < |\eta| < 2.5$ with a higher granularity than the forward region, which covers the range $2.5 < |\eta| < 3.2$. With a thickness of approximately 20 radiation lengths the design energy resolution of the EMcal is $\frac{\sigma_E}{E} = 10\%/\sqrt{E} \oplus 7\%$[1]. The EMcal absorbs the total energy of electrons (e) and photons (γ).

Hadronic calorimeter (Hcal) The Hcal is divided into two parts. A tile calorimeter in the central region ($|\eta| < 1.7$) which uses scintillator tiles as detector and steel as absorber material (three layers), and the hadronic end-caps (HEC, $1.5 < |\eta| < 3.2$) which uses LAr (detector) and copper (absorber) in four layers. The Hcal has a thickness of approximately ten radiation lengths and a design resolution of $\frac{\sigma_E}{E} = 50\%/\sqrt{E} \oplus 3\%$.

Forward Calorimeter (FCal) The purpose of the FCal is to detect particles in the very forward region of $3.1 < |\eta| < 4.9$. It uses LAr as detector material and has only three layers of absorber material. The first is copper for EM measurements and the following two layers are tungsten for hadronic measurements. The FCal has a thickness of approximately ten radiation lengths and a design resolution of $\frac{\sigma_E}{E} = 100\%/\sqrt{E} \oplus 10\%$.

3.1.3 Muon detector

Muons are minimum ionizing particles, which in contrast to electrons, deposit only small amounts of energy in the calorimeter system. Therefore, a specialized *Muon Spectrometer* (MS) surrounds all other parts of the ATLAS detector to assure reliable momentum measurements (cf. Fig. 3.1).

The momentum measurement is based on the magnetic fields provided by large toroidal magnets. Due to the geometry of the magnets, the trajectories of charged particles are bent in the R-z plane rather than the R-ϕ plane, which corresponds to the bending plane of the inner solenoid. Separate toroidal magnet systems are used for the barrel ($|\eta| < 1.4$) and end-cap region ($1.6|\eta| < 2.7$), which produce magnetic fields with strengths ranging from 0.2-2.5 T

---

[1] The notation $a \oplus b = \sqrt{a^2 + b^2}$ has been used, E in GeV.

in the barrel region and 0.2-3.5 T in the end-caps, respectively.
Monitored Drift Tubes (MDT) are used for the detection of tracks in the region $|\eta| < 2.7$. In the region of $2.0 < |\eta| < 2.7$ Cathode Strip Chambers (CDC) are used in addition. The CDCs are multiwire proportional chambers and able to manage higher signal rates as well as provide better spacial resolution. Due to the higher magnetic field strength and the greater dimensions of the MS compared to the central solenoid, the MS has a higher bending power for charged particles. Due to the larger dimensions of the MS a more precise measurement of the muon momentum for high-p_T muons is achieved, than with the inner detector alone. The design resolution of the muon spectrometer is $\frac{\sigma_{p_T}}{p_T} = 10\%$ for $p_T(\mu) = 1$ TeV. The built-in muon trigger system consists of resistive plate chambers in the barrel and thin gap chambers in the end-cap region, respectively.

3.1.4 Trigger System

To manage the high bunch crossing rate of approximately 40 MHz at nominal bunch spacing, the ATLAS experiment is equipped with a sophisticated multi-stage trigger system. The Level-1 trigger (L1) uses a subset of the detector information and reduces the rate to approximately 75 kHz. More detector information is accessed by the Level-2 trigger (L2) and full detector information is used by the event filter (EF). In the end a final data-taking rate of approximately 200 Hz is achieved.

4 Particle reconstruction and identification

This chapter focusses on the reconstruction and identification of physical objects in the ATLAS detector. Also a detailed overview of a newly developed algorithm is given, which evaluates the number of neutral pions in a τ_h decay. In addition, this algorithm offers an alternative momentum reconstruction for the hadronic τ candidate. Information from this algorithm is not included in the usual $H \rightarrow \tau_l \tau_h$ analysis. The impact of this information on the sensitivity of the analysis is discussed in chapter 6 of this thesis.

4.1 Particle reconstruction and identification

The reconstruction and identification of particles with the ATLAS detector is a complex procedure which has been described in great detail in Ref. [19]. Here, only a short overview with emphasis on the tau lepton is given.

4.1.1 Track reconstruction

The reconstruction of the tracks that charged particles leave in the inner detector is split into three stages:

Preprocessing stage At the *preprocessing stage* the raw data of the pixel detector and SCT is converted into clusters, which are transformed into space points. The raw timing of the TRT is translated into calibrated drift circles.

Track finding stage Two track finding strategies are used, each optimised for a different purpose.
The default strategy exploits the high granularity of the pixel detector and the SCT to find tracks with origins near the interaction region. Seed tracks are formed from three pixel layers and the first SCT layer, which are then extended through the SCT. These track candidates are fitted and cleaned from outlying clusters. Clusters shared by more than on track are specifically treated and fake tracks removed by applying quality cuts. The surviving tracks are then extrapolated to the TRT and combined with the drift tube information. A final fit is performed using the information of all three detectors.
By the default strategy unused track fragments in the TRT are searched by the back-tracking strategy. Those are then extrapolated inwards to improve the tracking of long-lived particles.

Post-processing stage All the information provided by the previous two stages is used, to reconstruct the primary vertices with a dedicated vertex-finder algorithm. Afterwards other algorithms are used to reconstruct secondary vertices and photon conversions.

4.1.2 Electron reconstruction and identification

Electrons are charged particles which leave tracks in the inner detector and deposit most of their energy in the EM calorimeter. Two algorithms are used to reconstruct electrons and distinguish them from jets and a third algorithm is specialized on electrons with $|\eta| > 2.5$, but does not use any track information.

The standard clustering algorithm which is applied to central electrons used in this thesis, is the *sliding window* algorithm. It starts with energy clusters in the EM calorimeter, which are then associated to tracks from the inner detector.

The sliding window algorithm chooses a window of 3×5 cells in the middle layer of the EM calorimeter which corresponds to 0.025×0.025 in the $\eta - \phi$ plane. If the sum of the *transverse energy* in these cells succeeds $2.5\,\text{GeV}$ they are considered a cluster. The cluster reconstruction efficiency is close to 100% for electrons with a transverse energy $E_T > 15\,\text{GeV}$. Tracks from the inner detector are then associated to the clusters of the EM calorimeter. To allow for energy losses due to bremsstrahlung which reduces the bending radius of the particle trajectory, different track-cluster matching criteria are applied in the bending direction of the solenoid magnet or in the other direction. Clusters and tracks are matched if $\Delta\eta < 0.1$ and $\Delta\phi < 0.1$ in the bending direction or $\Delta\phi < 0.05$ in the opposite direction, respectively. Tracks with hits in the silicon detectors are preferred over others if multiple tracks are matched to one cluster, and the closest is chosen.

For a found electron candidate, the cluster is newly formed with 3×7 cells in the barrel region and 5×5 cells in the end-caps, using the middle layer of the EM calorimeter. The electron momentum four vector is given through the η and ϕ of the track at the primary vertex. The energy information is taken from the cluster.

To distinguish electrons from other physical objects, identification (ID) criteria are applied after reconstruction. Depending on the firmness of the applied cuts, ID criteria are divided into three categories: *loose*++, *medium*++ and *tight*++. The three categories are gradually based on each other.

Information from the inner detector and the EM calorimeter is used by all ID categories. The highest efficiency but also the highest jet contamination has the *loose*++ category. It uses track information from the silicon detectors as well as information about the shower shape in the EM calorimeter and the energy deposition in the hadronic calorimeter.

These requirements are tightened for the *medium*++ category, which also uses information from the TRT as well as from the innermost layer of the pixel detector.

Even tighter cuts are applied by the *tight*++ category, especially on the matching criteria of tracks and clusters. Naturally this category has the lowest efficiency but also the lowest contamination by other physical objects.

Tight++ electrons are used in the final selection of this analysis (cf. Chapter 5).

4.1.3 Muon reconstruction

Four muon reconstruction algorithms are in use.
Standalone muons are reconstructed using only information from the MS and the calorimeter system. Therefore, low energy muons which do not reach the MS cannot be reconstructed. Also, muons originating from secondary vertices, e.g. from Pion or Kaon decays, cannot be distinguished from muons originating from primary vertices. However, this method covers the largest η region.
In the *segment tagged* muon algorithm, tracks from the inner detector are extrapolated to the MS and selected as muon candidates if matched to track segments in the MS. This algorithm is particularly fit to reconstruct low p_T muons, since only information from the inner detector is used for the momentum measurement.
The full information from the inner detector and the MS is used by the *combined* muon algorithm. Tracks from the independent measurements of the two detector systems are extrapolated to the beam axis and matched to pairs. The pair with the lowest *matching parameter* χ^2_{match} is chosen. The matching parameter is calculated using the vectors $\mathbf{T}_{ID}$ and $\mathbf{T}_{MS}$ which hold the track information of inner detector tracks and MS tracks respectively, as well as the corresponding covariance matrices $\mathbf{C}_{ID}$ and $\mathbf{C}_{MS}$:

$$\chi^2_{match} = \left(\mathbf{T}_{MS} - \mathbf{T}_{ID}\right)^{\intercal} \left(\mathbf{C}_{MS} + \mathbf{C}_{ID}\right)^{-1} \left(\mathbf{T}_{MS} - \mathbf{T}_{ID}\right). \tag{4.1}$$

The *calorimeter tagged* muon algorithm combines tracks from the inner detector with energy depositions in the calorimeter system.
In this thesis STACO[1] combined muons are used.

4.1.4 Lepton isolation

Electrons and muons coming from Z or W decays have less energy depositions in their immediate surroundings than leptons contained in jets. This feature can be used to select well isolated leptons. The quantities based on the isolation in the calorimeter and inner detector, respectively, in a cone with radius R_0 around the lepton are defined as

$$E_T^{cone}(R_0) = \left(\sum_{R<R_0}^{cells} E_T^{cell}\right) - E_T^{lep}, \qquad p_T^{cone}(R_0) = \left(\sum_{R<R_0}^{tracks} p_T^{track}\right) - p_T^{lep}. \tag{4.2}$$

The energy deposition around the lepton in the calorimeter E_T^{cone} can also be applied to neutral particles. Whereas the track momenta p_T^{cone} around the lepton can be used to distinguish particles originating from the primary vertex of the hard interaction from particles coming from other vertices, e.g. pile-up.
Both variables are used for electrons and muons in this thesis.

---

[1] STACO and MuID are frameworks which differ slightly in the implementation of the listed algorithms.

4.1.5 Jet reconstruction

Quarks and gluons cannot exist as free particles and undergo hadronization, forming showers of collimated hadrons called *jets*. To reconstruct jets two classes of algorithms are in use: *cone*-based and *cluster*-based algorithms.
Cone algorithms try to maximize the Energy or transverse momentum in a cone in the $\eta - \phi$-space.
Jets used in this thesis have been reconstructed via the *anti-k_T* algorithm, which is a cluster algorithm. The anti-k_T algorithm uses a measure of distance d_{ij} in the calorimeter to group objects together and a stopping criterion d_{iB} which aborts the grouping after a certain benchmark is reached. The distance d_{ij} between two objects i and j in the calorimeter is calculated using the transverse momenta $k_{Ti,j}$ of the objects, the geometrical distance $\Delta R_{ij} = \sqrt{(\Delta y_{ij})^2 + (\Delta\phi_{ij})^2}$ between the objects, with y being the rapidity, and the distance parameter $R = \sqrt{\Delta\eta^2 + \Delta\phi^2}$:

$$d_{ij} = \min\left\{\frac{1}{k_{Ti}^2}, \frac{1}{k_{Tj}^2}\right\} \times \frac{\left(\Delta R_{ij}\right)^2}{R^2}. \tag{4.3}$$

The stopping criterion d_{iB} is defined as the minimal distance of object i to the beam axis:

$$d_{iB} = \frac{1}{k_{Ti}^2}. \tag{4.4}$$

The two factors d_{ij} and d_{iB} are calculated for all objects in an event. As long as d_{ij} is the minimal distance of two objects i and j, they are grouped together and considered a single object. However, if the distance d_{iB} of the object i to the beam axis is smaller than the distance to another object j (i.e. $d_{iB} < d_{ij}$), object i is considered a jet and removed from the list of possible jet candidates. This method is repeated until all jets have been defined.
The jets used in this thesis have been reconstructed with the anti-k_T algorithm using a distance parameter $R = 0.4$ [20].

4.1.6 Reconstruction of hadronic τ leptons

Tau leptons have a lifetime corresponding to approximately $c\tau \approx 87\mu m$ and therefore decay before reaching the inner detector. As mentioned in Section 2.2.3 the tau lepton can decay hadronically with a BR of 64.7%. The light quarks emerging from the tau decay undergo hadronization due to the strong interaction. Due to charge conservation an odd number of charged pions are formed, dominated by one or three charged pions often referred to as 1-prong or 3-prong decay respectively. The BRs for the tau decay are displayed in Table 4.1. Decays with five or more charged pions are very rare, and are not taken into account in the following. It is a great challenge to distinguish hadronic tau decays (τ_h) from QCD jets which have a cross section that is higher by many orders of magnitude. The characteristic features of a τ_h like the 1 or 3-prong signature or the narrow collimation of jet constituents is used to identify τ_h jets among the multijet background. The collimation of a jet can be represented with the *electromagnetic radius R_{EM}*. The electromagnetic radius is the shower

Decay	BR
$\tau \rightarrow e\nu_e\nu_\tau$	17.83 ± 0.04 %
$\tau \rightarrow \mu\nu_\mu\nu_\tau$	17.41 ± 0.04 %
$\tau \rightarrow \pi^\pm\nu_\tau$	10.83 ± 0.06 %
$\tau \rightarrow \pi^\pm\pi^0\nu_\tau$	25.52 ± 0.09 %
$\tau \rightarrow \pi^\pm\pi^0\pi^0\nu_\tau$	9.30 ± 0.11 %
$\tau \rightarrow \pi^\pm\pi^0\pi^0\pi^0\nu_\tau$	1.05 ± 0.07 %
$\tau \rightarrow \pi^\pm\pi^\pm\pi^\mp\nu_\tau$	9.31 ± 0.06 %
$\tau \rightarrow \pi^\pm\pi^\pm\pi^\mp\pi^0\nu_\tau$	4.62 ± 0.06 %
$\tau \rightarrow K^*(892)\nu_\tau$	1.20 ± 0.07 %
$\tau \rightarrow \pi^\pm\bar{K}^0\nu_\tau$	0.84 ± 0.04 %
$\tau \rightarrow K^\pm\nu_\tau$	0.70 ± 0.01 %

Table 4.1: Branching ratios of the leptonic and hadronic tau decays [4].

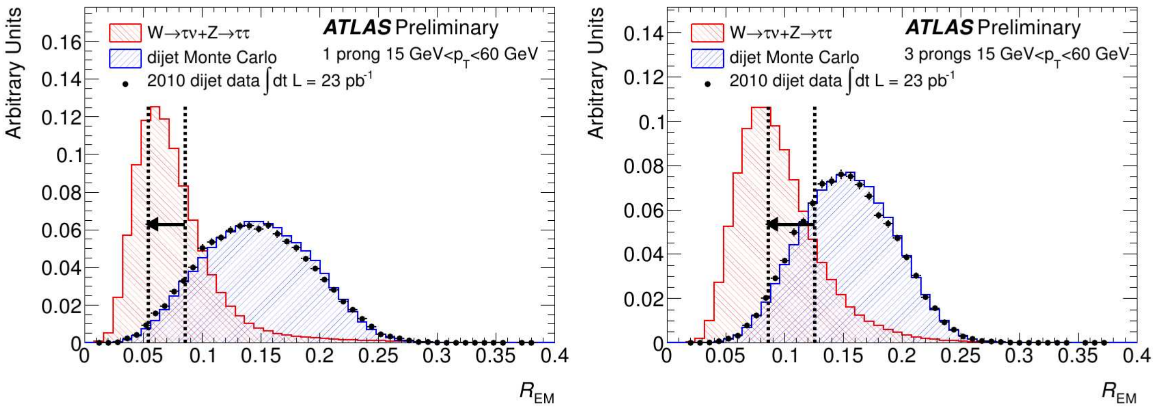

Figure 4.1: Displayed are the distributions of τ_h jets selected from $W \rightarrow \tau\nu$ and $Z \rightarrow \tau\tau$ processes (red) and of QCD jets drom dijet Monte Carlo samples (blue) for 1-prong (left) and 3-prong τ_h (right). The dashed lines indicate the cut values of the cut-based identification [21].

width in the EM calorimeter weighted by the transverse energy of the object:

$$R_{EM} = \frac{\sum_{i=1}^{n} E_{T,i}\sqrt{(\eta_i - \eta_{\text{cluster}})^2 + (\phi_i - \phi_{\text{cluster}})^2}}{\sum_{i=1}^{n} E_{T,i}}. \tag{4.5}$$

The parameters $E_{T,i}$, η_i and ϕ_i refer to the angular and kinematic variables of cell i in the EMcal in a cluster with $\Delta R < 0.4$. Since τ_h jets consist of few, light particles which have a small opening angle, the R_{EM} of τ_h jets is smaller than for QCD jets of the same p_T which usually include many constituents with larger opening angle (cf. Fig. 4.1).

Hadronic τ candidates are based on calorimeter jets in the range of $|\eta| < 2.5$ which have been reconstructed using the anti-k_T algorithm with $R < 0.4$ (cf. Section 4.1.5). Those jets are referred to as seed jets.

To reconstruct the τ_h four-momentum, η and ϕ are taken from the seed jet, which have been determined by the four-vector sum of the jet constituents by assuming zero mass for

each of them. The energy of the τ_h candidate is calculated via the sum over all cells within $\Delta R = \sqrt{(\Delta\eta)^2 + (\Delta\phi)^2} < 0.4$ of the seed axis. The mass of the τ_h is considered to be exactly zero, hence the transverse energy is equal to the transverse momentum.
Since τ_h jets are more collimated than QCD jets, the area around a τ_h candidate is divided into two regions. The *core cone* ($\Delta R < 0.1$), which is used for track association to the τ_h candidate and the *isolation annulus* ($0.1 < \Delta R < 0.2$)[2]. Tracks within the core cone are associated to the τ_h candidate, if they pass several quality criteria including the number of hits in the pixel and SCT detectors as well as the distance of the track to the primary vertex. The charge of the τ_h candidate is calculated by summing the charge of all associated tracks. Depending on the number of tracks in the cone core, the τ_h candidates are classified as single or multiprong.

The reconstructed τ_h candidates provide modest discrimination power against QCD jets, which is why the τ_h reconstruction is followed by the τ_h identification (ID). Three different discriminants are used to distinguish τ_h jets from QCD jets. The *cut-based* selection, *projective likelihood* identification and identification using *boosted decision trees* use different combinations of the identification variables listed in Ref. [21]. Common to all discriminants is the rejection of candidates with zero reconstructed tracks.
The τ_h candidates used in this thesis have been identified with the boosted decision tree (BDT) method. The BDTs are trained on the Monte Carlo samples $W \to \tau\nu$ and $Z \to \tau\tau$ for the signal and dijet events selected from 2011 data for background. The signal efficiency and background efficiency are defined as

$$\varepsilon_{sig}^{1/3\text{-prong}} = \frac{\left(\begin{array}{c}\text{\# of tau candidates with 1/3 reconstructed track(s), passing}\\ \text{ID, and truth-matched to a simulated 1/3-prong decay}\end{array}\right)}{(\text{\# of simulated visible hadronic taus with 1/3 prong(s)})}, \tag{4.6}$$

$$\varepsilon_{bkg}^{1/3\text{-prong}} = \frac{\left(\begin{array}{c}\text{\# of tau candidates with 1/3 reconstructed track(s)}\\ \text{from dijet events, passing ID}\end{array}\right)}{(\text{\# of tau candidates with 1/3 reconstructed track(s)})}. \tag{4.7}$$

A reconstructed τ_h candidate is considered truth matched, if a simulated τ_h candidate is found within a cone of $\Delta R < 0.2$.
The discriminant BDT is trained to three working points *Loose* ($\varepsilon_{sig} \approx 65\%$), *Medium* ($\varepsilon_{sig} \approx 55\%$) and *Tight* ($\varepsilon_{sig} \approx 35\%$). The BDTs are trained on separate categories corresponding to simulated τ_h events with one or three tracks as well as categories defined by the number of reconstructed primary vertices. The BDT trained on 3-prong events is used for classifying all multiprong events.
The analysis presented in this thesis is based on medium τ_h candidates.

Electrons can mimic the characteristic signature of a 1-prong τ_h.
Properties like the depth and width of the electromagnetic shower can be used to distinguish between electrons and τ_h. A BDT to identify electrons among the τ_h candidates is trained on simulated $Z \to \tau\tau$ and $Z \to ee$ events for the three working points loose, medium and

---

[2] For 2011 the isolation criteria were $\Delta R < 0.2$ (core cone) and $0.2 < \Delta R < 0.4$ (isolation annulus). The isolation critera have changed from 2011 to 2012 to cope with the increased pile-up.

tight. The τ_h in $Z \rightarrow \tau\tau$ events that could be matched to true 1-prong τ_h within $\Delta R < 0.2$ are defined as signal candidates. Electrons from $Z \rightarrow ee$ events matched to true electrons are considered as background candidates.

The electron BDT provides good separation power between electrons and 1-prong τ_h with signal efficiencies of 95%, 85% and 75% for loose, medium and tight, respectively.

Since Muons are minimal ionizing particles, they are not as likely to be misidentified as τ_h. However, large amounts of energy may also occationally be deposited by the muon in the calorimeter or leakage from the electromagnetic calorimeter can lead to muons which are misidentified as 1-prong τ_h. The muon veto algorithm is optimized on $Z \rightarrow \tau\tau$ and $Z \rightarrow \mu\mu$ events using variables like the leading track momentum fraction f_{track}, which is the fraction of track momentum and calorimeter energy, and is usually higher for muons than τ_h.

With a target τ_h efficiency of 96%, a background rejection rate for muons of approximately 55% is reached [22].

4.1.7 Energy calibration

To determine the energy of the reconstructed objects correctly, the detector has to be calibrated. For the EM and hadronic calorimeter this has been done using electron and pion test-beams respectively as well as muons from cosmic rays [23]. Energy losses in the passive parts of the detector are modeled by Monte Carlo simulations and corresponding corrections are applied.

How well known processes in 2010 data are used to further calibrate the energy of different objects is explained shortly in the following.

Electrons

Electrons pass passive detector material before depositing their remaining energy in the EM calorimeter. Therefore, a discrepancy between measured and true electron energy is observed.

The calibration of the electron energy is divided into three steps. First, the raw signal extracted from the EMcal cells is converted into a deposited energy using the electronic calibration of the EMcal. Second, MC based corrections on the calibration are applied to account for energy losses in passive detector materials or energy leakage. Third, another correction on the calibration is applied, based on studies of well known processes such as $Z \rightarrow ee$ and $J/\psi \rightarrow ee$. Studies on these well known processes using the reconstructed di-electron mass have shown that the measured (after MC based calibration correction) and true electron energy have a linear dependence [24]:

$$E_{\text{meas}} = (1+\alpha_i)E_{\text{true}}. \tag{4.8}$$

The correction factor α_i accounts for different η regions which have different amounts of passive detector material. Studies on $Z \rightarrow ee$ events have also shown, that the mass resolution of the Z-peak is slightly worse in data than in Monte Carlo simulation. To correct for this effect, energies in simulated events are convoluted with Gaussians of according width.

A different electron energy calibration method is based on the comparison of the energy deposited in the calorimeter with the independent momentum measurement from the inner detector, E/p. This method has shown, that the fraction of E_{meas} to E_{true} differs less than 2% from unity in the central region of the detector ($|\eta| < 2.47$).

Muons

Since muons undergo much smaller energy losses, their momentum measurement is not affected as much by passive detector material as the electron energy measurement. Studies on $Z \rightarrow \mu\mu$ have shown, that the muon momentum scale is well known [25]. But similar to electrons, the resolution in data is worse than in Monte Carlo simulation. Therefore the simulated muon momenta are smeared accordingly.

Jets

Jets are complex objects which consist of multiple particles that deposit their energies differently in the detector. Particles such as muons or neutrinos, which can appear in a jet due to hadron decays, deposit only little amounts of energy (muons) or no energy at all (neutrinos) in the detector. Neutral pions ($\pi^0 \rightarrow \gamma\gamma$) form electromagnetic showers inside the hadronic shower. When a particle reacts with the detector material energy losses due to nuclear binding may occur. Also, particles with very high energies in the jets are able to leave the detector. Therefore the energy corrections applied to jets are more complicated than for electrons or muons.

The electromagnetic shower component of the jet is expected to be well described (cf. electrons). Therefore the calibration of the jet energy is done with respect to the electromagnetic scale and then applied to the hadronic component via scale factors. The calibration scheme which is applied to jets used in this thesis is called EM+JES and follows three steps. First, a correction to account for pile-up is applied to the energy measured in the calorimeter. In a second step, a correction on the jet direction is applied in such a way, that the jet originates from the primary vertex of the interaction and not the geometrical center of the detector. Third, the jet calorimeter energy and position are corrected by applying correction factors derived from studies comparing reconstructed jets with truth jets from MC simulations.

A correction on the energy resolution is not needed, since it is already well described by Monte Carlo [26].

Taus

Since τ_h are reconstructed from jets, the calibration of jet energies mentioned above, has already been applied. On top of that an additional calibration is needed to restore the τ_h energy scale (TES). Simulated $Z \rightarrow \tau\tau$ and $W \rightarrow \tau\nu$ events are used to derive the TES. From those samples, only τ_h candidates which pass loose ID criteria (cf. Section 4.1.6) and can be matched to a true τ_h are used to derive calibration constants and corrections. These corrections depend on the reconstructed τ_h energy, η and the number of prongs and are applied to the energy and direction of the τ_h [27].

4.1.8 Reconstruction of missing transverse energy (MET)

Neutrinos leave the detector unnoticed, other particles may leave the detector undetected under large angles. These particles cause a momentum imbalance in the detector. This missing

transverse momentum is calculated via the negative vector sum of all object momenta in the event. The *missing transverse energy* (MET or E_T^{miss}) corresponds to the norm of the missing transverse momentum.
The E_T^{miss} is defined as

$$E_T^{miss} = \sqrt{\left(E_x^{miss}\right)^2 + \left(E_y^{miss}\right)^2}. \tag{4.9}$$

The missing energy component in x (y) direction is calculated as the sum over the $E_{x(y)}^{miss,j}$ components of all objects j ($j = e, \mu, \tau, \gamma$, jets) in the calorimeter as well as the missing energy components $E_{x(y)}^{miss,CellOut}$ of the calorimeter cells which have not been assigned to a reconstructed object and $E_{x(y)}^{miss,\mu(MS)}$ of the MS, respectively.

$$E_{x(y)}^{miss} = \sum_j E_{x(y)}^{miss,j} + E_{x(y)}^{miss,CellOut} + E_{x(y)}^{miss,\mu(MS)}. \tag{4.10}$$

The component $E_{x(y)}^{miss,\mu}$ is only considered if the muon is not isolated (i.e. $\Delta R(jet,\mu) < 0.3$). All terms in equation 4.10 are calculated via

$$E_x^{miss,k} = -\sum_i E_i \sin\theta_i \cos\phi_i, \tag{4.11}$$

$$E_y^{miss,k} = -\sum_i E_i \sin\theta_i \sin\phi_i, \tag{4.12}$$

where k corresponds to term k in equation 4.10, θ_i and ϕ_i are the polar and azimuthal angle and E_i the calibrated energy of calorimeter cell i. [28]

4.2 The Pi0Finder algorithm

The *Pi0Finder* algorithm has been developed in Ref. [29] and validated in Ref. [30]. It aims to provide information about neutral pions in the τ_h decay.
The algorithm sets in after the τ_h has been reconstructed as described above (cf. Section 4.1.6). It uses the tracking system and calorimeter clusters which have been assigned to the τ_h. The Pi0Finder algorithm has two distinct features. On the one hand it aims at the reconstruction of the visible τ_h mass by treating certain calorimeter clusters of the τ_h as *π^0-clusters*. On the other hand the number of neutral pions (π^0s) in the τ_h decay is evaluated.

4.2.1 π^0 counting

Neutral pions decay through the electromagnetic interaction into two photons in approximately 99% of all decays, whereas charged pions decay through the weak interaction. Therefore the lifetime of a π^0 is with approximately 10^{-17} s much shorter than the lifetime of charged pions ($\tau_{\pi^\pm} \approx 10^{-8}$ s) [4]. As a result neutral pions deposit most of their energy in the early layers of the electromagnetic calorimeter. Therefore the fraction of calorimeter energy found in the pre-sampler and strip layers ($E_{\mathrm{PPS}}/E_{\mathrm{calo}}$) is higher for τ_h decays including neutral pions (cf. Fig. 4.2, top left plot). For the same reason, the number of cells in the

n_{π^0}	primary BDT score	secondary BDT score
0	$\text{score}_{\text{BDT1}} \geq 0.465$	-
1	$\text{score}_{\text{BDT1}} < 0.465$	$\text{score}_{\text{BDT2}} \geq 0.565$
2	$\text{score}_{\text{BDT1}} < 0.465$	$\text{score}_{\text{BDT2}} < 0.565$

Table 4.2: Definition of the number of π^0s (n_{π^0}) through the primary and secondary BDT score. [29]

strip layer with energy depositions above 200 MeV (N_{strip}) is higher for τ_h decays including neutral pions (cf. Fig. 4.2, top right plot). Also the ratio of the $\pi^{\pm}$ energy to the energy measured in the EM calorimeter ($(E_{\text{track sys}} - E_{\text{hCal}})/E_{\text{EMcal}}$) is higher for τ_h decays without π^0s, since relatively more energy of the τ_h is available for the charged pions (cf. Fig. 4.2, middle left plot). For the same reason the ratio of the momentum measured in the EMcal to the track momentum ($p_{\text{EM}}/p_{\text{track sys}}$) is higher for τ_h decays including π^0s (cf. Fig. 4.2, middle right plot). The ratio of the transverse energy to the transverse momentum of the leading track ($E_T/p_{T,\text{ lead}}$) is low for τ_h decays including one or two pions (1-prong, 1-prong+1π^0) and higher for τ_h decays including more pions (1-prong+2π^0s, 3-prong, 3-prong+1π^0) (cf. Fig. 4.2, bottom plot).

These five variables are used by two different BDTs in order to evaluate the number of π^0s in a τ_h decay. The primary BDT (BDT1) is trained on simulated τ events including π^0s (signal) and without π^0s (background). It distinguishes between τ_h decays including or not including π^0s with a signal efficiency of 81.8% and background rejection of 82.4%, respectively. The secondary BDT (BDT2) distinguishes between 1-prong τ_h decays including one (signal) or two π^0s (background) and is only used if π^0s have been found by BDT1. BDT2 has a signal efficiency of 59.8% and a background rejection of 54.5%. It has only been optimized on 1-prong τ_h events. Since 1-prong τ_h decays involving more than two π^0s as well as 3-prong τ_h decays involving more than one π^0 are rare (cf. Table 4.1), this is a reasonable simplification.

The number of π^0s (n_{π^0}) is defined over the value of the primary and secondary BDT score, as listed in Table 4.2.

4.2.2 Mass reconstruction of the visible τ_h

The mass reconstruction of the visible τ_h is based in the track measurement, which corresponds to a measurement of the charged pions in the τ_h decay, and on the clusters in the calorimeter system which are identified as neutral pions.

A correction for noise, underlying event (U.E.) and pile-up is applied to all calorimeter clusters which have been associated to the τ_h by the reconstruction algorithm (cf. Section 4.1.6). The clusters surviving the correction are inspected further by the Pi0Finder algorithm, which chooses the cluster or pair of clusters which has the highest resemblance to a π^0. The quality of the resemblance is expressed by the π^0 *likeness score*:

$$\pi^0\text{-likeness score} = \frac{E^{\text{PPS}}_{\text{cluster(s)}}}{f^{\text{HAD}}_{\text{cluster(s)}} + x\sqrt{\left|\frac{E_{\text{cluster(s)}}}{E_{\text{calo}} - E_{\text{tracks}}}\right|}}, \qquad (4.13)$$

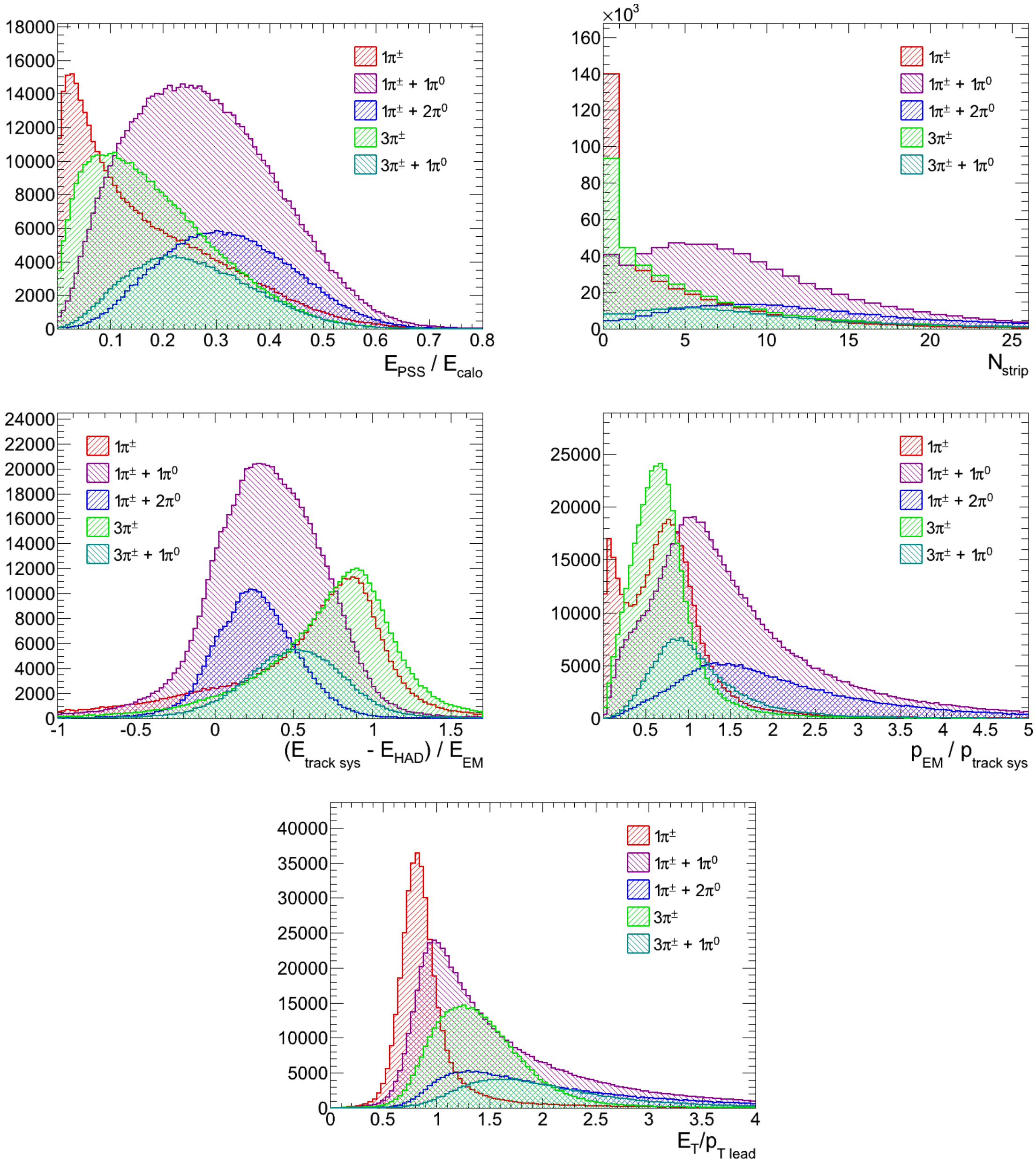

Figure 4.2: Pi0Finder BDT input variables. Top left: fraction of calorimeter energy found in the pre-sampler and strip layers. Top right: number of cells in the strip layer with energy depositions above 200 MeV. Middle left: ratio of the $\pi^\pm$ energy to the energy measured in the EM calorimeter. Middle right: ratio of the momentum measured in the EMcal to the track momentum. Bottom: ratio of the transverse energy to the transverse momentum of the leading track [29].

where E^{PPS} and $f^{\mathrm{HAD}}_{\mathrm{cluster(s)}}$ are the energy fraction of the selected cluster(s) in the hadronic calorimeter or inner detector respectively. $E_{\mathrm{cluster(s)}}$, E_{calo} and E_{tracks} corresponds to the energy of the selected cluster(s), the energy deposited in the calorimeter system and the energy of the track system, respectively. The adjusting factor x has no physical meaning. The cluster or pair of clusters with the highest π^0-likeness score is chosen.
The visible τ_h is reconstructed by adding the four-momenta of the π^0 cluster(s) and the track system

$$\mathbf{p}_{\tau_{vis}} = \mathbf{p}_{\mathrm{cluster(s)}} + \mathbf{p}_{\mathrm{track\ sys}}. \tag{4.14}$$

The four momenta of the cluster(s) $\mathbf{p}_{\mathrm{cluster(s)}}$ and track system $\mathbf{p}_{\mathrm{track\ sys}}$, respectively, are build with the corresponding p_T, η, ϕ and m, with $m = 140\,\mathrm{MeV}$ for the track system (i.e. $\pi^{\pm}$ system) and $m = 135\,\mathrm{MeV}$ for the cluster(s) (i.e. π^0 system). The mass or other kinematic variables of the visible τ_h are then taken from the resulting four momentum.
It should be noted that since π^0 cluster(s) are chosen in every τ_h event, the number of cluster(s) is not necessarily correlated to the number of π^0s found by the Pi0Finder counting algorithm [29] [31].

The validation of the Pi0Finder algorithm has been performed for loose, medium and tight BDT selected 1-prong and 3-prong τ_h candidates. Non-$Z \rightarrow \tau\tau$ background subtracted data has been compared to $Z \rightarrow \tau\tau$ Monte Carlo in a $Z \rightarrow \tau\tau$ control region. The Monte Carlo predictions have been found to be in good agreement with the data for the π^0 counting as well as the τ_h transverse momentum reconstruction without further calibration [30] [32].

5 Overview of the $H \rightarrow \tau_l \tau_h$ analysis

The Higgs-boson search in the $H \rightarrow \tau^+\tau^-$ decay mode is divided into three subchannels ($H \rightarrow \tau_l\tau_l$, $H \rightarrow \tau_l\tau_h$ and $H \rightarrow \tau_h\tau_h$) because of their distinct final-state dependent background compositions [20]. In this chapter the $H \rightarrow \tau_l\tau_h$ analysis is introduced, which is used as a reference and on which this thesis is based. The complete $H \rightarrow \tau_l\tau_h$ reference analysis is described in great detail in Ref. [33], only a short overview is given here.

5.1 Event selection

This thesis and the reference analysis use proton-proton collision data with an integrated lumnosity of $13\,\text{fb}^{-1}$ collected at a center-of-mass energy of $\sqrt{s} = 8\,\text{TeV}$, corresponding to the running periods A-E5 of 2012 [33].

5.1.1 Pre-selection

To cope with the vast amount of interactions, triggers are used to filter for interesting events in a first step. In order to increase the signal yield with respect to the analysis performed on the $\sqrt{s} = 7\,\text{TeV}$ data set which only used a single-lepton trigger (cf. Ref. [34]), two triggers with different lepton thresholds are used to pre-select events for the current analysis. A combined lepton+tau trigger (LTT) and a single-lepton trigger (SLT). The LTT triggers on isolated electron (muon) candidates with a transverse momentum of $p_T(e) > 18\,\text{GeV}$ ($p_T(\mu) > 15\,\text{GeV}$) and a τ_h with $E_T > 20\,\text{GeV}$. The SLT has a higher lepton threshold, it triggers on events with an isolated electron or muon with $p_T(e,\mu) > 24\,\text{GeV}$. Offline, only SLT events are considered for high lepton p_T and only LTT events are considered for low lepton p_T events. In addition, the event is required to have a vertex with at least four tracks. An Overlap removal on the reconstructed muon, electron, τ_h and jet candidates is conducted in this order. Also $e\tau_h$ events with $1.37 \leq |\eta_e| \leq 1.52$ are discarded, due to inefficient regions in the Liquid Argon calorimeter.

Pre-selection cuts are applied on all events passing the trigger. The electron and muon candidates are required to pass the following isolation cuts: $E_T^{\text{cone}}(R_0 = 0.2) < 0.06 \cdot E_T^{\text{corr}}$ and $p_T^{\text{cone}}(R_0 = 0.4) < 0.06 \cdot p_T^{\text{corr}}$ (cf. Section 4.1.4). Also, electron (muon) candidiates are required to pass the tight++ (CombinedMuon) identification requirement (cf. Section 4.1.2). Exactly one isolated electron (muon) with $20 < p_T(e) < 26\,\text{GeV}$ ($17 < p_T(\mu) < 26\,\text{GeV}$) and exactly one identified τ_h with $p_T(\tau) > 25\,\text{GeV}$ are required for events passing the LTT. For events passing the SLT exactly one isolated electron or muon with $p_T > 26\,\text{GeV}$ and exactly one identified τ_h with $p_T(\tau) > 20\,\text{GeV}$ are required. A di-lepton veto is applied to suppress contributions from $Z \rightarrow ee, \mu\mu, t\bar{t}$ and Wt (single top) events. However, the isolation requirements are dropped and only loose identification criteria are applied for a higher efficiency of the di-lepton veto. Also the lepton and τ_h are required to have opposite charge.

5.1.2 Event categorization

After pre-selection, all remaining events are categorized to increase the signal to background ratio. The VBF category (see below), for example, has a very distinct signal signature due to the VBF Higgs-boson production mode which can be exploited to increase the signal to background ratio. In general the categorization is oriented on the number of high p_T jets in the event and all quality criteria are listed in Ref. [33].
This thesis aims at increasing the sensitvity of the 0- and 1-jet category by splitting them into subcategories using the information of the hadronic τ decay. The $H \rightarrow \tau_l\tau_h$ analysis categories used by the reference analysis are listed in the following.

VBF category: $H \rightarrow \tau\tau$ events, where the Higgs was produced via the vector boson fusion (VBF, cf. Section 2.2.2) result in a characteristic detector signature, including two high-p_T jets in the forward region of the detector. Those jets are used as *tagging* jets. At least two jets with $p_T(jet_1) > 40\,\text{GeV}$ and $p_T(jet_2) > 30\,\text{GeV}$ are required for this category as well as a τ_h with a $p_T(\tau) > 30\,\text{GeV}$ and missing energy of $E_T^{miss} > 20\,\text{GeV}$. Quality cuts on the pesudo-rapidity η and the dijet-mass are applied, since the jets in $pp \overset{VBF}{\rightarrow} H$ events have a large seperation in η. Also the $H \rightarrow \tau\tau$ decay products are expected to lie between the tagging jets.
Due to the low statistics in this category, the electron ($e\tau_h$) and muon ($\mu\tau_h$) final states are combined.

Boosted category: All events that fail the VBF category, are considered for the boosted category.
Additional high-p_T jets in the event result typically in a boosted Higgs boson in the transverse plane. Therefore, the Higgs-boson p_T is reconstructed and quality cuts are applied on the reconstructed Higgs-boson $p_T(H)$. The $p_T(H)$ is calculated using the transverse momentum of the lepton and the τ_h as well as the missing transverse energy E_T^{miss} to account for neutrinos. This especially improves the seperation between the Higgs signal and the irreducible $Z \rightarrow \tau\tau$ background.
As for the VBF category, the electron and muon final states are combined for the boosted category because of low statistics.

1-jet category: All events that fail the VBF and Boosted category are considered for the 1-jet category. In addition, at least one jet with $p_T > 30\,\text{GeV}$ and a missing transverse energy of $E_T^{miss} > 20\,\text{GeV}$ are required.
The high statistics in this category allow a seperate consideration of the electron and muon final states.

0-jet category: All pre-selected events which have failed the above categorys and have no jets with a transverse momentum $p_T > 30\,\text{GeV}$ as well as a missing energy of $E_T^{miss} > 20\,\text{GeV}$ are included in this category.
As for the 1-jet category the high statistics allow a seperate consideration of the electron and muon final states.

After the categorization additional requirements to further reduce the different backgrounds are applied to each analysis category. All requirements are listed in Ref. [33]. Here only those for the 0- and 1-jet category are introduced, since this thesis aims at an increase in

0-jet	1-jet
$m_T(l, E_T^{miss}) < 30\,\mathrm{GeV}$	$m_T(l, E_T^{miss}) < 50\,\mathrm{GeV}$
$\sum\Delta\phi < 3.5$	$\sum\Delta\phi < 3.5$
$\Delta(\Delta R) < 0.5$	$\Delta(\Delta R) < 0.6$
$Z \rightarrow ll$ rejection cuts	$Z \rightarrow ll$ rejection cuts
$p_T(l) - p_T(\tau) < 0$	

Table 5.1: Additional cuts applied to the 0- and 1-jet categories after categorization [33].

sensitivity in these high statistic categories by splitting them further into subcategories (cf. chapter 6). The additional cuts applied to the 0- and 1-jet categories are listed in table 5.1 and explained below.

The in table 5.1 listed requirements are applied to supress the contributions of fake τs.

$m_T(l, E_T^{miss})$: The *transverse mass* of the lepton and the missing transverse energy

$$m_T(l, E_T^{miss}) = \sqrt{2p_T(l)E_T^{miss}\left(1 - \cos\Delta\phi(p_T(l), E_T^{miss})\right)}, \tag{5.1}$$

discriminates especially well against the $W \rightarrow e/\mu + \nu$ background. W events usually have a transverse mass m_T that peaks in the mass region right below the W-mass, therefore events with $m_T > 70\,\mathrm{GeV}$ are chosen for a W control region (WCR). Since $m_T(l, E_T^{miss})$ is lower for the signal, events with a low transverse mass ($m_T(l, E_T^{miss}) < 30/50\,\mathrm{GeV}$) are chosen for the signal region (SR).

$\sum\Delta\phi$: Due to the E_T^{miss} vector usually lying between the p_T vectors of the lepton and the τ_h for the Higgs-boson signal, the sum

$$\sum\Delta\phi = |\phi(l) - \phi(E_T^{miss})| + |\phi(\tau) - \phi(E_T^{miss})| \tag{5.2}$$

is usually smaller for $H \rightarrow \tau\tau$ events than for W+jets events. For W+jets events $\sum\Delta\phi$ can be larger than π.

$\Delta(\Delta R)$: The angular seperation ΔR of a di-τ system depends on the boost this system has experienced by its mother particle. A correlation between ΔR and the transverse momentum of the lepton-τ-pair ($p_T(l, \tau)$) for resonance $\tau\tau$-systems (from $H \rightarrow \tau\tau$ or $Z \rightarrow \tau\tau$) can be observed. This correlation is modeled for $H \rightarrow \tau\tau$ decays and depending on $p_T(l, \tau)$ an expected angular seperation $\Delta R^{\text{pred.}}$ can be predicted.

The ΔR for non-resonant backgrounds deviates from the expected $\Delta R^{\text{pred.}}$. Therefore $\Delta(\Delta R)$ is defined as the difference between the predicted and the measured angular seperation:

$$\Delta(\Delta R) = |\Delta R^{\text{meas.}} - \Delta R^{\text{pred.}}|, \tag{5.3}$$

which is higher for fake τ_h backgrounds than for $H \rightarrow \tau\tau$ and $Z \rightarrow \tau\tau$.

$Z \rightarrow ll$ rejection cuts: The $Z \rightarrow ll$ background can be supressed by applying dedicated cuts depending on the lepton and its ability to fake a τ.

Muons are minimal ionizing particles and therefore deposit only little amounts of energy in the calorimeter system. Even muons with high amounts of bremsstrahlung

have a small electromagnetic fraction f_{EM}[1]. Therefore the cut $f_{EM} > 0.1$ is applied to 1-prong muon events if the invariant mass of the muon and the associated track lies within the Z-mass window ($80 < m_{inv}(\mu,\text{track}) < 100\,\text{GeV}$).
Since the $Z \to \mu\mu$ background component is only of noteworthy importance in the 0-jet category, $Z \to \mu\mu$ rejection cuts are not applied to the other categories.
Due to a deficit in TRT and calorimeter information in the central region of the detector, 1-prong τ candidates within $|\eta_{\text{track}}| < 0.05$ are rejected for the 0- and 1-jet categories.

$p_T(l) - p_T(\tau)$: For $Z \to \tau\tau$ and $H \to \tau\tau$ events the lepton originates from a τ decay which also includes two neutrinos. Therefore the p_T asymmetry between the lepton and the τ_h peaks at negative values for those two processes ($p_T(l) - p_T(\tau) < 0$) and offers another possibility to suppress the multijet and W+jets backgrounds in the 0-jet category. [33]

5.2 Mass reconstruction of the di-tau system

The mass reconstruction of the $\tau_l\tau_h$ system is not trivial, since two neutrinos from the τ_l and one neutrino from the τ_h decay escape the detector. Therefore the so-called *missing mass calculator* (MMC) is used to reconstruct the invariant $\tau\tau$ mass. The MMC di-tau mass reconstruction method is explained in greater detail in Ref. [33] , here only the MMC principle is introduced.
In order to provide a full reconstruction of the event topology, the MMC has to solve an underconstraint equation system for the invisible momentum components of the neutrino(s) from each τ decay (τ_l and τ_h) and the invariant mass of the di-neutrino system of the leptonic τ decay.
Although a definite solution of the underconstraint system is not possible, some solutions are more likely than others. The MMC tries to find the most probable solution using additional information about the τ decay kinematics. In the current implementation of the MMC, the 3-dimentional angle $\Delta\theta_{3D}$ between the (in)visible τ decay products is used. The $\Delta\theta_{3D}$ is calculated from data for all points in the $(\phi_{\text{mis1}}, \phi_{\text{mis2}})$ parameter space.
As a reference, $\Delta\theta_{3D}$ distributions are obtained from simulated $Z/\gamma^* \to \tau\tau$ events in a $p_T(\tau)$ range from $10\,GeV < p_T(\tau) < 230\,GeV$. The simulated $\Delta\theta_{3D}$ distributions are fitted with a combination of Gaussian and Landau functions, and propability density functions $\mathscr{P}(\Delta\theta_{3D}, p_T(\tau))$ are derived for each τ decay type (τ_l, $\tau_h^{\text{1-prong}}$, $\tau_h^{\text{3-prong}}$). The $\mathscr{P}(\Delta\theta_{3D}, p_T(\tau))$ for both τs in the decay are multiplied to derive an overall event probability $\mathscr{P}_{\text{event}}$.
For all scanned points in the $(\phi_{\text{mis1}}, \phi_{\text{mis2}})$ parameter space, the di-τ mass is calculated and weighted by the event propability $\mathscr{P}_{\text{event}}$. The maximum of the di-$\tau$ mass (m_{MMC}) distribution is used as final estimate of the di-τ mass.

---

[1] The electromagnetic fraction f_{EM} is the fraction of the transverse energy of the τ candidate which has been deposited in the EM calorimeter.

5.3 Background estimation

In order to extract the Higgs-boson signal out of the vast amount of events, it is crucial to understand all relevant background processes and their power to fake the $H \to \tau\tau \to l + \tau_h + 3\nu$ signal signature. The signature of the signal can be faked in three ways: if the event has a true or fake lepton and a true τ_h or the τ_h is either faked by a lepton or a jet. The fake signature depends on the background process. The corresponding backgrounds to the three just mentioned possibilities to fake the $H \to \tau\tau$ signature are introduced in the following.

True lepton + true τ_h: The most prominent background with this signature is the $Z/\gamma^* \to \tau\tau$ decay, which has the same final state and similar event kinematics as the $H \to \tau\tau$ decay. A smaller contribution to this background category comes from di-boson production if both bosons decay leptonically ($VV \to l+\tau_h+X$ with $VV = ZZ, WW, WZ$)[2]. The top background contributes to this category, if both top quarks from a $t\bar{t}$ production process decay to leptonic final states via a W boson
($t\bar{t} \to W^+bW^-\bar{b} \to l + \tau_h + X$). The single top production in association with a W boson reaches a similar final state, if the W from the top decay as well as the W from the associated production decay leptonically.
All those processes show a strong charge correlation of the lepton and the τ_h, which have opposite charge in the great majority of times. Therefore the number of events where the lepton and the τ_h have opposite charge, N_{OS} greatly exceeds the number of events N_{SS} where both have the same charge: $N_{OS} \gg N_{SS}$[3].

True lepton + τ_h faked by lepton: This category is largely dominated by $Z \to ll$ processes if one of the leptons from $Z/\gamma^* \to ee/\mu\mu$ fakes the τ_h.
Due to the Z/γ^* which are neutral, this background shows a very strong charge correlation: $N_{OS} \gg N_{SS}$.

True/fake lepton + τ_h faked by a jet: A major contribution to this background category comes from QCD jet processes, which have a large production cross section. The τ_h is faked by a QCD jet and the lepton can either also be faked by a jet or result from a semi-leptonic decay of hadrons. However, leptons originating from a semi-leptonic decay of hadrons are not isolated, therefore only a small fraction of those pass the by the analysis required isolation cuts. Another contribution comes from W+jets processes, due to the true lepton resulting from the W decay and a jet faking the τ_h. If the jet which fakes the τ_h originates from the same quark that has radiated the W, the charges of the lepton from the W decay and of the fake τ_h are correlated ($N_{OS} > N_{SS}$). However, if the quark which has radiated the W also radiates a gluon, and that gluon is the origin of the τ-fake jet, no charge correlation is expected.
Also, the resulting jet from a hadronically decaying W boson or a B-hadron from a $t\bar{t}$ decay can fake a τ_h. In addition the τ_h can be faked by a W associated single top process where one of the W bosons decays hadronically and fakes the τ_h.

---

[2] The X stands for all other decay products, which are not relevant for the characteristic signature and therefore are not listed.

[3] OS (SS) stands for **O**pposite (**S**ame) **S**ign

Other contribuions come from $Z/\gamma^* + jets \to ee/\mu\mu + jets$ processes if a jet is misidentified as a τ_h, or from di-boson processes where one boson decays hadronically and one of the resulting jets fakes the τ_h.
The charge correlation between lepton and τ_h is small for QCD, W+jets or top processes and non-existent for Z+jets or di-boson contributions.
[33]

5.3.1 Method

The background estimation is based on two major assumptions: the shape of the m_{MMC} distribution is the same for OS and SS events and the MC-to-data scale factor ($k = {}^{N_{\text{data}}}/_{N_{\text{MC}}}$) is the same for the signal and control region of a given background. Using those two assumptions, the number of expected OS background events N_{OS}^{bkg} can be estimated by the formula

$$N_{OS}^{bkg} = r_{QCD} \cdot N_{SS}^{data} + N_{\text{Add-on}}^{Z\to\tau\tau} + N_{\text{Add-on}}^{Z\to ll(\to\tau)} + N_{\text{Add-on}}^{Z\to ll+jet(\to\tau)} + N_{\text{Add-on}}^{W+jets} + N_{\text{Add-on}}^{top} + N_{\text{Add-on}}^{VV}. \tag{5.4}$$

All components of equation 5.4 are explained in the following. However, the derivation of r_{QCD} and the used k-faktors is not explained (except for the W+jets background), since it is not crucial for this thesis and has been done in great detail in Ref. [33] and Ref. [34].

$r_{QCD} \cdot N_{SS}^{data}$: The same sign components of all backgrounds are included in N_{SS}^{data} which stands for all same sign data events that pass all events selection cuts except the OS requirement. Since QCD events are practically impossible to predict via MC simulation, N_{SS}^{data}, which has a significant contribution of QCD events, is used to estimate the QCD background component. Different charge correlations are expected for QCD-jets originating from di-quark or di-gluon/quark-gluon parton pairs, respectively. This can lead to differences in the number of OS and SS QCD-events, which is accounted for by the correction factor $r_{QCD} = {}^{N_{OS}^{QCD}}/_{N_{SS}^{QCD}}$.

$N_{\textbf{Add-on}}^{Z\to\tau\tau}$: Since the same sign components of all backgrounds are included in N_{SS}^{data}, only the $N_{\text{Add-on}}^{bkg_i} = N_{OS}^{bkg_i} - N_{SS}^{bkg_i}$ components are added to obtain the OS number of events of the corresponding background. The $Z \to \tau\tau$ add-on curve is estimated via $N_{\text{Add-on}}^{Z\to\tau\tau} = k_{Z\to\tau\tau} \cdot \left(N_{OS}^{Z\to\tau\tau} - r_{QCD} \cdot N_{SS}^{Z\to\tau\tau}\right)$. The $Z \to \tau\tau$ background is estimated with MC, which proves to be a very good estimation [33]. Therefore, $k_{Z\to\tau\tau}$ is assumed to be equal to unity.

$N_{\textbf{Add-on}}^{Z\to ll(\to\tau)}$: The data-driven estimate of the $Z \to ll(\to \tau)$ background is described in Ref. [33] and Ref. [34]. Again the $k_{Z\to ll(\to\tau)}$ factor in $N_{\text{Add-on}}^{Z\to ll(\to\tau)} = k_{Z\to ll(\to\tau)} \cdot \left(N_{OS}^{Z\to ll(\to\tau)} - r_{QCD} \cdot N_{SS}^{Z\to ll(\to\tau)}\right)$ is assumed to be equal to unity.

$N_{\textbf{Add-on}}^{Z\to ll+jet(\to\tau)}$: Since τ_h fakes from jets are not expected to have any charge correlation with a lepton from the $Z \to ll$ decay and in addition no significant statistical difference is observed between OS and SS events for this background, $N_{\text{Add-on}}^{Z\to ll+jet(\to\tau)}$ reduces to $N_{\text{Add-on}}^{Z\to ll+jet(\to\tau)} = k_{Z\to ll+jet(\to\tau)} \cdot N_{OS}^{Z\to ll+jet(\to\tau)} \cdot (1 - r_{QCD})$.

$N^{W+jets}_{\textbf{Add-on}}$: The τ_h misidentification rate is different for quark or gluon initiated jets and the OS requirement leads to different quark-gluon fractions in OS and SS events. Therefore seperate k-factors have to be applied to OS and SS events: $N^{W+jets}_{\text{Add-on}} = k^{OS}_{W+jets} \cdot N^{W+jets}_{OS} - r_{QCD} \cdot k^{SS}_{W+jets} \cdot N^{W+jets}_{SS}$. The W k-factors are derived in W enriched control regions (WCR) (cf. [33]).

The WCRs are defined depending on the analysis categories by changing the transverse mass cut to $m_T > 70\,\text{GeV}$ since W events show high transverse masses (cf. section 5.1.2). Also, cuts applied after categorization to suppress the W+jets background are not applied (i.e. no cuts on $\Delta(\Delta R)$ and $\sum \Delta\phi$ for the 0- and 1-jet categories). In those WCRs the W MC predictions are compared to non-W subtracted data to derive the k_W factors:

$$k_W = \frac{n^{\text{data}} - n^{MC}_{\text{non-W}}}{n^{MC}_{W}}. \tag{5.5}$$

Where the non-W background components are taken directly from MC. This is done seperately for OS and SS events. The k_W factors for the 0- and 1-jet categories are taken from [33] and listed in table 5.2.

	category			
	0-jet $e\tau_h$	0-jet $\mu\tau_h$	1-jet $e\tau_h$	1-jet $\mu\tau_h$
k_W^{OS}	0.614 ± 0.010	0.581 ± 0.009	0.656 ± 0.014	0.557 ± 0.011
k_W^{SS}	0.739 ± 0.023	0.717 ± 0.024	0.859 ± 0.028	0.710 ± 0.024

Table 5.2: The k_W factors for the 0- and 1-jet $e\tau_h/\mu\tau_h$ categories, with statistical uncertainties [33].

The k_W factors from table 5.2 are taken as a reference for a study on the impact of seperate k_W factors on the data to MC agreement in 0- and 1-jet subcategories which is explained in Section 6.1.3.

$N^{top}_{\textbf{Add-on}}$: As for the W+jets background, different k-factors have to be applied for OS and SS events: $N^{top}_{\text{Add-on}} = k^{OS}_{top} \cdot N^{top}_{OS} - r_{QCD} \cdot k^{SS}_{top} \cdot N^{top}_{SS}$. The top k-factors are also derived in a MC-based background estimation technique using top enriched control regions [33].

$N^{VV}_{\textbf{Add-on}}$: The di-boson events only make up a very small fraction of the baseline event sample ($\sim$0.5%) and it is valid to rely entirely on the MC-simulation for the di-boson background estimation. Therefore, the di-boson k-factor K_{VV} is assumed to be equal to unity: $N^{VV}_{\text{Add-on}} = k_{VV} \cdot \left(N^{VV}_{OS} - r_{QCD} \cdot N^{VV}_{SS}\right)$ [33].

5.4 Systematic uncertainties

In the search for the Higgs boson, the signal appears as an excess of data over the simulated background. However, if the background is not well known one cannot be certain about a possibly observed excess of data. The simulation of the background is influenced by several parameters. For example the behaviour of the trigger efficiencies might be different in simulation and real data, therefore the differences are used to correct for mismodelings. Other corrections are applied on the object-identification efficiencies, energy scales and resolutions. Also the theoretically derived cross sections are not exact, which directly effects the number of simulated events and therefore the estimation of the background. To account for the imprecisions of those corrections and predictions, systematic uncertainties are assigned. These systematic uncertainties are propagated to the analysis, by running the analysis once with the nominal values of the corrections, and then again twice for every source of systematic uncertainty where the concerned parameter is scaled up and down by $\pm 1\sigma$ of the systematic uncertainty.

All systematic uncertainties used by the reference analysis as well as this thesis for 0-/1-jet events are briefly described below. A detailed survey of all systematic uncertainties can be found in Ref. [33].

Systematic uncertainties on the luminosity and cross section

The expected event numbers are derived from MC simulation by normalizing them with the according next-to-next-to-leading order (NNLO) cross section and the total integrated luminosity:

$$N_{\text{exp}} = N_{\text{MC}} \cdot w \qquad \text{with } w = \frac{\sigma \cdot \int \mathscr{L} dt}{N_{\text{MC}}}. \tag{5.6}$$

The systematic uncertainties on the cross section, due to higher order corrections which are not considered, have to be derived seperetaly for each jet category. Since it has been shown that the cross-section uncertainties for the exclusive jet categories are underestimated, they are derived from the cross-section uncertainties for the inclusive jet categories [35]. This is done by calculating the cross section for the exlusive jet category by subtracting the cross section for inclusive jet bins from the total cross section (e.g. $\sigma_{\text{0-jet}} = \sigma_{\text{tot}} - \sigma_{\geq 1}$) and propagating the uncertainty accordingly.

The overall theory uncertainties on the event selection are found to be of the order of a few percent, except for the ggF Higgs-boson production mode which is especially sensitiv to higher order corrections, where it is of the order of 20%. For the total integrated luminosity of $\int L = 13\,\text{fb}^{-1}$ a systematic uncertainty of 3.6% was assigned.

Systematic uncertainties on the trigger efficiencies

For the SLT the uncertainties are of the order of 1-2%.

The efficiency scale factors on the τ-leg of the LTT have higher uncertainties, which depend on the running period and detector region. They range from 2-5% for 1-prong τs and from 4-12% for 3-prong τs. The scale factors for the lepton and τ leg of the LTT are multiplied and the uncertainties propagated to the overall scale factor.

The final effect of the trigger uncertainties on the analysis is very small ($\mathscr{O}(2\%)$).

Systematic uncertainties considered for electrons

For electrons, systematic uncertainties on the energy scale and resolution, the reconstruction and identification efficiency and on the calorimeter isolation are considered.

A 1-3% energy scale uncertainty is assigned, depending on the detector region. Also a 1-4% energy resolution smearing is applied to simulated events, since the energy resolution is not correctly reproduced by MC simulations. The impact of the electron reconstruction and identification uncertainty on the event selection acceptance is evaluated by varying the corresponding scale factor by 3%. In a similar way the effect of the calorimeter isolation on the event selection acceptance is estimated by varying the scale factor by 2-4% depending on the transverse momentum of the electron.

Overall the systematic uncertainties for electrons in $e\tau_h$ events are in the range 1-7% depending on the process. For $\mu\tau_h$ events electron systematic uncertainties are below 1%.

Systematic uncertainties considered for muons

For muons, systematic uncertainties on the muon momentum resolution and on the muon identification efficiency are considered.

The impact of these two uncertainties on the event selection acceptance is estimated by varying both by 1%. The overall muon systematic uncertainties for $\mu\tau_h$ events are of the order of 3% for all processes. For $e\tau_h$ events they are neglected.

Systematic uncertainties considered for τ_h

For τ_h systematic uncertainties on the τ_h energy scale and on the τ identification efficiency are considered.

The τ_h energy scale uncertainty depends on the τ momentum and ranges from 4.5-2% for 1-prong τs and from 6.5-3% for 3-prong τs with rising transverse momentum. The effect of the τ_h energy scale uncertainty on the event selection acceptance is estimated by smearing all τ_h which pass the selection criteria and the overlap removal accordingly. The τ identification efficiency uncertainties range from 3-10% depending on the number of prongs and $|\eta_\tau|$.

Overall the τ_h energy scale uncertainties range from 1-23% for 0-jet events and from 1-10% for 1-jet events depending on the process.

Systematic uncertainties considered for jets

For jets, systematic uncertainties on the jet-energy scale (JES) are considered. The baseline systematic on the JES which has been used in earlier analyses (cf. Ref. [**?**]) is split up into groups depending on the source of the individual systematic uncertainty to allow for a better treatment of correlations between them.

The baseline JES combines nuisance parameters which, for example, account for mismodelings of high-p_T jets or which have been derived from in-situ analyses. Different systematic uncertainties have to be applied to forward jets, therefore a seperate forward JES is used. Two seperate JES are used to account for in- and out-of-time pile-up effects and another is used to account for contaminations of close-by jets. Also a seperate flavor JES is used to account for the different quark and gluon JES. The flavor JES only applies to light quarks and gluons, therefore a seperate JES is used for b-quark jets.

Both analyses consider the baseline JES as well as the forward and flavor JES. The overall effect of those three systematic uncertainties on the event selection ranges from 1-20% depending on the process and the jet category.

Not considered by the reference analysis but by this thesis, are the effects of in- and out-of-time-pileup effects as well as effects of the b-jet energy scale. However, their overall effect on the event selection is very small.

Systematic uncertainties considered for E_T^{miss}

The E_T^{miss} vector is reconstructed by adding all object dependent $E_T^{miss,\,\mathrm{object}}$ vectors (cf. Section 4.1.8). Therefore, the systematic uncertainties of the e, τ_h-jet and jet energy scale are propagated to E_T^{miss}. In this procedure the uncertainties on the τ_h-jeta and jet energy scale are treated fully correlated.
The overall effect of the E_T^{miss} systematic uncertainties on the event selection acceptance ranges from 1-10% and 1-7% for 0-jet and 1-jet categories, respectively.

Systematic uncertainties considered for the background estimate

The systematic uncertainties considered for the background estimate are listed in Table 5.3 for the 0- and 1-jet categories. Overall, the effect of the systematic uncertainties on the background estimate on the event selection ranges from 1-6% and from 1-20% for the 0- and 1-jet category, respectively.

	Uncertainty in %			
	0-jet		1-jet	
	$e\tau_h$	$\mu\tau_h$	$e\tau_h$	$\mu\tau_h$
r_{QCD}	5.0	7.2	5.0	7.2
k^{OS}_{W+jets}	1.6	1.5	2.1	2.0
k^{SS}_{W+jets}	3.1	3.3	3.2	3.4
$k_{Z\rightarrow ll+jet(\rightarrow\tau)}$	5.4			
k^{OS}_{top}	18	19	18	19
k^{SS}_{top}	22	23	22	23

Table 5.3: Systematic uncertainties considered for the background estimate in the 0- and 1-jet categories [33].

5.5 Results of the $H \rightarrow \tau\tau$ reference analysis

Since no significant excess is observed in the $H \rightarrow \tau^+\tau^-$ search channel an upper limit on the Higgs-boson signal strength $\mu = \sigma/\sigma_{\mathrm{SM}}$ is derived. The limit setting is based on a modified frequentist approach as explained in Ref. [15].
The results of the Higgs-boson search in the $H \rightarrow \tau^+\tau^-$ decay channel on the 4.7 fb^{-1} (2011) and 13 fb^{-1} data set (2012) corresponding to center of mass energies of $\sqrt{s} = 7\,\mathrm{TeV}$ and $\sqrt{s} = 8\,\mathrm{TeV}$, respectively, have been presented in November 2012. In the limit calculation procedure the level of agreement between observed data and expected background for the MMC mass (m_{MMC}) distributions is evaluated. The m_{MMC} distrubutions for all categories contributing to the $H \rightarrow \tau_l \tau_h$ search channel are shown in Fig. 5.1.
To exclude a SM Higgs boson of a certain mass, the *95% Confidence Level* exclusion limit is derived. The limit is given in units of the SM Higgs-boson cross section under the *background-only hypothesis*. In this hypothesis, it is assumed that there is no SM Higgs boson. One can differentiate between the *expected* limit, which is derived by relying purely on simulated events and the *observed* limit which evaluates the level of agreement between

estimated background events and observed data. The value of the (expected) observed limit at a given Higgs-boson mass, corresponds to the (expected) observed signal strength μ of a Higgs boson with that mass. If the expected and observed 95% CL$_s$ limits are below $\mu = 1$ at a given Higgs-boson mass m_H, a SM Higgs boson with mass m_H can be excluded at the 95% CL$_s$.

Figure 5.2 shows the expected and observe 95% CL$_s$ limits for the combination of all $H \to \tau_l \tau_h$ categories (i.e. combination of the 0-jet $e\tau_h$, 0-jet $\mu\tau_h$, 1-jet $e\tau_h$, 1-jet $\mu\tau_h$, Boosted and VBF categories). The observed (expected) 95% CL$_s$ exclusion limits at the $m_H = 125\,\mathrm{GeV}$ mass point are found to be 2.3 (2.3) [33]. Therefore the sensitivity of the analysis does not allow a conclusion on the decay of the discovered boson unto τ leptons.

The 95% CL$_s$ exclusion limits for the $H \to \tau^+\tau^-$ search channel, i.e. the combination of the $H \to \tau_l\tau_l$, $H \to \tau_l\tau_h$ and $H \to \tau_h\tau_h$ analyses are shown in the top plot of Fig. 5.3. At the $m_H = 125\,\mathrm{GeV}$ mass pint the observed (expected) 95% CL$_s$ exclusion limits are found to be 1.9 (1.2) [20]. Therefore the sensitivity of the $H \to \tau^+\tau^-$ analysis does not allow a conclusion on the decay of the discovered boson unto τ leptons. The $H \to \tau^+\tau^-$ analyses has a sensitivity close to $1\sigma/\sigma_{\mathrm{SM}}$. New data or an optimization of the $H \to \tau^+\tau^-$ analysis might allow an exclusion of the SM Higgs-boson cross section in absence of a signal.

The significance of an excess in data is expressed by the so called p_0 value. The p_0 value corresponds to the probability that an observed excess in data is caused by a statistical fluctuation of the background. The expected significance is derived using only simulated events. Convebtion states the observation of a new particle if a significance of 5σ corresponding to a p_0 value of $4 \cdot 10^{-7}$ is observed.

In the bottom plot of Figure 5.3 the expected and observed p_0 curves are shown for the mass range $100\,\mathrm{GeV} < m_H < 150\,\mathrm{GeV}$. Neither the observed nor the expected p_0 curves show high significances, therefore no Higgs-boson signal could be observed in the $H \to \tau^+\tau^-$ decay channel. When fitting the MC estimate to data under the *signal-plus-background hypothesis* the signal strength μ is derived. a signal strength of $\mu = 1$ corresponds to the SM Higgs boson, whereas a signal strength of $\mu = 0$ denotes to a scenario without a SM Higgs boson. Corresponding to the observed p_0 curve in the bottom plot of Figure 5.3 is a signal strength of $\mu = 0.7 \pm 0.7$ [20]. The background-only as well as the signal-plus-background hypotheses corresponding to signal strengths $\mu = 0$ and $\mu = 1$, respectively, lie within uncertainties of the observed signal strength.

The existence of a SM Higgs boson could neither be confirmed nor excluded in the $H \to \tau^+\tau^-$ search channel.

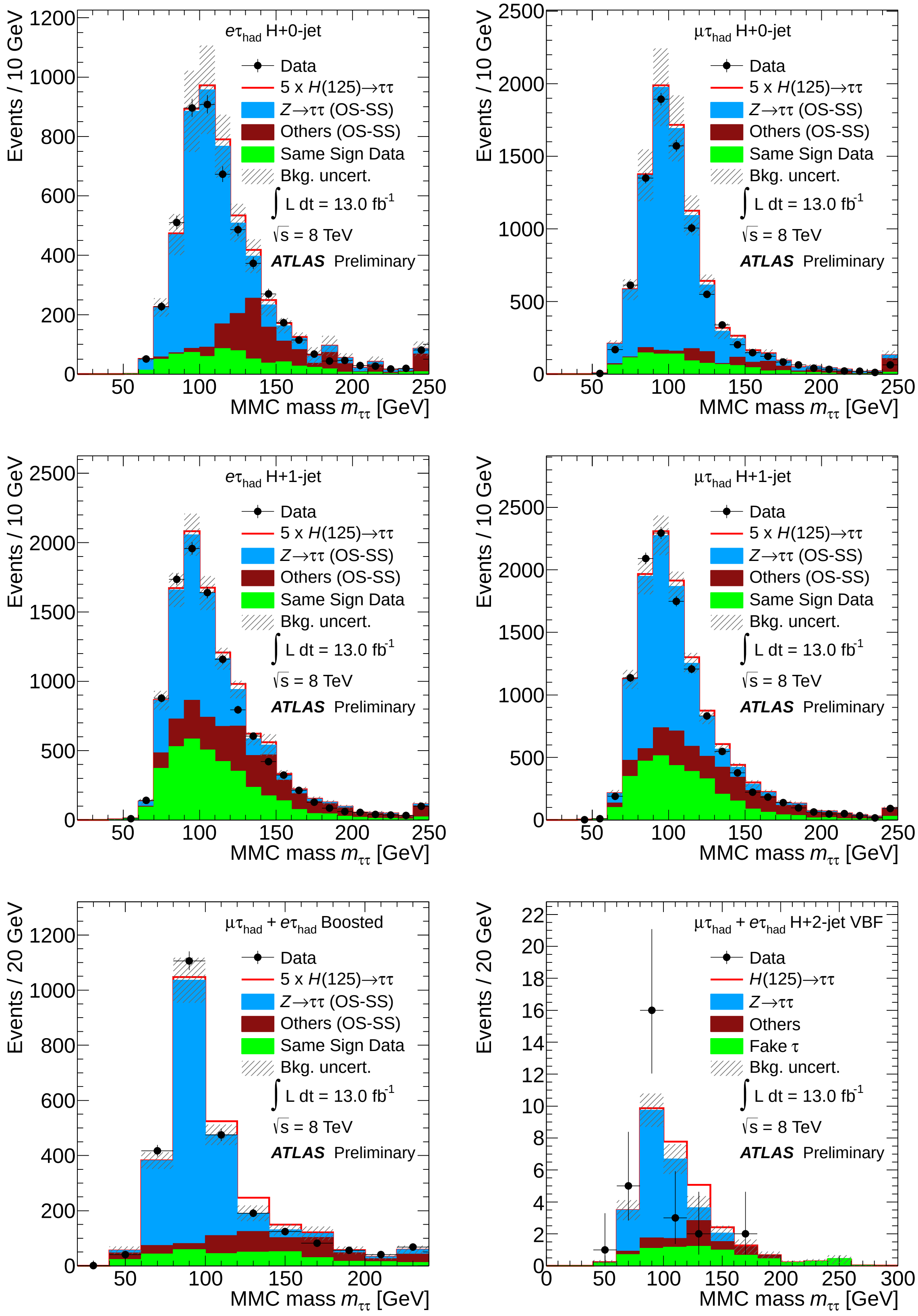

Figure 5.1: Distributions of the m_{MMC} for all categories considered in the reference $H \rightarrow \tau_l \tau_h$ analysis performed on data corresponding to an integrated luminosity or 13 fb^{-1} collected at a center-of-mass energy of $\sqrt{s} = 8$ TeV. Top left plot: 0-jet $e\tau_h$ category; Top right plot: 0-jet $\mu\tau_h$ category; Middle left plot: 1-jet $e\tau_h$ category; Middle right plot: 1-jet $\mu\tau_h$ category; Bottom left plot: Boosted category; Bottom right plot: VBF category [33].

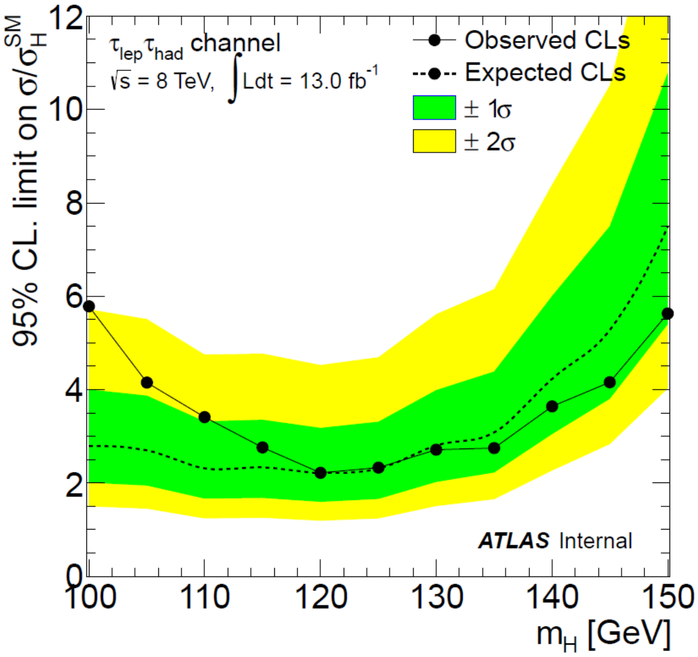

Figure 5.2: Observed (full line) and expected (dashed line) 95% CL$_s$ limits for all categories considered in the $H \longrightarrow \tau_l\tau_h$ analysis combined. The green and yellow bands represent the 1σ and 2σ bands, respectively [33].

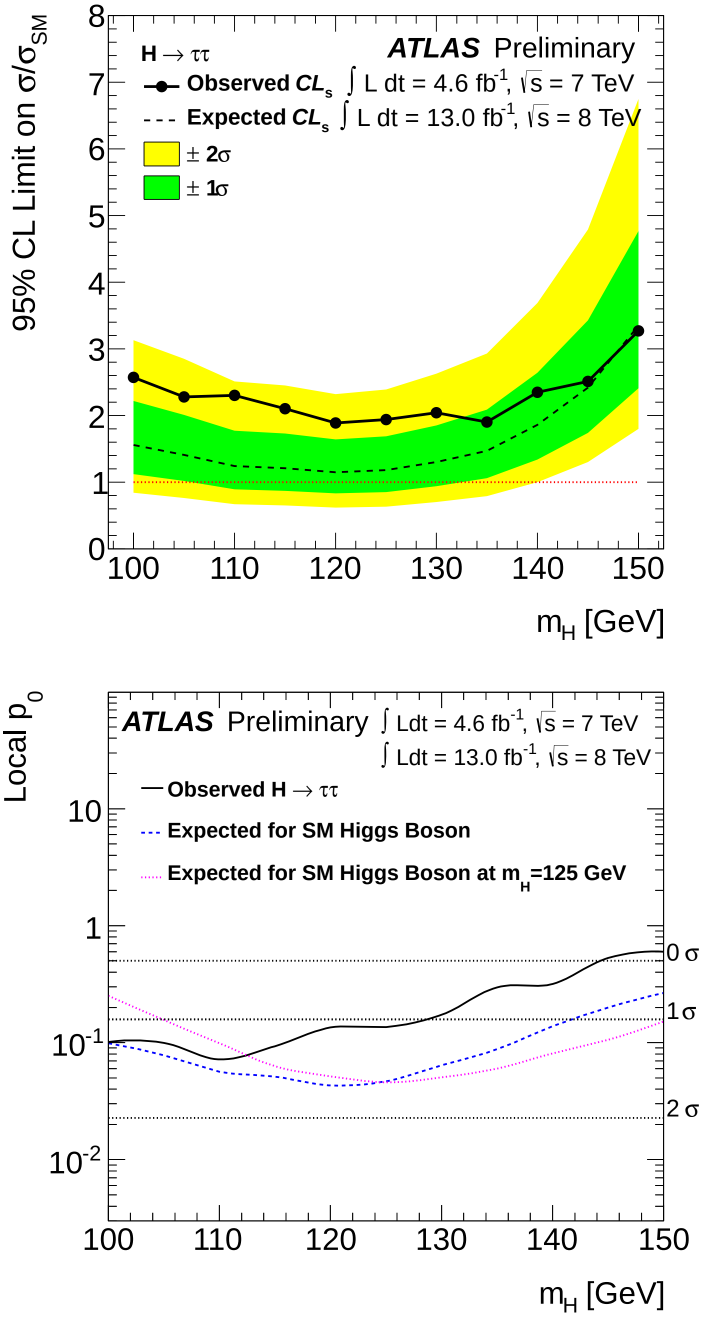

Figure 5.3: Left: Observed (solid) and expected (dashed) 95% CL_s limits for the combined $H \rightarrow \tau\tau$ channels. The expected limit is calculated under the background only hypothesis. The green and yellow bands represent the 1σ and 2σ bands, respectively. Right: Expected (dashed) and observed (solid) significance for the combined $H \rightarrow \tau\tau$ channels [20].

6 Exploitation of the τ_h substructure in the $H \rightarrow \tau_l \tau_h$ search channel

This thesis investigates the possibilities of improving the sensitivity towards a possible SM Higgs-boson signal in the 0- and 1-jet categories of the $H \rightarrow \tau_l \tau_h$ search channel (cf. Section 5.1.2) by utilizing the substructure of the τ_h. The substructure of the τ_h corresponds to the decay mode of the hadronic tau. Here, the τ_h decay modes into pions are investigated since they have the highest branching ratio (cf. Table 4.1).

Approximately 93% of all events passing the pre-selection with the requirement $E_T^{miss} > 20\,\text{GeV}$ get categorized as 0- or 1-jet events [33]. Therefore, the high event rates in these categories hold the possibility of splitting them further into subcategories. The splitting is done using the hadronic τ 1- and 3-prong signature as well as the reconstructed number of neutral pions in the decay, provided by the Pi0Finder algorithm (cf. Section 4.2).

In this chapter the approach and results of the *subcategory splitting* and its impact on the sensitivity towards a SM Higgs boson are discussed.

6.1 Subcategory splitting

The analysis categories introduced here are based on the definition of the 0- and 1-jet categories given in Section 5.1.2. These categories are split into subcategories depending on the signature of the hadronic τ decay.

6.1.1 Definition of analysis categories

The τ_h decays into one charged and any number of neutral pions in approximately 77% of all cases (cf. Table 4.1). Due to this high fraction of 1-prong τ_h decays, an additional splitting regarding the number of accompanying π^0s in the decay is done. The number of π^0s in the decay was reconstructed using the Pi0Finder algorithm, which has been introduced in Section 4.2.

Hadronic τ decays with three charged pions (3-prong decays) occur in approximately 23% of all τ_h decays. Due to this rather small branching ratio and the fact that approximately 67% of 3-prong decays do not involve any π^0s (cf. Table 4.1), no further splitting concerning π^0s is applied to 3-prong τ_h decays.

The subcategorization of the 0- and 1-jet categories relies on two quantities: the number of tracks that have been assigned to the τ_h candidate (n^{τ}_{tracks}) which corresponds to the number of charged pions in the decay, and the number of π^0s which have been found by the Pi0Finder algorithm (n_{π^0}).

Including the separate treatment of $e\tau_h$ and $\mu\tau_h$ events, this results in a total of twelve subcategories:

$$\begin{array}{ccc}
\text{0-jet } e\tau_h \text{ 1-prong-no-}\pi^0 s & \text{0-jet } e\tau_h \text{ 1-prong with-}\pi^0 s & \text{0-jet } e\tau_h \text{ 3-prong} \\
\text{0-jet } \mu\tau_h \text{ 1-prong-no-}\pi^0 s & \text{0-jet } \mu\tau_h \text{ 1-prong with-}\pi^0 s & \text{0-jet } \mu\tau_h \text{ 3-prong} \\
\text{1-jet } e\tau_h \text{ 1-prong-no-}\pi^0 s & \text{1-jet } e\tau_h \text{ 1-prong with-}\pi^0 s & \text{1-jet } e\tau_h \text{ 3-prong} \\
\text{1-jet } \mu\tau_h \text{ 1-prong-no-}\pi^0 s & \text{1-jet } \mu\tau_h \text{ 1-prong with-}\pi^0 s & \text{1-jet } \mu\tau_h \text{ 3-prong}
\end{array} \tag{6.1}$$

For the above listed subcategories, the distribution of the number of π^0s after the selection listed in Section 5.1.2 and Table 5.1, is shown in Fig. 6.1 and 6.2. All plots have been produced using the data which has been collected by the ATLAS experiment in 2012 (running periods A-E5) corresponding to an integrated luminosity of $13\,\text{fb}^{-1}$. The background has been normalized with the OS-SS background estimation method as introduced in Section 5.3.

The *1-prong-no-π^0* (*1-prong-with-π^0s*) subcategory corresponds to bin one (bin two and three) in the plots for 1-prong events (cf. left column of Fig. 6.1 (Fig. 6.2)). In total there are eight plots shown in Fig. 6.1 and 6.2, one for each of the possible combinations of the following: 0-/1-jet + $e\tau_h$/$\mu\tau_h$ + 1-/3-prong. On the y-axis the number of events as a function of the number of π^0s in the event is plotted. Bin one, two or three on the x-axis correspond to zero, one or two π^0s respectively.

6.1.2 Background composition

The major backgrounds contributing in the $H \rightarrow \tau_l \tau_h$ decay channel have been listed and described in Section 5.3. Plots showing the background composition of the different subcategories are shown in Fig. 6.1 and 6.2. The largest background component for all subcategories is the $Z \rightarrow \tau\tau$ background. Smaller contributions (in order of importance) come from QCD, $Z \rightarrow ll$ and W+jets for 0-jet subcategories or QCD, W+jets, top, $Z \rightarrow ll$ and diboson for 1-jet subcategories respectively.

It is peculiar that the $Z \rightarrow ll$ background in the 0-jet $\mu\tau_h$ channel only shows a significant contribution in the 0-jet $\mu\tau_h$ 1-prong-no-π^0 subcategory. No $Z \rightarrow ll$ contribution can be observed in the 0-jet $\mu\tau_h$ 1-prong-with-π^0 or 3-prong subcategory (cf. bottom row of Fig. 6.1). This is due to the very clean signature muons have in the detector (cf. Section 4.1.3). Muons are minimal ionizing particles and therefore leave very clean tracks and very little energy deposition in the calorimeter system. The former makes it practically impossible for muons to fake a 3-prong τ_h and the latter prevents the misidentification of π^0s. Therefore, it might be possible to gain in sensitivity by only applying the $Z \rightarrow ll$ rejection cuts to the 0-jet $\mu\tau_h$ 1-prong-no-π^0 subcategory.

The event yields for all twelve sub-categories are shown in Tables 6.1-6.4. As can be seen in these tables, the largest background contributions for all twelve subcategories come from $Z \rightarrow \tau\tau$ and same-sign-data events. It can happen that more same sign events than opposite sign events are counted, in that case the OS-SS fraction of the total event numbers is negative. Here, this is the case for the $Z \rightarrow ll$ background component in the 0-jet $\mu\tau_h$ 1-prong-with-π^0s subcategory. Since muons deposit only little amounts of energy in the calorimeter system, they are unlikely to fake 1-prong τ_h candidates which include π^0s in the decay. However, if an accompanying jet fakes the τ_h, no charge correlation is expected for $Z \rightarrow ll$+jets events

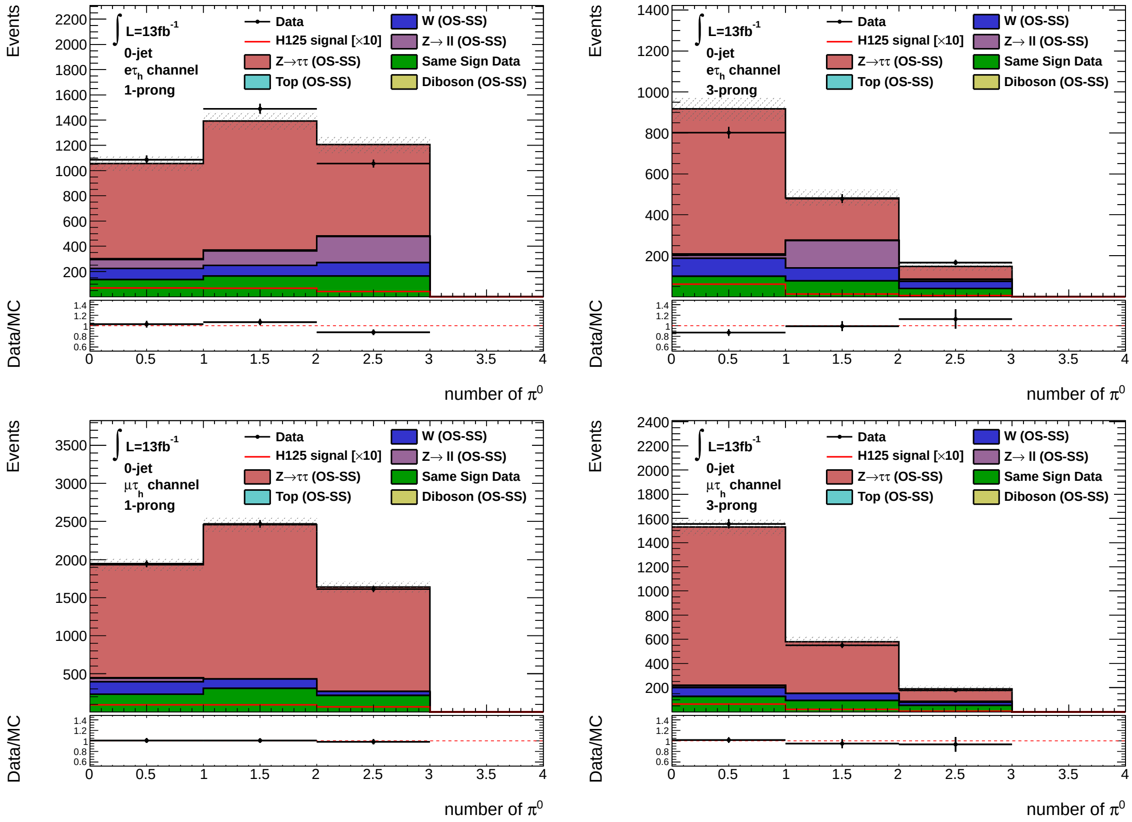

Figure 6.1: Number of π^0s for 1- and 3-prong (left/right column) events of the $e/\mu\tau_h$ (top/bottom row) subcategories of the 0-jet category. Bin1: no π^0s; bin2: 1 π^0; bin3: $2\pi^0$s.

and $n^{SS}_{Z\to ll+\text{jets}} > n^{OS}_{Z\to ll+\text{jets}}$ is possible for finite event numbers.
For 0-jet as well as 1-jet events the gluon-fusion Higgs production mode ($H_{ggF} \to \tau\tau$) is the dominant signal contribution.

6.1.3 Study on k_W-factor for subcategories

The most prominent background $Z \to \tau\tau$ is largely irreducible but well modeled by MC (cf. Section 5.3). On the other hand it is known, that the W+jets background, which is the second largest non-QCD background in the 0- and 1-jet categories (cf. Table 6.1-6.4), is not well modeled by MC. Therefore, this background is estimated in dedicated control regions (cf. Section 5.3).
To probe if the MC mismodeling depends on the τ_h substructure, i.e. if the data-to-MC agreement in the subcategories is affected by relying on the k_W factors derived for the superior 0- and 1-jet categories in Ref. [33] (listed in Table 5.2), seperate k_W factors for each subcategory have been derived and compared as described in the following.
For the subcategorization defined in the previous section, the transverse mass cut is reversed ($m_T > 70\,\text{GeV}$) to define W+jets enriched control regions (W CRs) for all subcategories. The k_W factors are derived by by scaling the W+jets MC estimate to data, from which all non-W background components have been subtracted. This is done for the subcategories using the

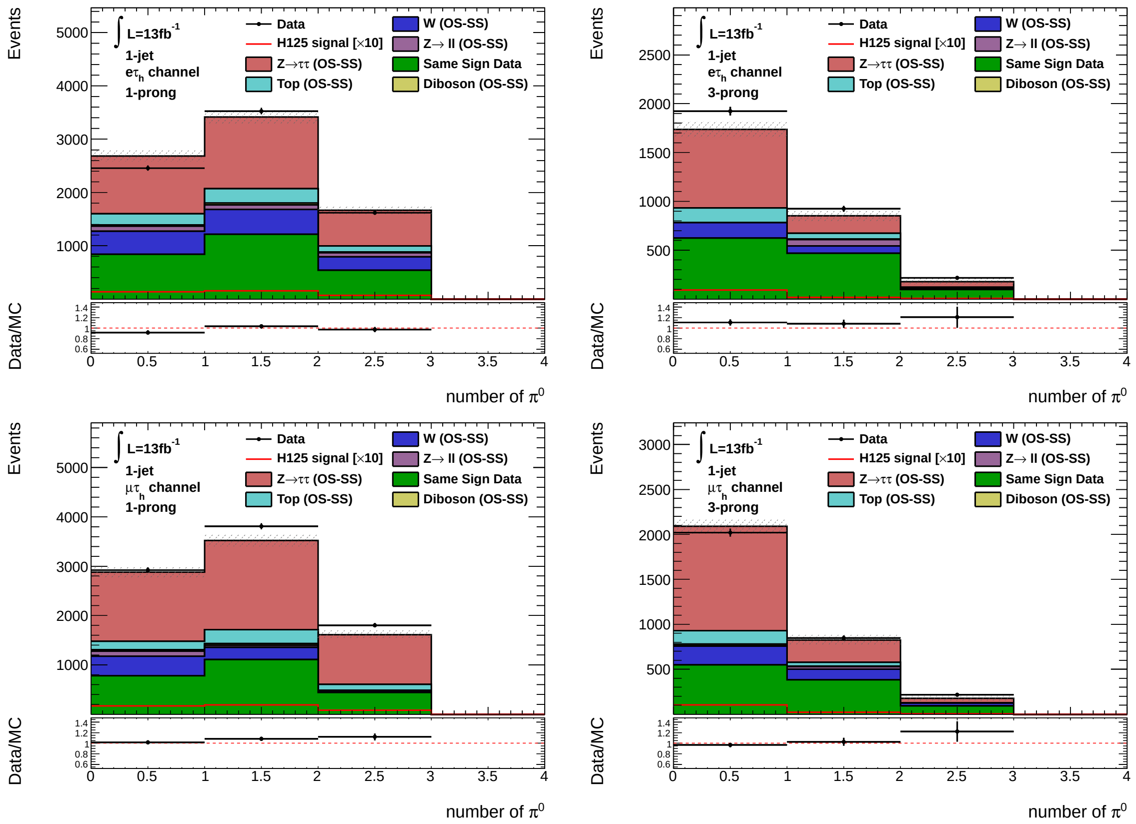

Figure 6.2: Number of π^0s for 1- and 3-prong (left/right column) events of the $e/\mu\tau_h$ (top/bottom row) subcategories of the 1-jet category. Bin1: no π^0s; bin2: 1 π^0; bin3: $2\pi^0$s.

Process	Events		
	0-jet $e\tau_h$		
	1-prong-no-π^0s	1-prong-with-π^0s	3-prong
Signal VBF125	0.04 ± 0.02	0.11 ± 0.03	0.11 ± 0.03
Signal WH125	0.04 ± 0.02	0.10 ± 0.04	0.04 ± 0.02
Signal ZH125	0.04 ± 0.02	0.03 ± 0.01	0.02 ± 0.01
Signal ggF125	6.9 ± 0.4	10.7 ± 0.5	7.9 ± 0.4
Total Signal	7.0 ± 0.4	11.0 ± 0.5	8.1 ± 0.4
$Z \to \tau\tau$ (OS-SS)	755 ± 46	1748 ± 68	979 ± 50
Diboson (OS-SS)	3.3 ± 0.7	7.5 ± 1.2	7.0 ± 1.1
$Z \to ll$ (OS-SS)	71 ± 18	305 ± 36	154 ± 22
W+jets (OS-SS)	89 ± 22	197 ± 48	188 ± 43
Top (OS-SS)	2.2 ± 0.9	3.3 ± 1.3	2.6 ± 1.0
Same sign data	136 ± 12	326 ± 18	218 ± 15
Total Background	1057 ± 56	2587 ± 93	1549 ± 71
Data	1086 ± 33	2545 ± 50	1447 ± 38

Table 6.1: Number of events in the 0-jet $e\tau_h$ categories. Only statistical uncertainties are shown.

Process	Events		
		0-jet $\mu\tau_h$	
	1-prong-no-π^0s	1-prong-with-π^0s	3-prong
Signal VBF125	0.09 ± 0.03	0.23 ± 0.05	0.13 ± 0.03
Signal WH125	0.01 ± 0.01	0.02 ± 0.02	0.06 ± 0.03
Signal ZH125	0.03 ± 0.02	0.05 ± 0.02	0.03 ± 0.01
Signal ggF125	9.0 ± 0.4	15.4 ± 0.6	8.7 ± 0.4
Total Signal	9.1± 0.4	15.7 ± 0.6	8.9 ± 0.4
$Z \to \tau\tau$ (OS-SS)	1486 ± 62	3424 ± 95	1847 ± 68
Diboson (OS-SS)	3.2 ± 0.8	9.5 ± 1.4	6.5 ± 1.1
$Z \to ll$ (OS-SS)	52 ± 14	-21.4 ± 12.6	7.8 ± 10.9
W+jets (OS-SS)	162 ± 38	175 ± 62	158 ± 44
Top (OS-SS)	1.2 ± 0.7	4.9 ± 1.2	1.7 ± 1.0
Same sign data	233 ± 16	525 ± 24	274 ± 17
Total Background	1938 ± 76	4118 ± 117	2296 ± 84
Data	1944 ± 44	4083 ± 64	2283 ± 48

Table 6.2: Number of events in the 0-jet $\mu\tau_h$ categories. Only statistical uncertainties are shown.

Process	Events		
		1-jet $e\tau_h$	
	1-prong-no-π^0s	1-prong-with-π^0s	3-prong
Signal VBF125	2.22 ± 0.142	3.48 ± 0.18	1.90 ± 0.13
Signal WH125	0.652 ± 0.092	1.03 ± 0.12	0.50 ± 0.08
Signal ZH125	0.382 ± 0.06	0.54 ± 0.06	0.32 ± 0.05
Signal ggF125	10.12 ± 0.5	17.4 ± 0.6	9.1 ± 0.4
Total Signal	13.4 ± 0.5	22.5 ± 0.7	11.8 ± 0.5
$Z \to \tau\tau$ (OS-SS)	1083 ± 58	2012 ± 79	1044 ± 56
Diboson (OS-SS)	28.1 ± 2.7	47.2 ± 3.5	27.5 ± 2.9
$Z \to ll$ (OS-SS)	84 ± 577	173 ± 46	43 ± 26
W+jets (OS-SS)	387 ± 44	642 ± 82	227 ± 55
Top (OS-SS)	207 ± 9	386 ± 13	229 ± 13
Same sign data	840 ± 29	1756 ± 42	1191 ± 35
Total Background	2630 ± 98	5017 ± 131	2761 ± 90
Data	2457 ± 50	5147 ± 72	3064 ± 55

Table 6.3: Number of events in the 1-jet $e\tau_h$ categories. Only statistical uncertainties are shown.

Process	Events		
	0-jet $\mu\tau_h$		
	1-prong-no-π^0s	1-prong-with-π^0s	3-prong
Signal VBF125	2.39 ± 0.15	4.00 ± 0.19	1.91 ± 0.13
Signal WH125	0.73 ± 0.10	1.04 ± 0.12	0.62 ± 0.09
Signal ZH125	0.49 ± 0.06	0.57 ± 0.06	0.25 ± 0.04
Signal ggF125	13.2 ± 0.5	21.5 ± 0.7	10.4 ± 0.5
Total Signal	16.8 ± 0.6	27.1 ± 0.7	13.2 ± 0.5
$Z \to \tau\tau$ (OS-SS)	1401 ± 67	2815 ± 92	1459 ± 66
Diboson (OS-SS)	30.7 ± 2.7	51.8 ± 3.9	29.8 ± 3.0
$Z \to ll$ (OS-SS)	111 ± 23	33 ± 15	12 ± 15
W+jets (OS-SS)	439 ± 57	370 ± 90	415 ± 58
Top (OS-SS)	170 ± 9	402 ± 14	204 ± 12
Same sign data	779 ± 29	1547 ± 41	1022 ± 34
Total Background	2931 ± 96	5219 ± 137	3142 ± 96
Data	2923 ± 54	5614 ± 75	3081 ± 56

Table 6.4: Number of events in the 1-jet $\mu\tau_h$ categories. Only statistical uncertainties are shown.

equation 5.5 which is again listed here for greater clarity:

$$k_W = \frac{n^{\text{data}} - n^{MC}_{\text{non-W}}}{n^{MC}_{W}}.$$

Where $n^{MC}_{\text{non-W}}$ corresponds to the non-W background events estimated by MC:

$$n^{MC}_{\text{non-W}} = n^{MC}_{Z\to\tau\tau} + n^{MC}_{Z\to ll} + n^{MC}_{diboson} + n^{MC}_{top}. \tag{6.2}$$

The statistical uncertainties of the MC estimates and data events have been propagated to k_W. Since the τ_h misidentification rate is different for quark and gluon initiated jets and the OS requirement leads to different quark-gluon fractions in OS and SS events, the k_W factors are derived separately for OS and SS events.

The visible mass distributions in the W CR for the 0-jet $\mu\tau_h$ categories after applying the corresponding k_W factor are shown in Fig. 6.3 (nominal categorization as used by the reference analysis) and 6.4 (subcategories as defined in the previous section). The corresponding plots for all other categories are shown in Fig. A.1-A.3 and Fig. A.4-A.6, respectively.

Due to a charge asymmetry for W+jets events (cf. Section 5.3) the event rates are higher for OS events. The W+jets MC sample corresponds to an integrated luminosity of 5 fb^{-1}. It is scaled up to be comparable to the 13 fb^{-1} data set. This leads to spiky visible mass distributions and large errors on the MC background estimate for SS event in all subcategories.

The derived subcategory k_W factors are listed in Table 6.5 together with the k_W factors taken from Ref. [33] (k_W^{ref}). In Figure **??** the variation of the k_W factors depending on the subcategory for 0- and 1-jet events are displayed seperately for the $e\tau_h/\mu\tau_h$ channel and for OS and SS events. The k_W factors derived in the reference analysis (k_W^{ref}) and their uncertainties are represented by the green line and band in Fig. 6.5 and 6.6. Whereas the subcategory

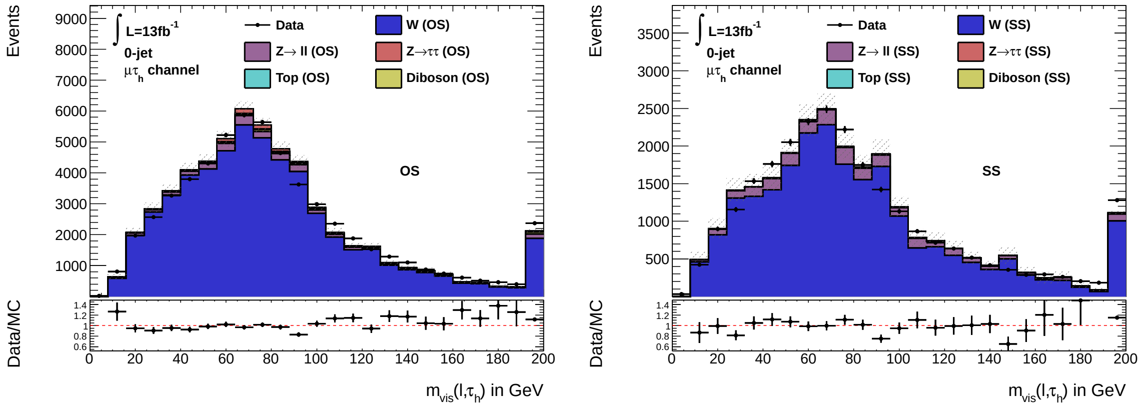

Figure 6.3: Distributions of the m_{vis} in the W control regions for the 0-jet $\mu\tau_h$ category. Left plot: opposite sign (OS) W CR; Right plot: same sign (SS) W CR.

			k_W^{ref}	subcategories $k_W^{\text{1p-no-}\pi^0}$	 $k_W^{\text{1p-with-}\pi^0\text{s}}$	 k_W^{3p}
0-jet	$e\tau_h$	OS	0.614 ± 0.010	0.613 ± 0.018	0.648 ± 0.015	0.597 ± 0.017
		SS	0.739 ± 0.010	0.808 ± 0.057	0.680 ± 0.033	0.780 ± 0.041
	$\mu\tau_h$	OS	0.581 ± 0.009	0.550 ± 0.015	0.634 ± 0.014	0.553 ± 0.014
		SS	0.717 ± 0.024	0.729 ± 0.047	0.757 ± 0.032	0.720 ± 0.033
1-jet	$e\tau_h$	OS	0.656 ± 0.014	0.674 ± 0.023	0.717 ± 0.021	0.626 ± 0.020
		SS	0.859 ± 0.014	0.889 ± 0.064	0.886 ± 0.037	0.797 ± 0.039
	$\mu\tau_h$	OS	0.557 ± 0.011	0.501 ± 0.017	0.639 ± 0.017	0.561 ± 0.015
		SS	0.710 ± 0.024	0.755 ± 0.045	0.747 ± 0.032	0.643 ± 0.036

Table 6.5: k_W factors for the 0-/1-jet $e\tau_h/\mu\tau_h$ 1-prong-no-π^0/1-prong-with-π^0s/3-prong subcategories (right three columns). The k_W factors derived for the 0-/1-jet $e\tau_h/\mu\tau_h$ categories in Ref. [33] are listed in the column "k_W^{ref}". The uncertainties represent statistical uncertainties only.

depending k_W factors and statistical uncertainties are shown by the black curve. Due to the charge asymmetry in W+jets events (cf. Section 5.3), the statistical uncertainties are smaller for OS events (cf. Fig. 6.5 and 6.6 left/right column).

It is peculiar, that for OS events the k_W factor of the 1-prong-with-π^0s subcategory is always higher than any other k_W factor derived for the same superior category (cf. Fig. 6.5 and 6.6 left column, last bin). This indicates that the systematic uncertainties depend on the τ_h substructure.

As can be seen in Table 6.5 and figures 6.5 and 6.6 the k_W factors for the subcategories differ from those derived in Ref. [33]. In order to know if these differences result in significant changes in the data-to-MC agreement for the subcategories, both k_W factors are applied to each subcategory. As variable the visible mass of the lepton-τ_h system is chosen. The visible mass of the lepton-τ_h system is calculated using the definition:

$$m_{vis}(l,\tau_h) = \sqrt{2 \cdot p_T^l \cdot p_T^{\tau_h} \cdot \cosh\left(|\eta_l - \eta_{\tau_h}| + 1\right)}. \tag{6.3}$$

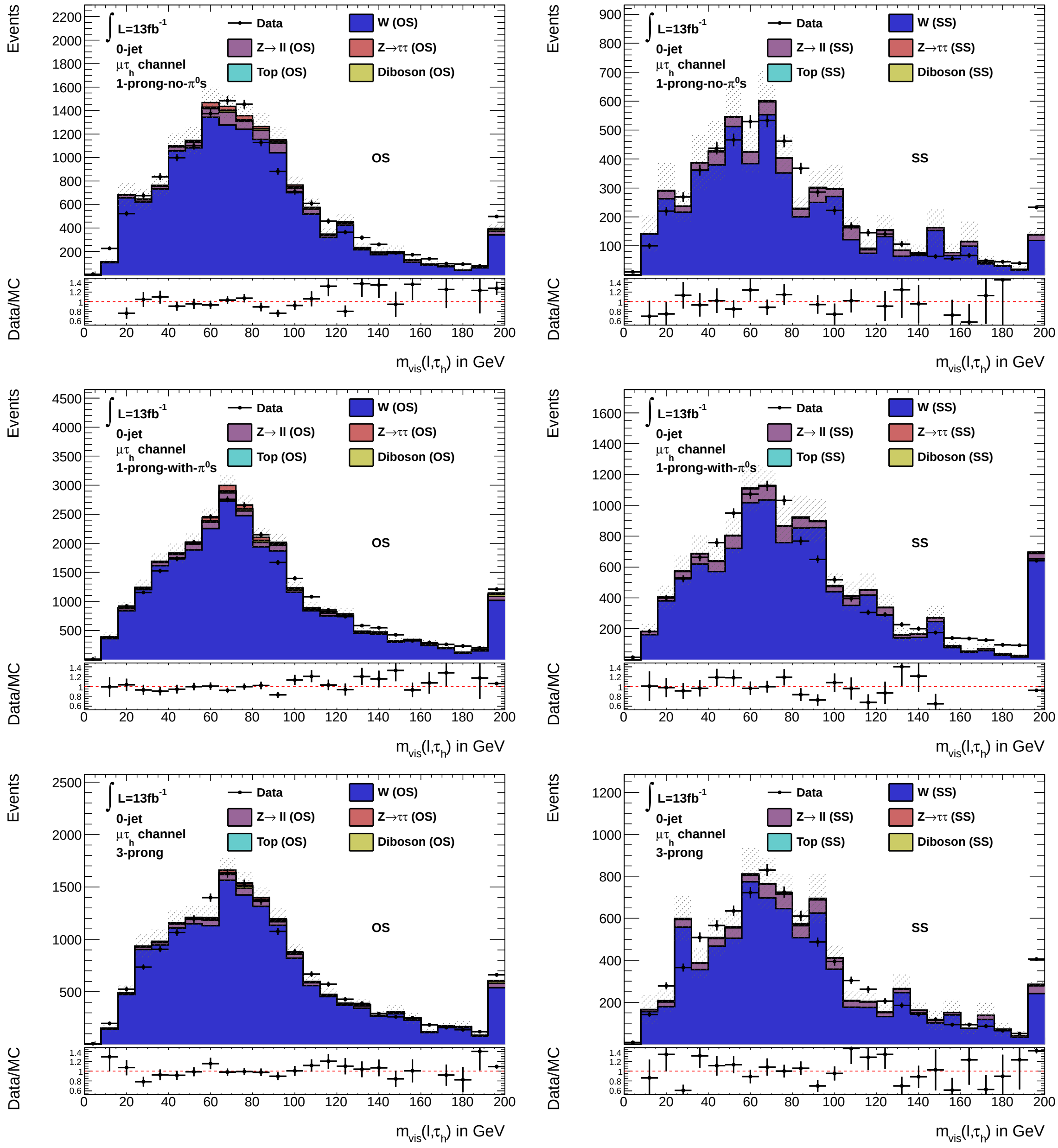

Figure 6.4: Distributions of the m_{vis} in the W control regions for all 0-jet $\mu\tau_h$ subcategories. Left column: opposite sign (OS) W CR; Right column: same sign (SS) W CR. Top row: 0-jet $\mu\tau_h$ 1-prong-no-π^0 subcategory; Middle row: 0-jet $\mu\tau_h$ 1-prong-with-π^0s subcategory; Bottom row:0-jet $\mu\tau_h$ 3-prong subcategory.

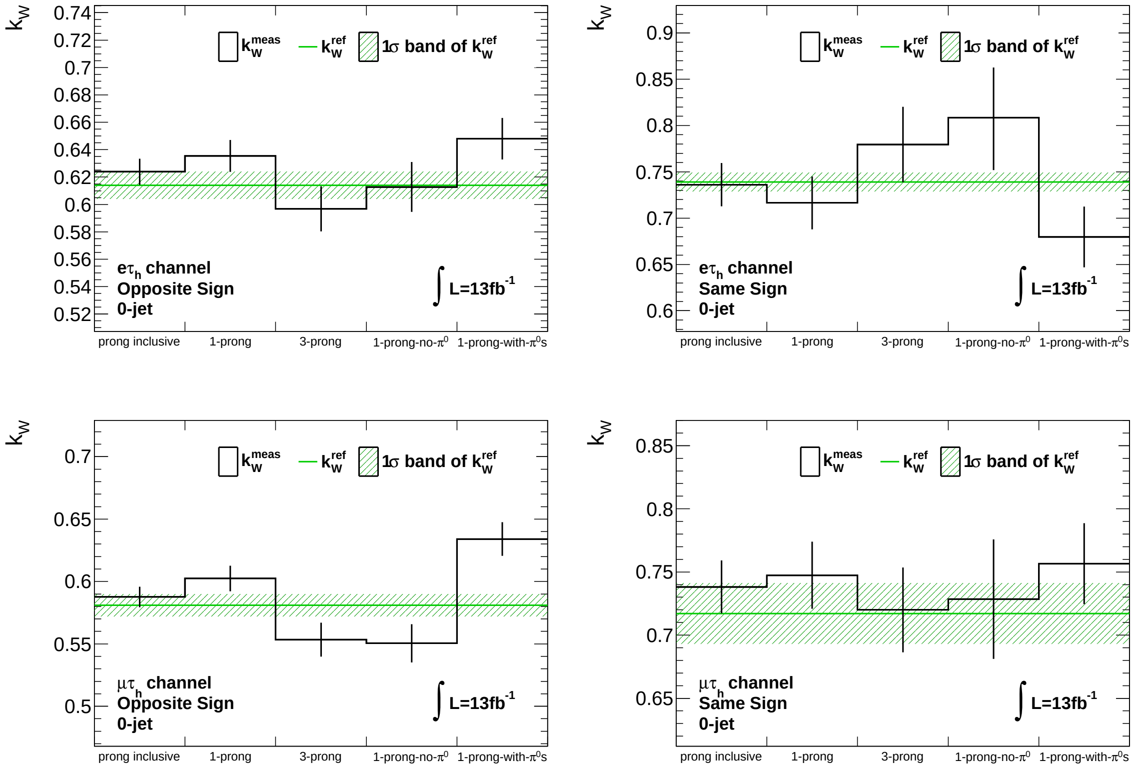

Figure 6.5: Variation of the k_W factors for the various subcategories for 0-jet events (black curve). The individual subcategories are indicated by the x-axis labels. The k_W factors and their uncertainties as listed in Table 5.2 (Ref. [33]) are indicated by the green line and band. Shown are statistical uncertainties only. Left column: OS events; Right column: SS events. Top row: $e\tau_h$ channel; Bottom row: $\mu\tau_h$ channel.

Where η_l and η_{τ_h} correspond to the pseudorapidity of the lepton and the τ_h, respectively. The corresponding distributions, once derived with the k_W factor of the superior 0-/1-jet categories (k_W^{ref}) and once derived with the subcategory dependent k_W factors, are compared for each subcategory. The resulting visible mass distributions for the three 0-jet $\mu\tau_h$ subcategories are shown in Fig. 6.7. The corresponding plots to the 0-/1-jet $e\tau_h$ and 1-jet $\mu\tau_h$ subcategories can be found in appendix A.

As can be seen in Fig. 6.7 the differences between the k_W factors only lead to minor changes in the data-to-MC agreement between the m_{vis} distributions derived with the k_W factors taken from Ref. [33] and the subcategory dependent k_W factors (left and right column of Fig. 6.7, respectively). For convenience, the k_W factors from Ref. [33] are used for the following studies.

6.2 Study on $p_T(\tau_h)$

Neutral pions are short-lived particles that decay after approximately 10^{-16} s into two photons and deposit their energy in the electromagnetic calorimeter. In the current approach the τ_h momentum is reconstructed using the tracks in the inner detector. The reconstruction is

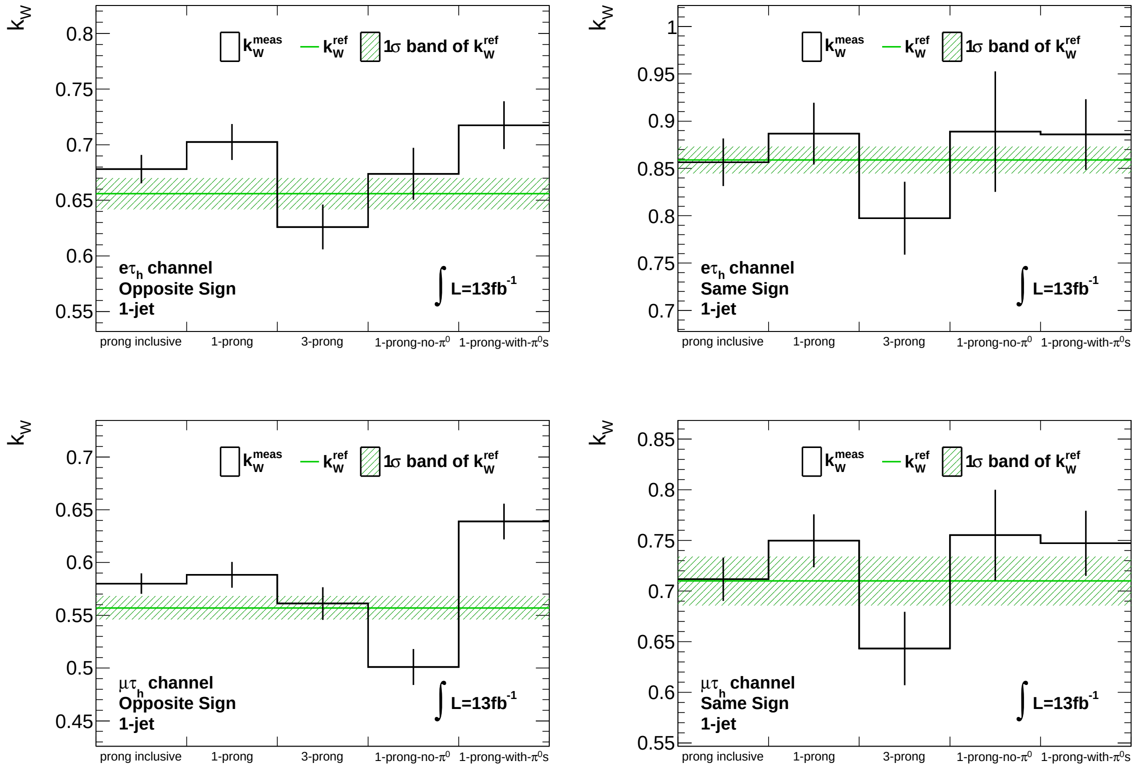

Figure 6.6: Variation of the k_W factors for the various subcategories for 1-jet events (black curve). The individual subcategories are indicated by the x-axis labels. The k_W factors and their uncertainties as listed in Table 5.2 (Ref. [33]) are indicated by the green line and band. Shown are statistical uncertainties only. Left column: OS events; Right column: SS events. Top row: $e\tau_h$ channel; Bottom row: $\mu\tau_h$ channel.

therefore only sensitive to the charged fraction of the τ_h. By reconstructing the momentum of the τ_h with the tracks from the inner detector, which correspond to the $\pi^{\pm}$, and the π^0 energy clusters in the EMcal as done by the Pi0Finder algorithm (cf. Ref. [29] and Section 4.2), one can benefit from the better energy resolution of the EMcal. Therefore, using information about the π^0s in an event allows to improve the reconstruction of kinematic variables like the visible mass of the lepton-τ_h system.

This Section compares the pion-based transverse momentum (derived with the Pi0Finder algorithm) and visible mass to their regularly derived equivalents (reconstructed as described in Section 4.1.6).

6.2.1 Comparison of $m_{vis}(l,\tau_h)$ and $m_{vis}^{\pi^0\text{ reco}}(l,\tau_h)$

To probe if the π^0 based transverse momentum of the τ_h ($p_T^{\pi^0\text{ reco}}(\tau_h)$) improves the mass resolution and the sensitivity towards a possible SM Higgs-boson signal, the visible mass of the lepton-τ_h system is calculated using $p_T^{\pi^0\text{ reco}}(\tau_h)$ (cf. equation 6.3). This with $p_T^{\pi^0\text{ reco}}(\tau_h)$ calculated visible mass ($m_{vis}^{\pi^0\text{ reco}}(l,\tau_h)$) is then compared to the visible mass ($m_{vis}(l,\tau_h)$) which has been calculated using the regular $p_T(\tau_h)$. The $m_{vis}^{\pi^0\text{ reco}}(l,\tau_h)$ visible mass distributions

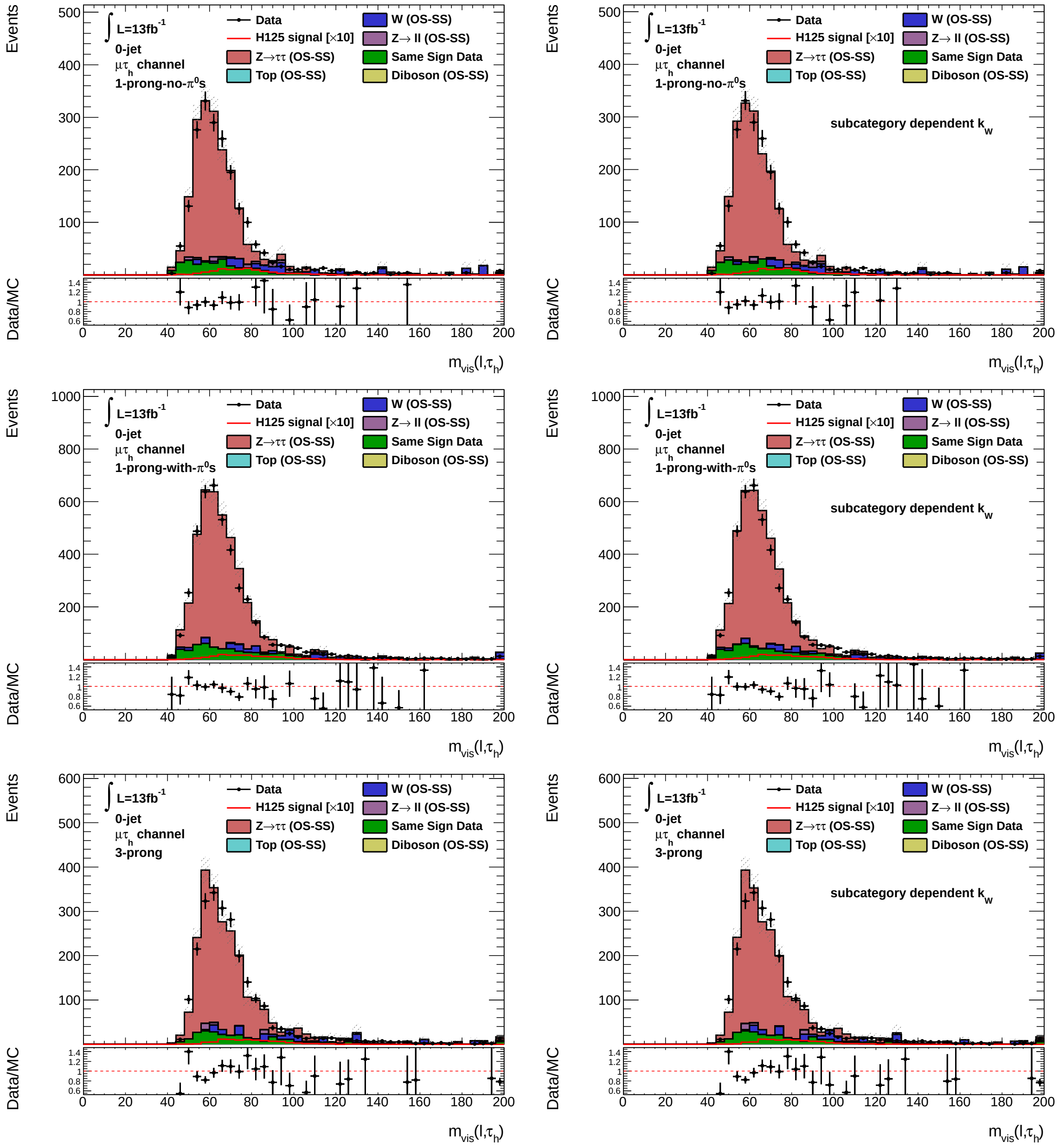

Figure 6.7: Visible mass distributions of the lepton-τ_h system for the 0-jet $\mu\tau_h$ subcategories for different k_W factors. The m_{vis} distributions derived with the k_W factors taken from Ref. [33] are shown in the left column. In the right column the m_{vis} distributions derived with the subcategory dependent k_W factors are shown.

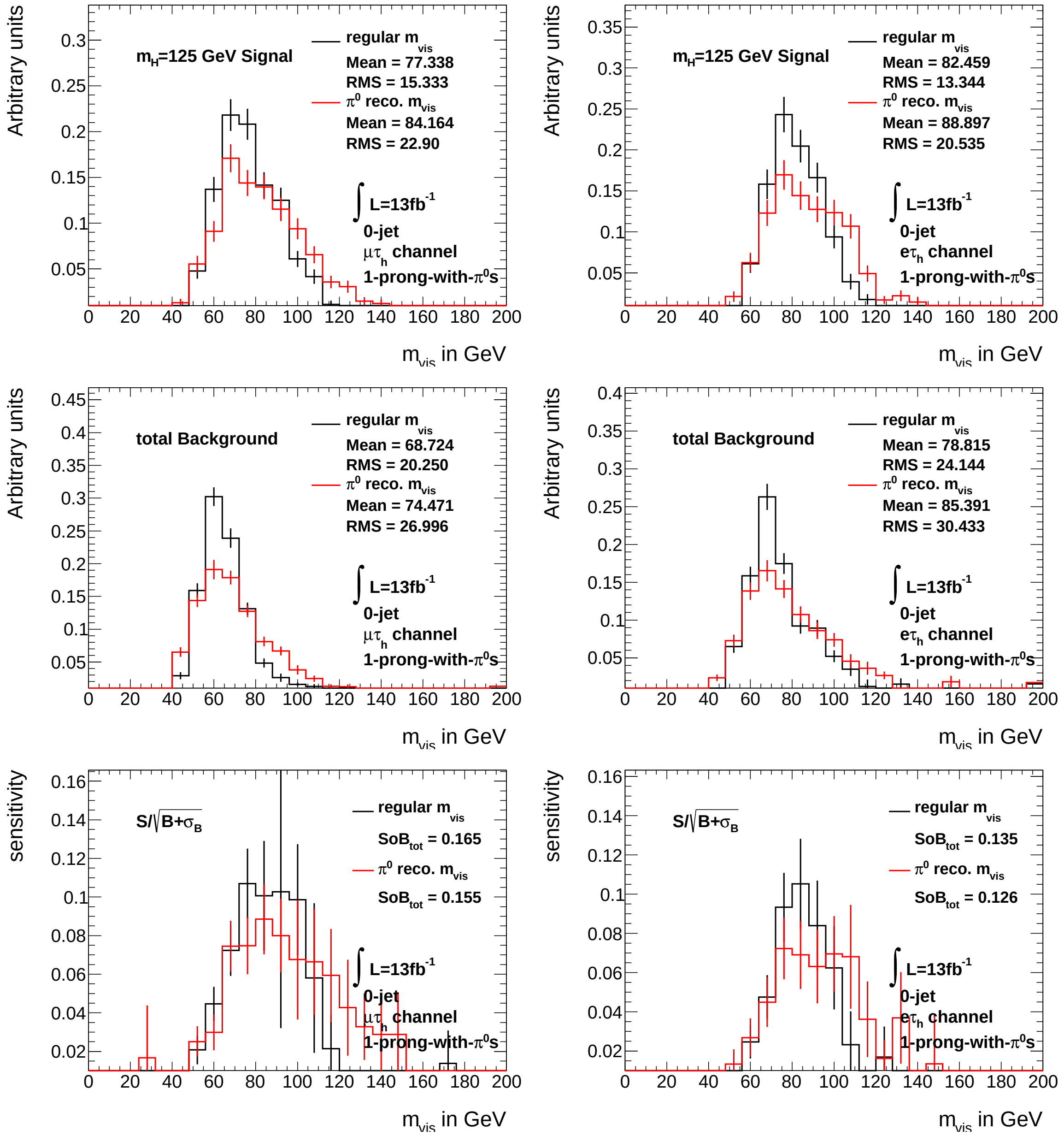

Figure 6.8: Comparison of regular (black curve) and with π^0 information reconstructed visible mass (red curve) distributions of the $m_H = 125\,\text{GeV}$ Higgs-boson signal (top row) and the total background (middle row). The corresponding expected sensitivity distributions are shown in the bottom row. All histograms are for the 0-jet 1-prong-with-π^0s category for the $\mu\tau_h$ channel (left column) and the $e\tau_h$ channel (right column).

for all twelve subcategories are shown in Fig. B.1 and Fig. B.2, respectively.

Figure 6.8 shows a comparison for the background and signal shapes of the two visible mass distributions for the 0-jet 1-prong-with-π^0s category. Background as well as signal distributions have been normalized to unity. The corresponding distributions for all other subcategories can be found in appendix B.

The two visible mass distributions peak at approximately the same mass for signal as well as background events (cf. Fig. 6.8 top and middle row, respectively). However, the $m_{vis}^{\pi^0\text{ reco}}$

distribution has a larger tail into the high mass region, which leads to larger RMS and mean values. This larger tail results from the Pi0Finder algorithm reconstruction principle. As described in Section 4.2 the Pi0Finder algorithm has two different features. On the one hand it provides information about the number of π^0s in the τ_h decay through a dedicated π^0-counting algorithm. On the other hand, it reconstructs the τ_h four-momentum by combining the four-momentum of the track system associated to the τ_h and the four-momentum of the reconstructed calorimeter clusters with the highest π^0-likeness score. However, those two features are decoupled from each other. One or two cluster(s) are always chosen to reconstruct the $p_T^{\tau_h}$, irrelevant of the number of π^0s that has been found by the π^0-counting algorithm.

This leads to a shift of the $p_T^{\tau_h}$ to higher values if in truth there were no π^0s in the decay, and finally to a larger tail in the high mass region.

To probe which visible mass variable is more sensitive towards a SM Higge-boson signal, the expected sensitivity has been calculated using the common simplification (cf. Ref. [36]):

$$\mathrm{SoB} = \frac{S}{\sqrt{B + \sigma_B^2}}. \tag{6.4}$$

In this notation, S and B refer to the expected number of signal and background events, respectively. The uncertainty of the unweighted background is represented by σ_B. Whereas $\sqrt{B}$ accounts for the finite number of collected data events. For an infinite number of generated MC events σ_B would tend to zero. The systematic uncertainty on the MC background estimation is neglected. The uncertainties of S and B have been propagated to the expected sensitivity.

To obtain the expected sensitivity as a function of the visible mass, the term 6.4 has been calculated for each bin of the corresponding signal and background histograms. The resulting histograms are shown in Fig. 6.8, bottom row.

To obtain a measure for the overall discrimination power of the two visible mass distibutions, the expected sensitivity over the entire mass range has been calculated using:

$$\mathrm{SoB}_{tot} = \sqrt{\sum_{i=1}^{\mathrm{bins}} \mathrm{SoB}_i^2}. \tag{6.5}$$

All bins of the m_{vis} distributions are treated as uncorrelated. The values of SoB_{tot} for the different subcategories are shown in Table 6.6. The background discrimination is approximately equal for both visible mass variables. The only exception is the 0-jet $\mu\tau_h$ 1-prong-no-π^0s subcategory, which has a large high mass tail that explains this behavior.

Overall no improvement of the expected sensitivity could be observed for the $m_{vis}^{\pi^0\,\mathrm{reco}}$ variable. Therefore, no improvement of the sensitivity is expected if the $p_T^{\tau_h}$ reconstructed with the Pi0Finder algorithm is used for the missing mass calculator (MMC).

6.2.2 Sensitivity scan for optimal $p_T^{\tau_h}$ cut value

A scan over possible cut values for $p_T^{\tau_h}$ has been performed to investigate if another cut value than $p_T^{\tau_h} > 20\,\mathrm{GeV}$, as used in the reference analysis (cf. Ref. [33]), can increase the expected

			SoB$_{tot}$	
			regular	with π^0 information
subcategories	0-jet	$\mu\tau_h$	1-prong-no-π^0	0.160±0.050	0.300±0.241
			1-prong-with-π^0	0.168±0.027	0.155±0.015
			3-prong	0.126±0.019	0.134±0.029
		$e\tau_h$	1-prong-no-π^0	0.145±0.028	0.160±0.031
			1-prong-with-π^0	0.138±0.015	0.126±0.015
			3-prong	0.123±0.016	0.119±0.015
	1-jet	$\mu\tau_h$	1-prong-no-π^0	0.172±0.016	0.172±0.036
			1-prong-with-π^0	0.200±0.015	0.188±0.022
			3-prong	0.129±0.014	0.127±0.012
		$e\tau_h$	1-prong-no-π^0	0.147±0.015	0.140±0.133
			1-prong-with-π^0	0.164±0.013	0.155±0.012
			3-prong	0.118±0.013	0.113±0.012

Table 6.6: Expected sensitivity for all subcategories with the visible mass of the lepton-τ_h system as discriminating variable. Right column: expected sensitivity corresponding to $m_{vis}^{\pi^0\ \text{reco}}$, second to right column: expected sensitivity corresponding to m_{vis}^{regular}.

sensitivity. The scan was done for all subcategories on $p^{\tau}_{T,\,\text{regular}}$ as well as $p^{\tau_h}_{T,\,\pi^0\ \text{reco}}$ in the range from 20 GeV to 50 GeV in 4 GeV steps.

The expected sensitivity is calculated using equation 6.4 where the number of signal and background events are derived by applying a cut on $p_T^{\tau_h}$ and calculating the integral over the entire mass range. The uncertainty on the unweighted background estimate corresponds to σ_B. The resulting expected sensitivity curves are shown in Fig. 6.9. The labels on the x-axis correspond to the cut applied. For example: the value "30 GeV" on the x-axis means, the cut $p_T^{\tau_h} > 30\,\text{GeV}$ was applied on top of the usual selection. In appendix C the sensitivity scans for all subcategories are shown. All 0-jet and 1-jet based subcategories, respectively, have a very similar structure: For 0-jet events the expected sensitivity rises with $p_T^{\tau_h}$ whereas it falls after a local maximum around $p_T^{\tau_h} > 25\,\text{GeV}$ for 1-jet events. Although small differences between $p^{\tau_h}_{T,\,\text{regular}}$ and $p^{\tau}_{T\ \pi^0\ \text{reco}}$ can be observed, their error bars always overlap.

Although the $p^{\tau_h}_{T,\,\pi^0\ \text{reco}}$ has been validated (cf. Ref. [30]) and the data-to-MC agreement seems good, this variable has not been calibrated yet. Therefore, and since no big differences between $p^{\tau_h}_{T,\,\text{regular}}$ and $p^{\tau_h}_{T,\,\pi^0\ \text{reco}}$ can be observed, $p^{\tau_h}_{T,\,\text{regular}}$ is chosen as cut variable for the limit calculation.

6.3 Exclusion limits

In this Section, 95% CL$_s$ upper exclusion limits on the Higgs-boson cross section as a function of the Higgs-boson mass are derived with the method described in Ref. [15]. As discriminating variable the MMC mass (m_{MMC}) of the di-tau system is chosen. The m_{MMC} distributions for all subcategories as used in the limit calulation are shown in Fig. 6.14-6.17. All systematic uncertainties mentioned in Section 5.4 have been used in the limit calculation.

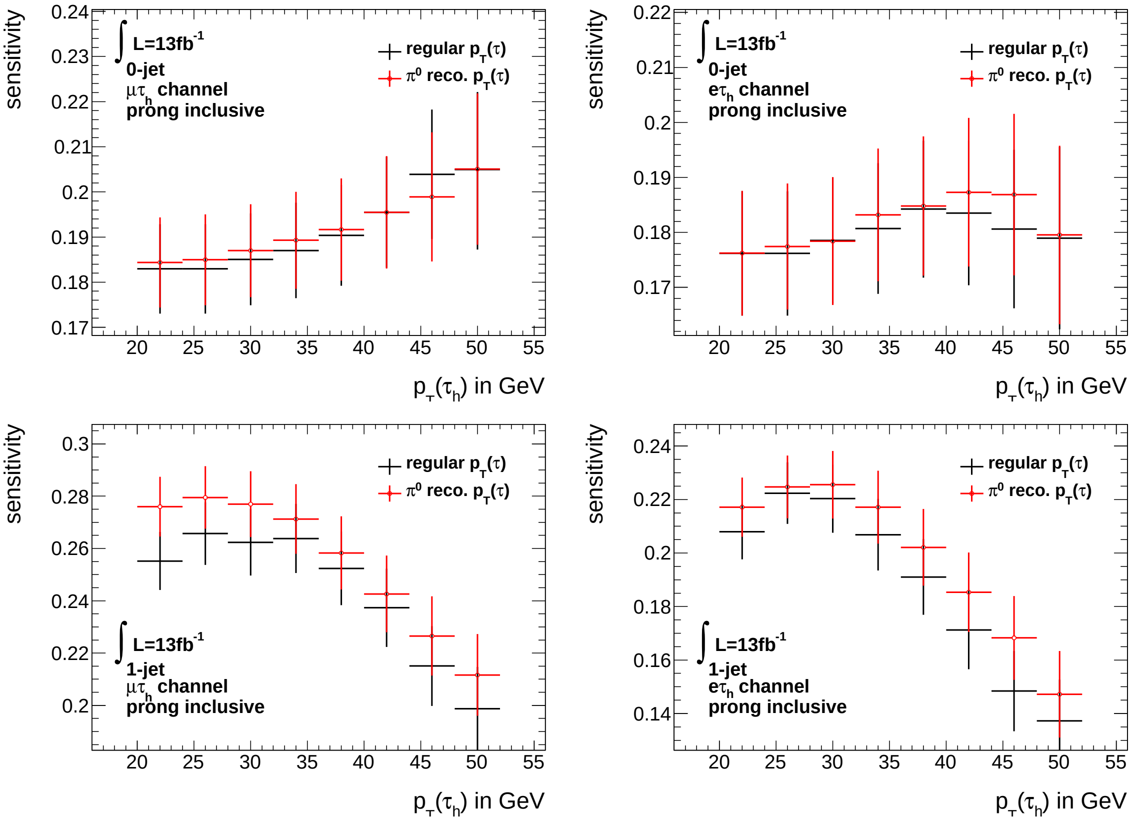

Figure 6.9: Expected sensitivity scan for different cut values on $p_T^{\tau_h}$ (black) and $p_{T,\,\pi^0\ \mathrm{reco}}^{\tau_h}$ (red) for the 0-jet (top row) and 1-jet category (bottom row). The x-axis labels correspond to the cut on $p_T^{\tau_h}$ that was applied on top of the selection.

It should be noted that no systematic uncertainties have been derived for any π^0 related variables from the Pi0Finder algorithm. This is an open working point in the τ_h working group. As a first qualitative estimate, the expected sensitivity towards a SM Higgs-boson signal is calculated for each subcategory using the common simplification

$$\text{expected sensitivity}(\text{subcat.}) = \sqrt{\sum_{\text{bin } i} \left(\frac{n^i_{Sig}}{\sqrt{n^i_{Bkg}}} \right)^2}. \tag{6.6}$$

Where n^i_{Sig} and n^i_{Bkg} denote to the number of signal and background events in bin i of the m_{MMC} distribution estimated by MC. The expected sensitivity for the combination of the 0- and 1-jet subcategories, respectively, is then calculated using

$$\text{expected sensitivity}(\text{combi.}) = \sqrt{\sum_{\text{subcat. } j} (\text{expected sensitivity}(\text{subcat. } j))^2}, \tag{6.7}$$

where j denotes the individual subcategories. This is done for the combination of the six 0-jet (1-jet) subcategories. As a reference, the expected sensitivity for the combination of the $e\tau_h$ and $\mu\tau_h$ channels of the nominal 0-jet (1-jet) categorization is calculated. The results

	expected sensitivity for 0-jet based subcategories			
	nominal	1-prong-no-π^0s	1-prong-with-π^0s	3-prong
$e\tau_h$	0.46	0.32	0.28	0.28
$\mu\tau_h$	0.59	0.59	0.44	0.29
combination	0.75	0.94		

Table 6.7: Estimate of the expected sensitivity towards a SM Higgs-boson signal for 0-jet based subcategories.

	expected sensitivity for 1-jet based subcategories			
	nominal	1-prong-no-π^0s	1-prong-with-π^0s	3-prong
$e\tau_h$	0.59	0.33	0.41	0.28
$\mu\tau_h$	0.68	0.41	0.48	0.31
combination	0.90	0.92		

Table 6.8: Estimate of the expected sensitivity towards a SM Higgs-boson signal for 1-jet based subcategories.

are listed in Table 6.7 (6.8).

As can be seen in Tables 6.7 and 6.8 the combinations of the six 0- or 1-jet subcategories show higher expected sensitivities towards a SM Higgs-boson signal than the nominal categorization. In order to understand this improvement, the signal and background components in each subcategory have to be analyzed.

The fraction of events that appears in each subcategory is listed in Tables 6.9-6.12 for all processes. The event numbers which were used to calculate these percentages are listed in Tables 6.1-6.4. Negative percentages or percentages greater than 100% are possible for the estimated background processes, since the used event numbers correspond to the OS-SS fraction of the total event numbers. It can happen that more same sign events than opposite sign events are counted, in that case the OS-SS fraction of the total event numbers is negative. Here, this is the case for the $Z \to ll$ background component in the 0-jet $\mu\tau_h$ 1-prong-with-π^0s subcategory. Since muons deposit only little amounts of energy in the calorimeter system, they are unlikely to fake 1-prong τ_h candidates which include π^0s in the decay. However, if an accompanying jet fakes the τ_h, no charge correlation is expected for $Z \to ll$+jets events and $n^{SS}_{Z\to ll+\text{jets}} > n^{OS}_{Z\to ll+\text{jets}}$ is possible for limited event numbers.

As can be seen in Tables 6.9-6.12, the fraction of total signal events is higher than the fraction of total background events in all 1-prong-no-π^0s categories. For example, the fraction of total signal events in the 0-jet $e\tau_h$ 1-prong-no-π^0s subcategory is 26.9% whereas the fraction of total background events in this subcategory is only 20.4%. The reduction of the total background in this subcategory is mainly driven by the reduction of the $Z \to \tau\tau$ and same-sign-data background components, which are the two largest background components for 0- and 1-jet based subcategories as can be seen in Tables 6.1 and 6.2.

The same-sign-data background component consists in large parts of QCD jets. A 1-prong τ_h without π^0s in the decay is a very narrow jet with only one track. A QCD jet is unlikely to fake this signature and the fraction of same-sign-data events in the 1-prong-no-π^0s subcategory is reduced. Due to the higher jet multiplicity and relatively larger same-sign-data

Process	Fraction of Events in 0-jet $e\tau_h$ in %		
	1-prong-no-π^0s	1-prong-with-π^0s	3-prong
Signal VBF125	15.5	42.0	42.5
Signal WH125	20.0	57.0	23.0
Signal ZH125	48.3	32.4	19.3
Signal ggF125	27.0	42.1	31.0
Total Signal	26.9	42.1	31.0
$Z \rightarrow \tau\tau$ (OS-SS)	21.7	50.2	28.1
Diboson (OS-SS)	18.6	42.1	39.4
$Z \rightarrow ll$ (OS-SS)	13.4	57.6	29.1
W+jets (OS-SS)	18.7	41.6	39.7
Top (OS-SS)	26.7	41.3	32.1
Same sign data	20.0	47.9	32.1
Total Background	20.4	49.8	29.8
Data	21.4	50.1	28.5

Table 6.9: Fraction of 0-jet $e\tau_h$ events in the 0-jet $e\tau_h$ 1-prong-no-π^0s, 1-prong-with-π^0s and 3-prong subcategories. The fractions are given in percent of the total events in the 0-jet $e\tau_h$ category.

Process	Fraction of Events in 0-jet $\mu\tau_h$ in %		
	1-prong-no-π^0s	1-prong-with-π^0s	3-prong
Signal VBF125	20.1	50.7	29.3
Signal WH125	05.2	23.6	71.3
Signal ZH125	26.0	46.8	27.2
Signal ggF125	27.2	46.5	26.3
Total Signal	27.0	46.5	26.5
$Z \rightarrow \tau\tau$ (OS-SS)	22.0	50.7	27.3
Diboson (OS-SS)	16.9	49.3	33.9
$Z \rightarrow ll$ (OS-SS)	135.8	-56.1	20.3
W+jets (OS-SS)	32.8	35.4	31.9
Top (OS-SS)	15.8	62.2	22.1
Same sign data	22.6	50.9	26.6
Total Background	23.2	49.3	27.5
Data	23.4	49.1	27.5

Table 6.10: Fraction of 0-jet $\mu\tau_h$ events in the 0-jet $\mu\tau_h$ 1-prong-no-π^0s, 1-prong-with-π^0s and 3-prong subcategories. The fractions are given in percent of the total events in the 0-jet $\mu\tau_h$ category.

Process	Fraction of Events in 1-jet $e\tau_h$ in %		
	1-prong-no-π^0s	1-prong-with-π^0s	3-prong
Signal VBF125	29.201	45.7577	25.0413
Signal WH125	29.8162	47.24	22.9437
Signal ZH125	30.5103	43.5992	25.8905
Signal ggF125	27.6454	47.5333	24.8212
Total Signal	28.0679	47.1338	24.7983
$Z \to \tau\tau$ (OS-SS)	26.1728	48.6075	25.2198
Diboson (OS-SS)	27.36	45.868	26.772
$Z \to ll$ (OS-SS)	28.0908	57.7006	14.2087
W+jets (OS-SS)	30.815	51.1106	18.0744
Top (OS-SS)	25.1691	46.9971	27.8338
Same sign data	22.1811	46.3692	31.4497
Total Background	25.2689	48.2037	26.5274
Data	23.0315	48.2471	28.7214

Table 6.11: Fraction of 0-jet $e\tau_h$ events in the 0-jet $e\tau_h$ 1-prong-no-π^0s, 1-prong-with-π^0s and 3-prong subcategories. The fractions are given in percent of the total events in the 0-jet $e\tau_h$ category.

Process	Fraction of Events in 1-jet $\mu\tau_h$ in %		
	1-prong-no-π^0s	1-prong-with-π^0s	3-prong
Signal VBF125	28.8	48.1	23.0
Signal WH125	30.5	43.7	25.8
Signal ZH125	37.5	43.5	19.1
Signal ggF125	29.3	47.6	23.1
Total Signal	29.5	47.5	23.1
$Z \to \tau\tau$ (OS-SS)	24.7	49.6	25.7
Diboson (OS-SS)	27.4	46.1	26.5
$Z \to ll$ (OS-SS)	71.3	21.1	7.6
W+jets (OS-SS)	35.9	30.2	33.9
Top (OS-SS)	21.9	51.9	26.3
Same sign data	23.3	46.2	30.5
Total Background	26.0	46.2	27.8
Data	25.2	48.3	26.5

Table 6.12: Fraction of 0-jet $\mu\tau_h$ events in the 0-jet $\mu\tau_h$ 1-prong-no-π^0s, 1-prong-with-π^0s and 3-prong subcategories. The fractions are given in percent of the total events in the 0-jet $\mu\tau_h$ category.

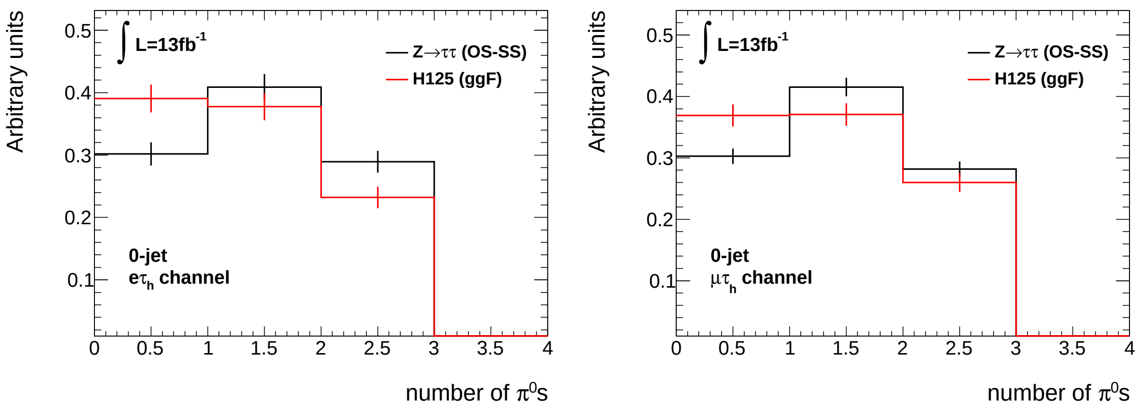

Figure 6.10: Distributions of the number of π^0s for 1-prong 0-jet $Z \longrightarrow \tau\tau$ and $H_{ggF} \longrightarrow \tau\tau$ events. Left plot: $e\tau_h$ events; Right plot: $\mu\tau_h$ events.

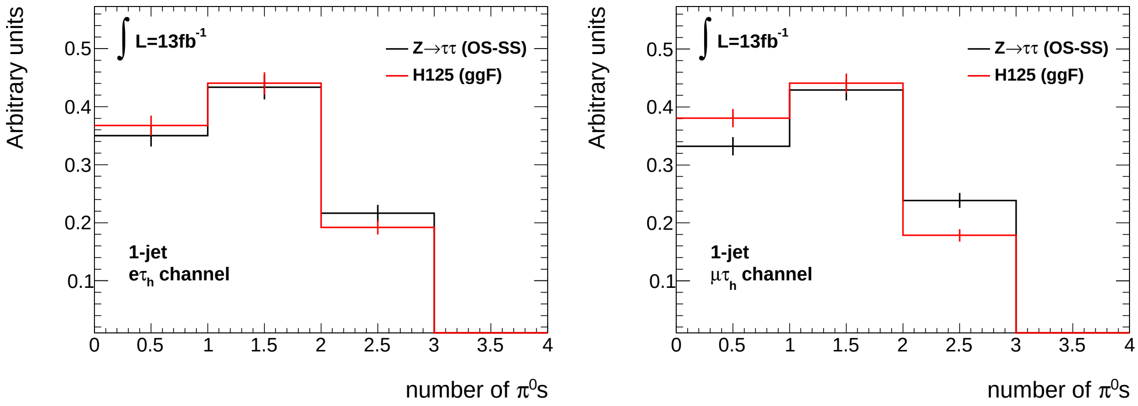

Figure 6.11: Distributions of the number of π^0s for 1-prong 1-jet $Z \longrightarrow \tau\tau$ and $H_{ggF} \longrightarrow \tau\tau$ events. Left plot: $e\tau_h$ events; Right plot: $\mu\tau_h$ events.

background component in the 1-jet category, this reduction is higher for 1-jet events than for 0-jet events.

The reduction of the $Z \longrightarrow \tau\tau$ background is more difficult to understand. One would expect the $Z \longrightarrow \tau\tau$ background to behave like the $H \longrightarrow \tau\tau$ signal. However, checks have shown that the tagging efficiency of the Pi0Finder algorithm towards 1-prong τ_h decays without π^0s is lower for $Z \longrightarrow \tau\tau$ events than for $H \longrightarrow \tau\tau$ events (cf. Fig. 6.10 and 6.11).

Due to the boost a τ_h originating from a $H \longrightarrow \tau\tau$ decay experiences, its transverse momentum is higher than the transverse momentum of a τ_h which originated from a $Z \longrightarrow \tau\tau$ decay. If the tagging efficiency of the Pi0Finder algorithm towards 1-prong τ_h decays without π^0s depends on the transverse momentum of the τ_h, more signal events than $Z \longrightarrow \tau\tau$ events would be reconstructed as 1-prong-no-π^0s τ_h. To check if this is the case, the normalized n_{π^0} distributions of $Z \longrightarrow \tau\tau$ and $H_{ggF} \longrightarrow \tau\tau$ events are compared for 20 GeV windows of the $p_T^{\tau_h}$. The following $p_T^{\tau_h}$ windows are used: 20 GeV< $p_T^{\tau_h}$ <40 GeV, 40 GeV< $p_T^{\tau_h}$ <60 GeV and 60 GeV< $p_T^{\tau_h}$ <80 GeV. Higher values of $p_T^{\tau_h}$ are not used, since the expected event rates are very low. The resulting comparison plots are shown in Fig. 6.12 and 6.13.

As can be seen in these plots, the fraction of $H \longrightarrow \tau\tau$ events is higher than the fraction of $Z \longrightarrow \tau\tau$ events for 1-prong-no-π^0 τ_h decays (bin 1) for all $p_T^{\tau_h}$ windows, whereas it is

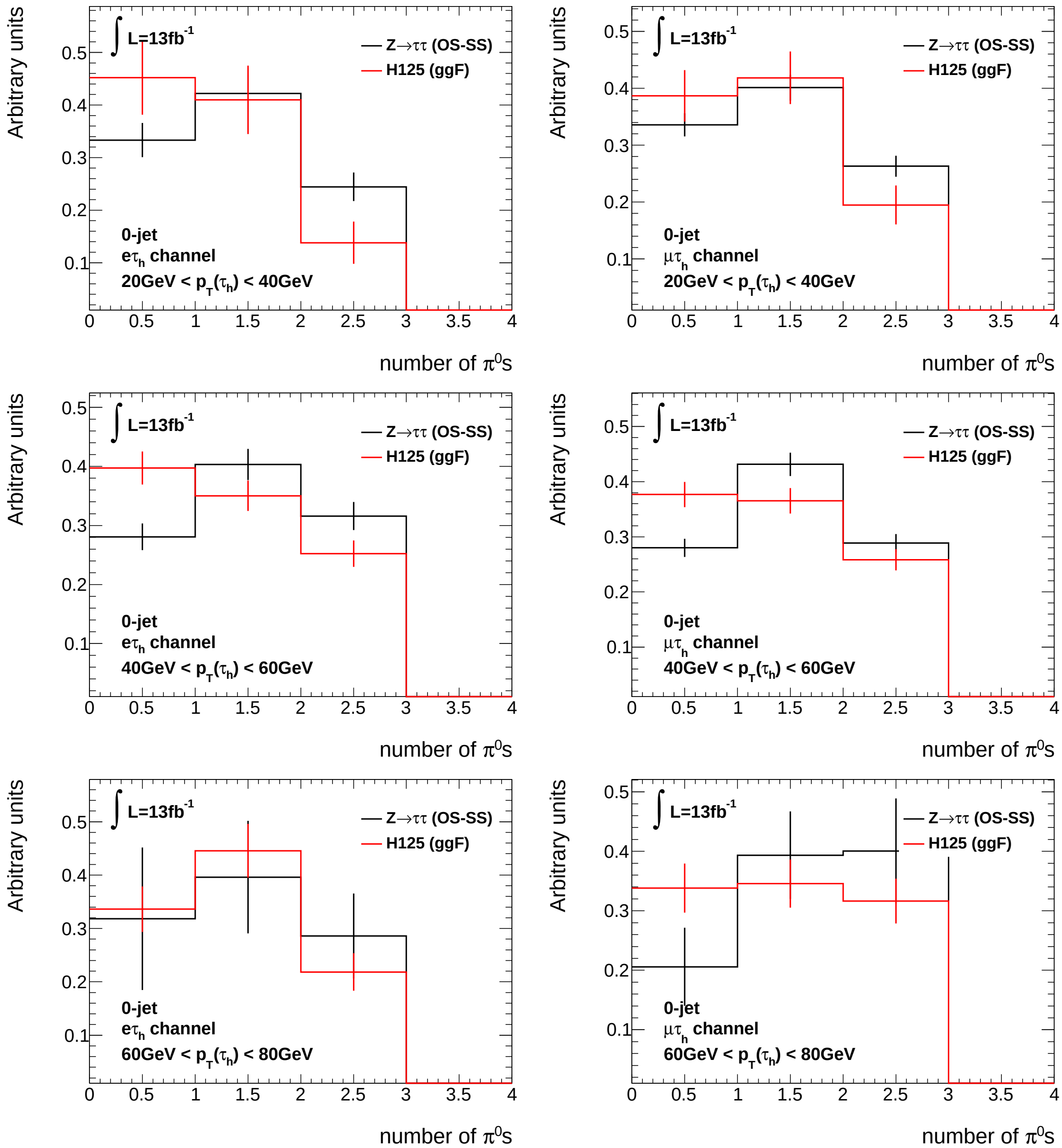

Figure 6.12: Distributions of the number of π^0s for 1-prong 0-jet $Z \rightarrow \tau\tau$ and $H_{ggF} \rightarrow \tau\tau$ events in 20 GeV windows of $p_T^{\tau_h}$. Left column: $e\tau_h$ events; Right column: $\mu\tau_h$ events. Top row: 20 GeV< $p_T^{\tau_h}$ <40 GeV window; Middle row: 40 GeV< $p_T^{\tau_h}$ <60 GeV window; Bottom row: 60 GeV< $p_T^{\tau_h}$ <80 GeV window.

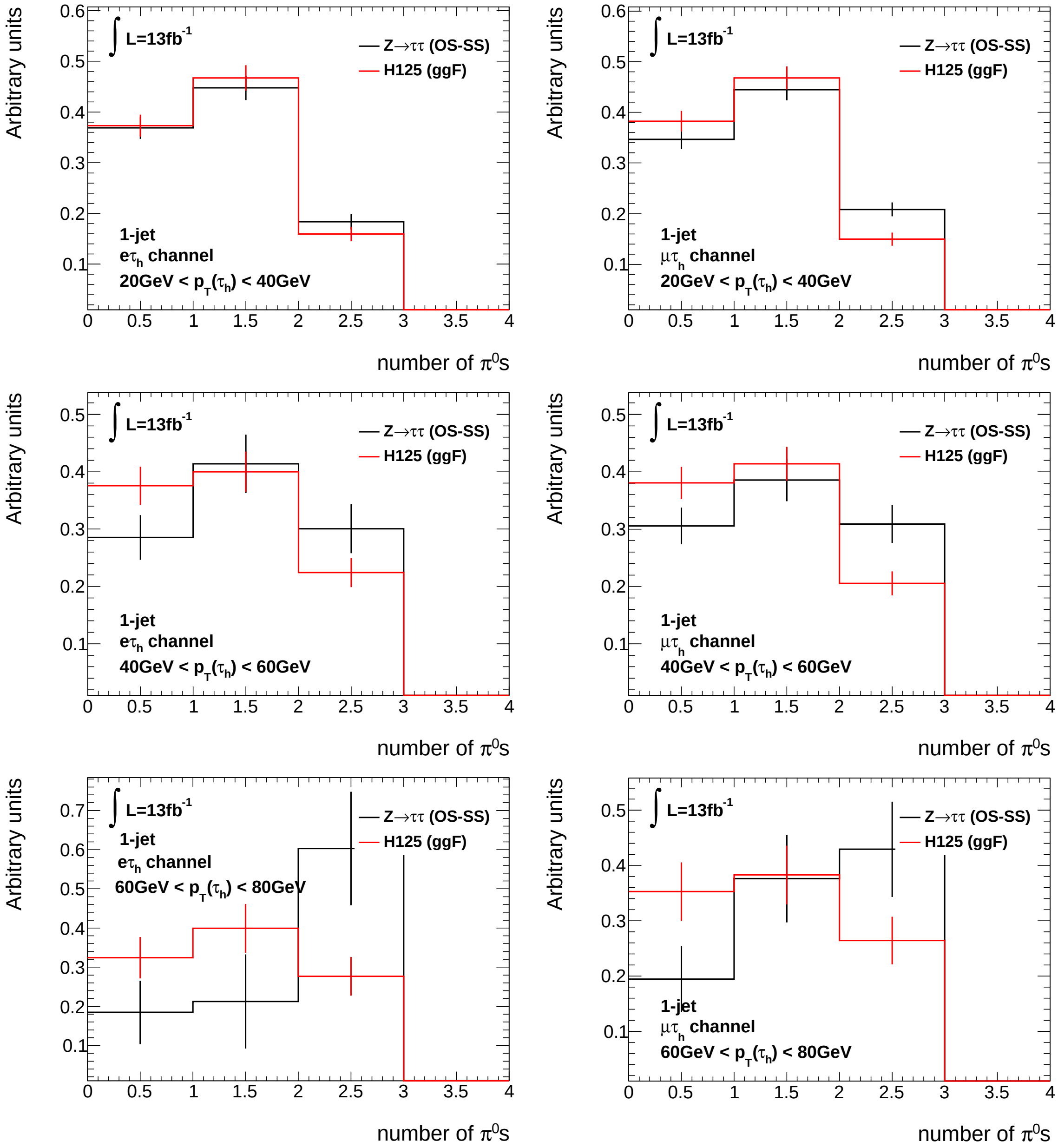

Figure 6.13: Distributions of the number of π^0s for 1-prong 1-jet $Z \to \tau\tau$ and $H_{ggF} \to \tau\tau$ events in 20 GeV windows of $p_T^{\tau_h}$. Left column: $e\tau_h$ events; Right column: $\mu\tau_h$ events. Top row: 20 GeV$<$ $p_T^{\tau_h}$ $<$40 GeV window; Middle row: 40 GeV$<$ $p_T^{\tau_h}$ $<$60 GeV window; Bottom row: 60 GeV$<$ $p_T^{\tau_h}$ $<$80 GeV window.

		95% CL_s exclusion limits on σ/σ_{SM}					
		nominal	nominal+$p_T^{\tau_h}$	1p3p	1p3p+$p_T^{\tau_h}$	1p$\pi^0$3p	1p$\pi^0$3p+$p_T^{\tau_h}$
σ/σ_{SM}	0-jet	$9.88^{14.49}_{7.12}$	$9.56^{14.06}_{6.89}$	$9.03^{13.27}_{6.50}$	$8.80^{12.91}_{6.34}$	$8.39^{12.34}_{6.04}$	$8.27^{12.14}_{6.00}$
	1-jet	$9.26^{13.37}_{6.67}$	$9.19^{13.22}_{6.62}$	$7.63^{11.12}_{5.50}$	$7.40^{10.84}_{5.33}$	$7.23^{10.53}_{5.21}$	$7.03^{10.10}_{5.06}$

Table 6.13: Blinded expected 95% CL_s exclusion limits for different subcategory combinations at the $m_H = 125\,\text{GeV}$ mass point. For the expected limits the $\pm 1\sigma$ values are given. The column labels correspond to the following category combinations: *nominal* - categorization as a single 0-/1-jet category as used by the reference analysis [33]; *1p3p* - intermediate categorization in 1- and 3-prong events, not regarding any π^0 related information; *1p$\pi^0$3p* - the 0- and 1-jet events are split up into the subcategories introduced in the previous section; X + $p_T^{\tau_h}$ - categorization is done as above and the cut on the τ_h transverse momentum is raised to $p_T(\tau_h) > 30\,\text{GeV}$ ($p_T(\tau_h) > 25\,\text{GeV}$) for 0-jet (1-jet) subcategories.

the opposite for τ_h decays with π^0s (bin 2 and 3 combined). The tagging efficiency of the Pi0Finder algorithm is therefore not dependent on $p_T^{\tau_h}$. The reason for this is not clear and remains an interesting open question.

To probe if the higher fraction of signal events in the 1-prong-no-π^0s subcategory affects the expected sensitivity when all systematic uncertainties are taken into account, the expected 95% CL_s exclusion limits are calculated for several combinations of subcategories. These calculations are done for a Higgs-boson mass of $m_H = 125\,\text{GeV}$. Also different cut values on the transverse τ_h momentum are considered. This means that, for example, not only the expected limit for the combination of the six 0-jet subcategories is calculated, but also the expected limit of the combination of the 0-jet $e\tau_h$ and $\mu\tau_h$, 1- and 3-prong subcategories. The combination with the lowest 95% CL_s expected exclusion limit is chosen. For the chosen combination the 95% CL_s exclusion limits are then calculated for the mass range $115 < m_H < 140\,\text{GeV}$ and compared to the results derived with categorization of the reference analysis.

The expected 95% CL_s exclusion limits for the $m_H = 125\,\text{GeV}$ mass point and the combinations of subcategories are shown in Table 6.13. Indicated by the superscript and subscript are the $\pm 1\sigma$ values of the corresponding 95% CL_s limit. The column labels correspond to the following category combinations:

nominal: The 0- and 1-jet categories are treated as single inclusive categories as used by the reference analysis (cf. Ref. [33]) and introduced in Section 5.1.2.

1p3p: The 0- and 1-jet categories as introduced in Section 5.1.2 are split up into the subcategories: 0-jet-1-prong, 0-jet-3-prong, 1-jet-1-prong and 1-jet-3-prong.

1p$\pi^0$3p: The categorization into twelve subcategories considering π^0s as introduced in the previous section is used.

X + $p_T^{\tau_h}$: In addition to one of the categorizations mentioned above a cut on $p_T(\tau_h) > 30\,\text{GeV}$ ($p_T(\tau_h) > 25\,\text{GeV}$) for 0-jet (1-jet) categories is applied.

In general, all categories were split up into an $e\tau_h$ and $\mu\tau_h$ channel prior to the limit calculation.

As can be seen in Table 6.13 the greatest improvements in sensitivity with respect to the nominal analysis categorization are achieved by a split into subcategories as introduced in the previous section for the 0- and 1-jet categories and applying a tighter momentum cut of $p_T^{\tau_h} > 30\,\mathrm{GeV}$ and $p_T^{\tau_h} > 25\,\mathrm{GeV}$, respectively (0-/1-jet 1p$\pi^0$3p + $p_T^{\tau_h}$). The individual improvements are of the order of $\mathcal{O}(16\%)$ for the 0-jet and $\mathcal{O}(24\%)$ for the 1-jet based category splitting, respectively.

The discriminating variable in the limit calculation is the MMC mass (m_{MMC}) of the di-tau system. The m_{MMC} mass distributions for each subcategory after applying the thighter cut on $p_T^{\tau_h}$ are shown in Fig. 6.14 and 6.15. The m_{MMC} distributions of the nominal 0- and 1-jet categories as described in Ref. [33] are shown in Fig. 6.16 and 6.17.

The data-to-MC agreement of the m_{MMC} distributions for the twelve subcategories is not perfect. This is due to low expected event rates in the subcategories. Also no systematic uncertainties on the Pi0Finder tagging efficiency are available. Therefore no observed, but only expected 95% exclusion limits are calculated. The expected limits are calculated over the mass range $115 \leq m_H \leq 140\,\mathrm{GeV}$ for the combinations of the six 0-jet and 1-jet based subcategories, respectively, after applying a tighter $p_T^{\tau_h}$ cut. They are then compared to the expected limits derived with the nominal categorization of the reference analysis.

In Fig. 6.18 (bottom plot) the expected 95% CL$_s$ exclusion limit for all 0-jet subcategories combined are shown (i.e. combination of 0-jet $e\tau_h/\mu\tau_h$ 1-prong-no-π^0/1-prong-with-π^0s/3-prong). Also a cut on $p_T(\tau_h) > 30\,\mathrm{GeV}$ was applied. As comparison the expected 95% CL$_s$ exclusion limit for the inclusive 0-jet category as defined by the reference analysis, are shown in the top plot of Fig. 6.18. The expected 95% CL$_s$ exclusion limits at the $m_H = 125\,\mathrm{GeV}$ mass point are found to be 9.88 for the inclusive treatment of the 0-jet category, and 8.27 for the combined limit of all 0-jet subcategories with $p_T(\tau_h) > 30\,\mathrm{GeV}$, respectively. This corresponds to an improvement of the expected limit of approximately 16%.

For the 1-jet category, the expected 95% CL$_s$ exclusion limit for the combination of all 1-jet subcategories after applying a $p_T(\tau_h) > 25\,\mathrm{GeV}$ cut is shown in Fig. 6.19 (bottom plot). As comparison the expected 95% CL$_s$ exclusion limit for the inclusive 1-jet category as defined by the reference analysis, is shown in the top plot of Fig. 6.19. The expected 95% CL$_s$ exclusion limits at the $m_H = 125\,\mathrm{GeV}$ mass point are found to be 9.26 for the inclusive treatment of the 1-jet category, and 7.03 for the combined limit of the all 1-jet based subcategories, respectively. This corresponds to an improvement of the expected limit of approximately 24%.

These results indicate an improvement of the sensitivity towards a SM Higgs-boson signal in the $H \to \tau_l\tau_h$ search channel. Also all other analyses with hadronic taus in the final state could profit from these studies.

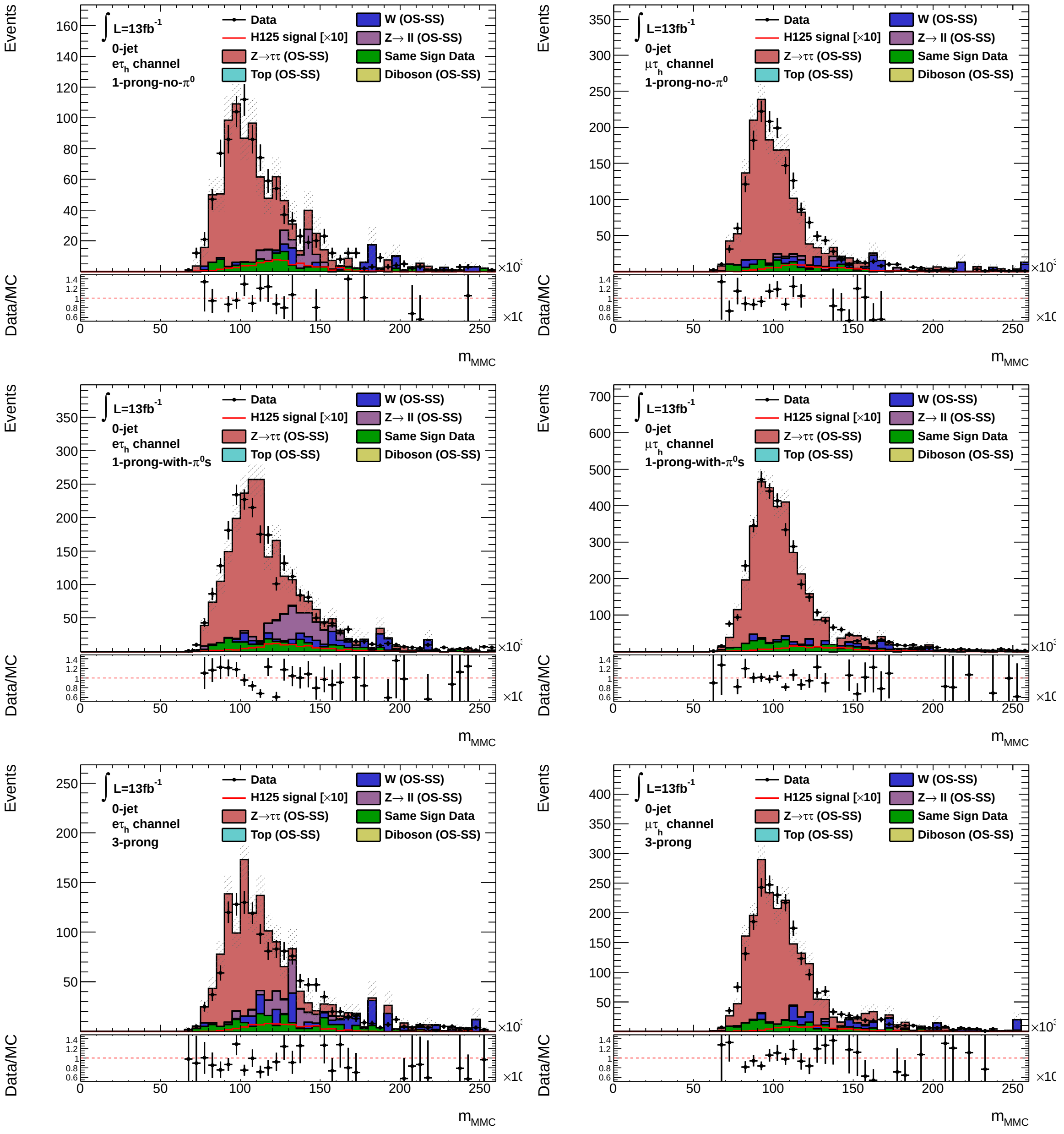

Figure 6.14: Distributions of the MMC mass (m_{MMC}) for all 0-jet subcategories after applying the $p_T^{\tau_h} > 30\,\mathrm{GeV}$ cut. Left column: 0-jet $e\tau_h$ subcategories; Right column: 0-jet $\mu\tau_h$ subcategories. Top row: 0-jet 1-prong-no-π^0 subcategories; Middle row: 0-jet 1-prong-with-π^0s subcategories; Bottom row: 0-jet 3-prong subcategories.

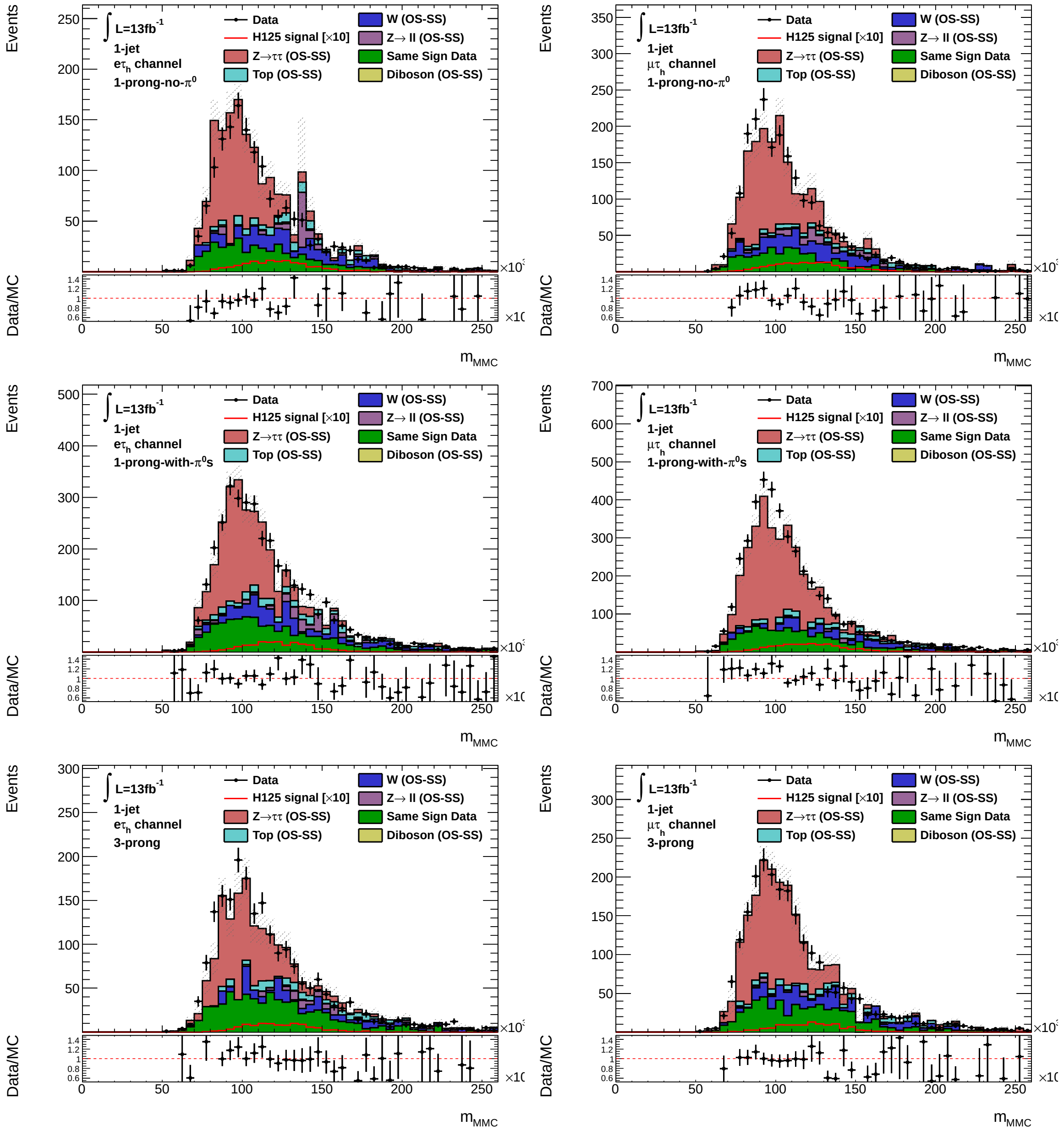

Figure 6.15: Distributions of the MMC mass (m_{MMC}) for all 1-jet subcategories after applying the $p_T^{\tau_h} > 25\,\mathrm{GeV}$ cut. Left column: 1-jet $e\tau_h$ subcategories; Right column: 1-jet $\mu\tau_h$ subcategories. Top row: 1-jet 1-prong-no-π^0 subcategories; Middle row: 1-jet 1-prong-with-π^0s subcategories; Bottom row: 1-jet 3-prong subcategories.

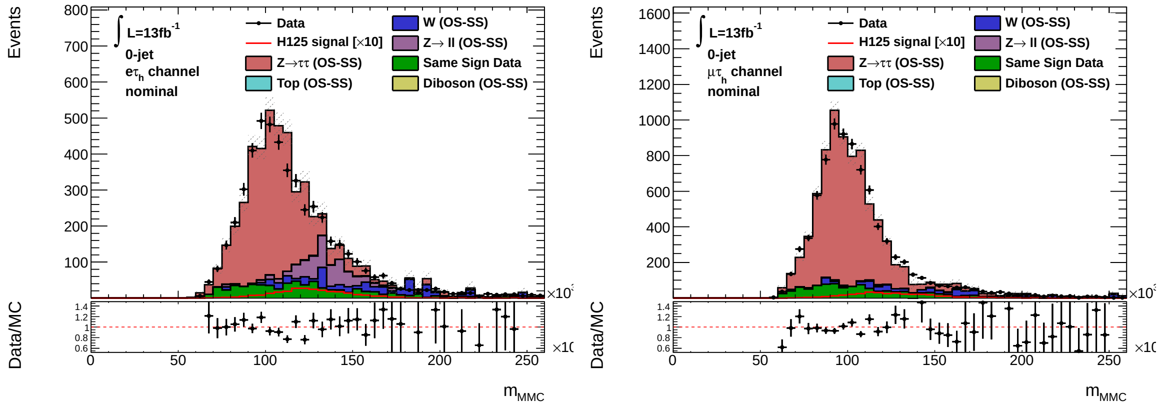

Figure 6.16: Distributions of the MMC mass (m_{MMC}) for the superior 0-jet $e\tau_h$ (left) and $\mu\tau_h$ (right) categories after nominal selection as defined by the reference analysis (cf. Ref. [33]).

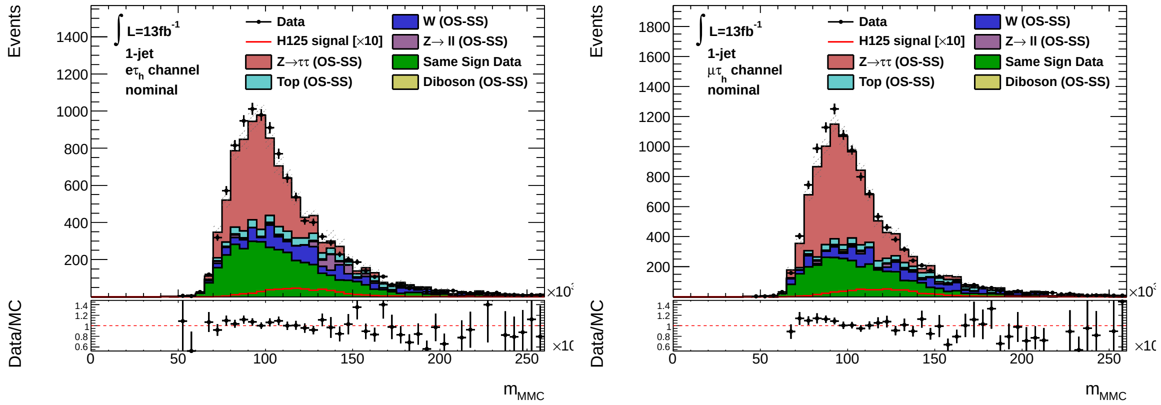

Figure 6.17: Distributions of the MMC mass (m_{MMC}) for the superior 1-jet $e\tau_h$ (left) and $\mu\tau_h$ (right) categories after nominal selection as defined by the reference analysis (cf. Ref. [33]).

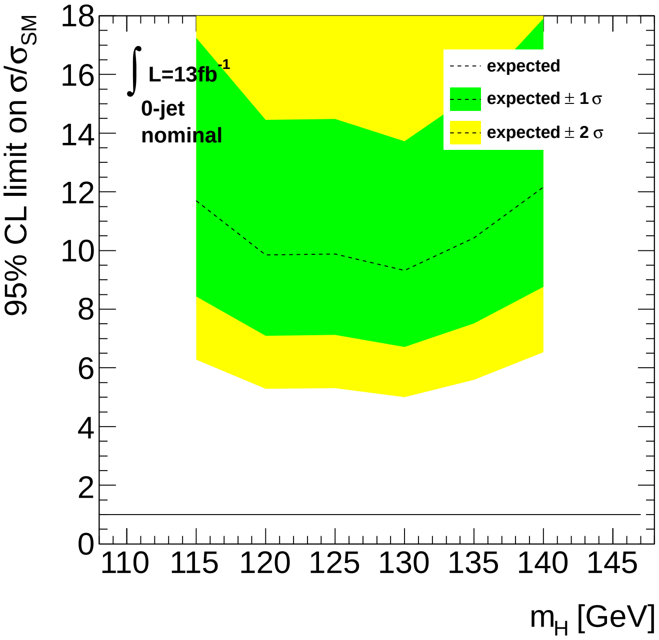

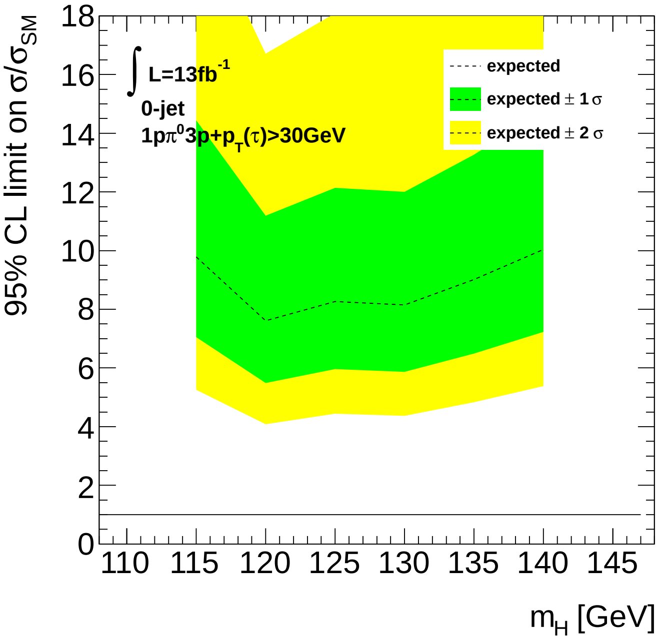

Figure 6.18: Expected (dashed line) 95% CL_s exclusion limits for the inclusive 0-jet category (top plot) and for all 0-jet subcategories combined after applying a $p_T(\tau_h) > 30\,\mathrm{GeV}$ cut (bottom plot).

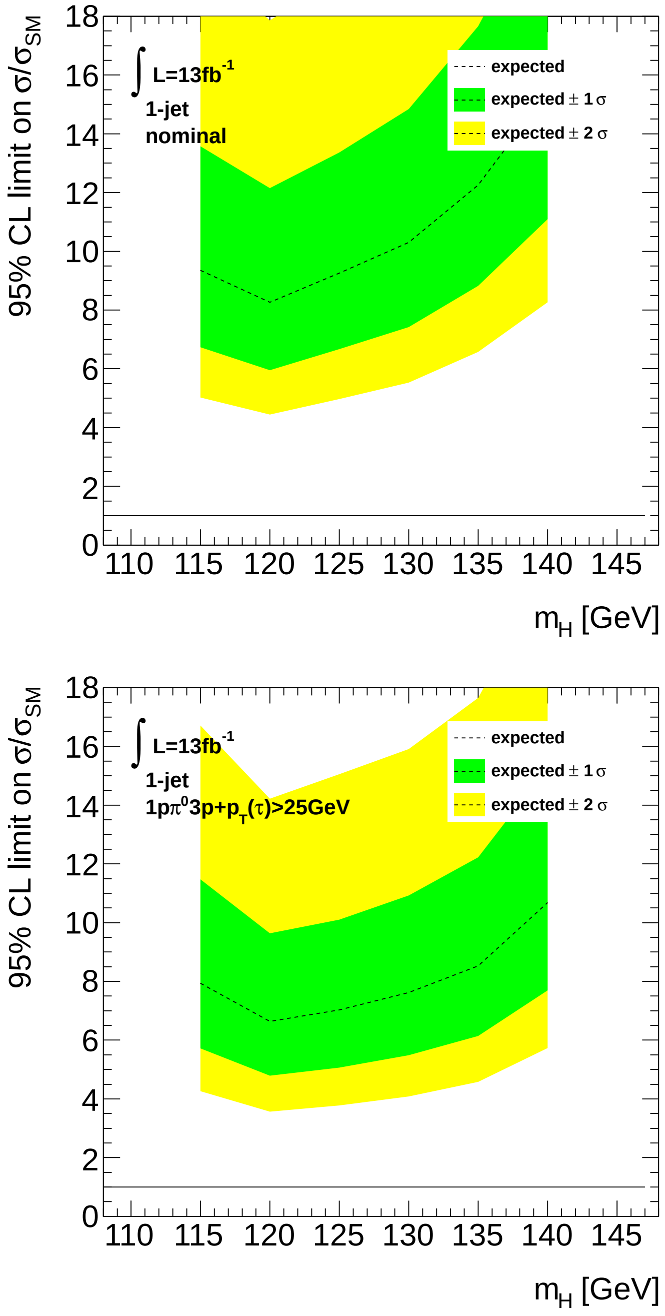

Figure 6.19: Expected (dashed line) 95% CL$_s$ exclusion limits for the inclusive 1-jet category (top plot) and for all 1-jet subcategories combined after applying a $p_T(\tau_h) > 25\,\text{GeV}$ cut (bottom plot).

7 Summary

In Summer 2012 a new bosonic resonance with a mass of 126 GeV, compatible with the Standard Model Higgs boson, was discovered independently by the ATLAS and CMS collaborations. However, no Higgs-boson signal could be observed in the $H \to \tau^+\tau^-$ or $H \to b\bar{b}$ search channels. These search channels are of special interest, since they can directly probe the coupling of the Higgs boson to fermions. The $H \to \tau^+\tau^-$ has one of the highest $\sigma \times BR$ in the low mass region and is the only channel in which the coupling of the Higgs boson to leptons can be directly probed. However, the analyses contributing to this search channel are not sensitive enough to exclude or confirm a Higgs-boson signal with the currently available data set.

In this thesis it was investigated if an improvement of the sensitivity can be achieved by including information on the decay of the hadronic tau in the $H \to \tau_l\tau_h$ analysis. The analysis was performed for the 0- and 1-jet categories of the $H \to \tau_l\tau_h$ decay mode. The study was done on data corresponding to an integrated luminosity of $13\,\mathrm{fb}^{-1}$, which was collected by the ATLAS experiment in 2012 at a center-of-mass energy of $\sqrt{s} = 8\,\mathrm{TeV}$.

In a first step, subcategories of the 0- and 1-jet categories were defined based on the pions in the τ_h decay. The background composition of these subcategories was investigated and it was tested if the estimation of the W background depends on the τ_h substructure. It was shown that the changes in the W-background correction factors have only minimal effect on the overall background estimation and can be neglected.

A comparison of π^0-based kinematic variables of the τ_h with their regularly derived equivalents was performed. The study on the visible mass of the lepton-tau system has shown, that the sensitivity towards a SM Higgs-boson signal does not improve if information about neutral pions in the hadronic tau decay is included in the mass reconstruction. No calibration has been done for the π^0-based variables and no systematic uncertainties resulting from the reconstruction of the neutral pions are currently available.

It was shown that the fraction of signal events in the 1-prong-no-π^0s subcategory of the 0- and 1-jet $e\tau_h$ and $\mu\tau_h$ channels is higher than the fraction of background events in the same subcategory. The reason for this is the tagging efficiency of the Pi0Finder algorithm towards 1-prong τ_h decays without π^0s, which is higher for $H \to \tau\tau$ signal events than for $Z \to \tau\tau$ events. In a first attempt to explain this difference in the tagging efficiency, it was tested if the tagging efficiency depends on the transverse momentum of the τ_h ($p_T^{\tau_h}$), which is expected to be higher for signal events. However, no dependence of the tagging efficiency on the $p_T^{\tau_h}$ could be observed. The reason for the higher tagging efficiency of the Pi0Finder towards 1-prong τ_h decays without π^0s could not be found and remains an open question.

The higher fraction of signal events in the 1-prong-no-π^0s subcategories indicated an improvement in the sensitivity towards a SM Higgs-boson signal in the $H \to \tau_l\tau_h$ search channel. Therefore, expected upper limit exclusion limits were derived for combinations of the pion-based subcategories and compared to the corresponding exlusion limits of the pion-

inclusive 0- and 1-jet categories. It was shown that the subcategorization based on pions improves the expected sensitivity in the 0- and 1-jet categories of the $H \rightarrow \tau_l \tau_h$ decay mode by 16% and 24%, respectively. Therefore an improvement of the sensitivity towards a possible Higgs boson is possible for the complete analysis of the $H \rightarrow \tau^+ \tau^-$ decay mode.
This thesis presents the first analysis which uses pion-based subcategories in the $H \rightarrow \tau_l \tau_h$ search channel. Since no pion-based systematic uncertainties were available for the categorization, this thesis states preliminary results. Nevertheless, the results of this study can be transferred to other analyses using high statistic categories with hadronically decaying tau leptons.

A Studies on k_W

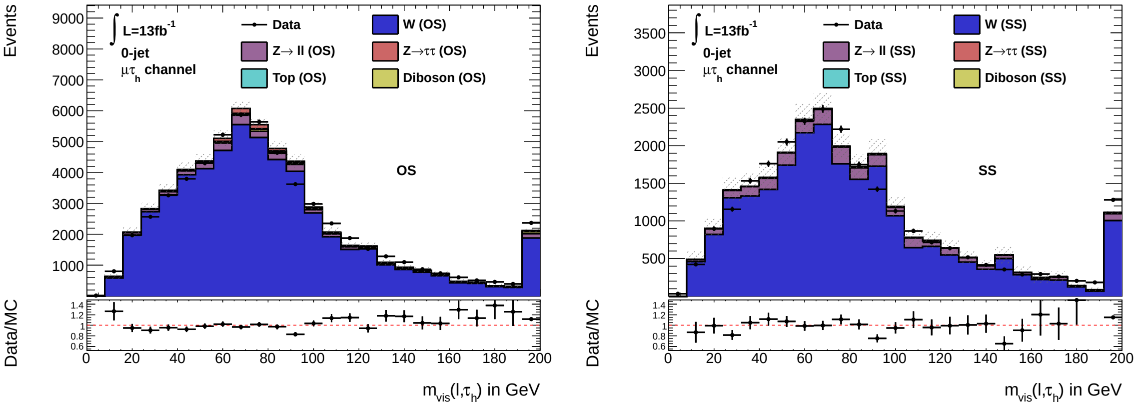

Figure A.1: Distributions of the m_{vis} in the W control regions for the 0-jet $e\tau_h$ category. Left plot: opposite sign (OS) W CR; Right plot: same sign (SS) W CR.

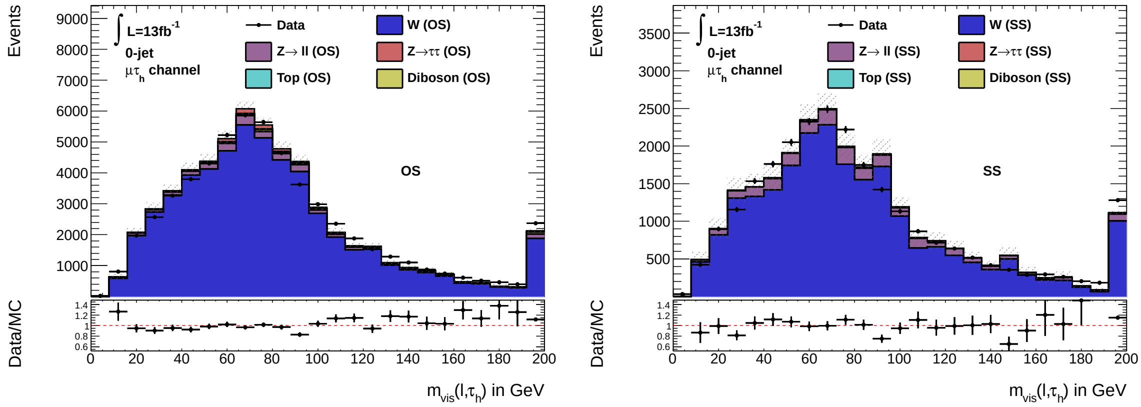

Figure A.2: Distributions of the m_{vis} in the W control regions for the 1-jet $\mu\tau_h$ category. Left plot: opposite sign (OS) W CR; Right plot: same sign (SS) W CR.

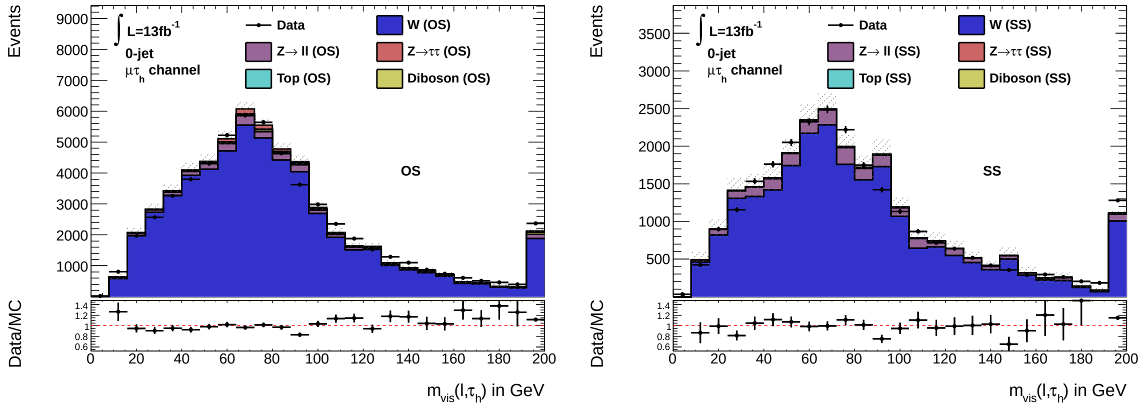

Figure A.3: Distributions of the m_{vis} in the W control regions for the 1-jet $e\tau_h$ category. Left plot: opposite sign (OS) W CR; Right plot: same sign (SS) W CR.

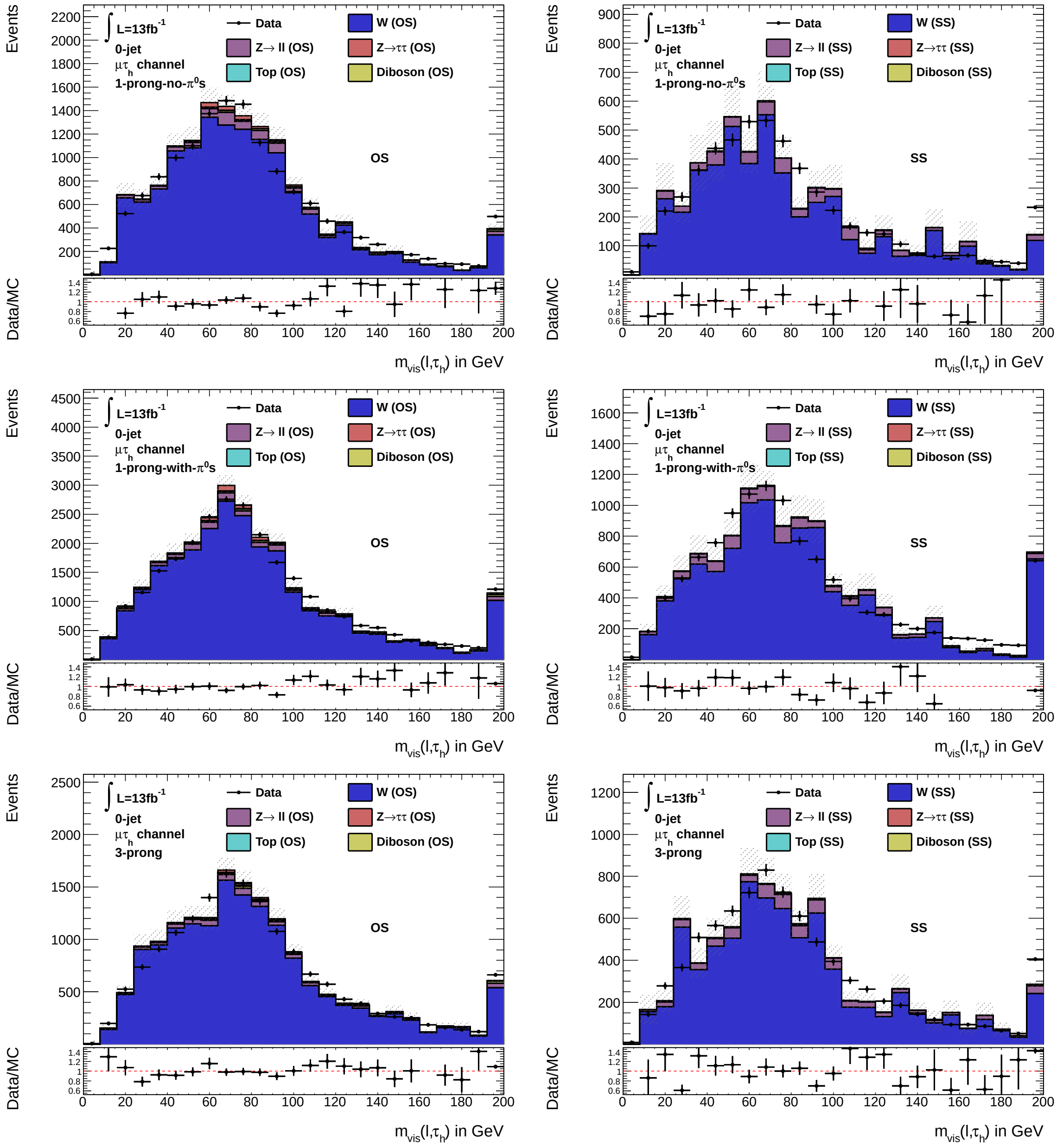

Figure A.4: Distributions of the m_{vis} in the W control regions for all 0-jet $e\tau_h$ subcategories. Left column: opposite sign (OS) W CR; Right column: same sign (SS) W CR. Top row: 0-jet $e\tau_h$ 1-prong-no-π^0 subcategory; Middle row: 0-jet $e\tau_h$ 1-prong-with-π^0s subcategory; Bottom row:0-jet $e\tau_h$ 3-prong subcategory.

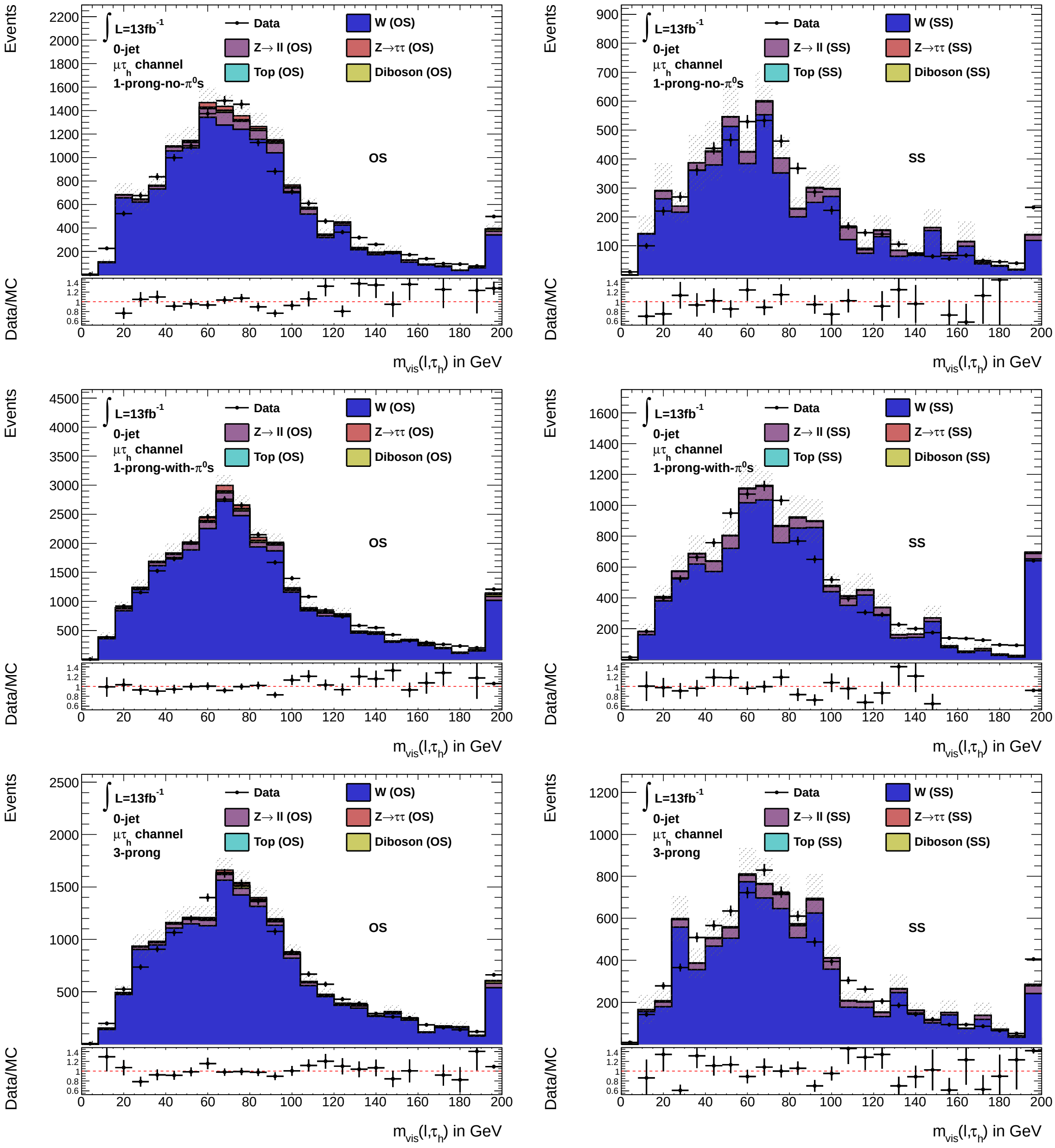

Figure A.5: Distributions of the m_{vis} in the W control regions for all 1-jet $\mu\tau_h$ subcategories. Left column: opposite sign (OS) W CR; Right column: same sign (SS) W CR. Top row: 1-jet $\mu\tau_h$ 1-prong-no-π^0 subcategory; Middle row: 1-jet $\mu\tau_h$ 1-prong-with-π^0s subcategory; Bottom row:1-jet $\mu\tau_h$ 3-prong subcategory.

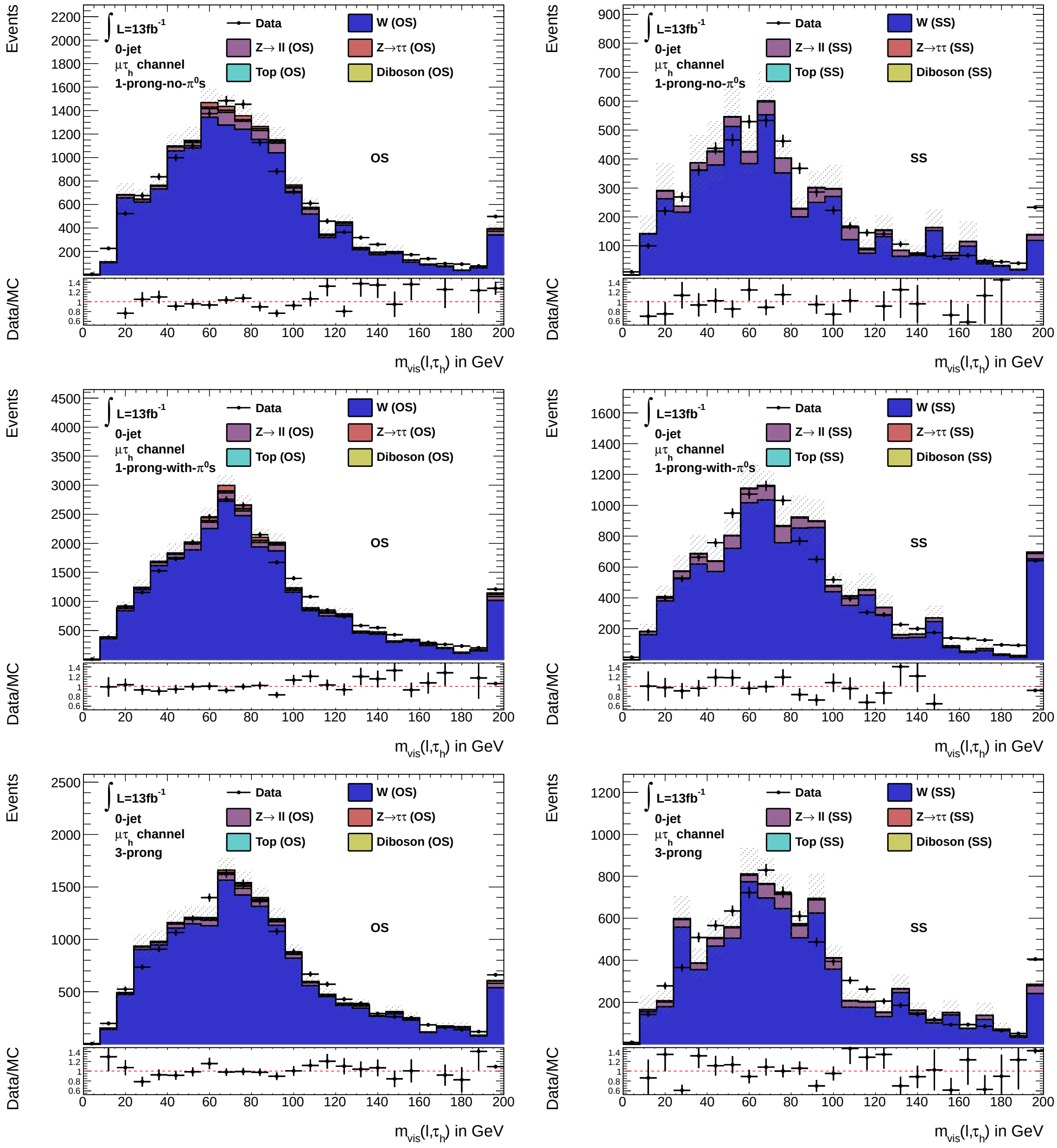

Figure A.6: Distributions of the m_{vis} in the W control regions for all 1-jet $e\tau_h$ subcategories. Left column: opposite sign (OS) W CR; Right column: same sign (SS) W CR. Top row: 1-jet $e\tau_h$ 1-prong-no-π^0 subcategory; Middle row: 1-jet $e\tau_h$ 1-prong-with-π^0s subcategory; Bottom row:1-jet $e\tau_h$ 3-prong subcategory.

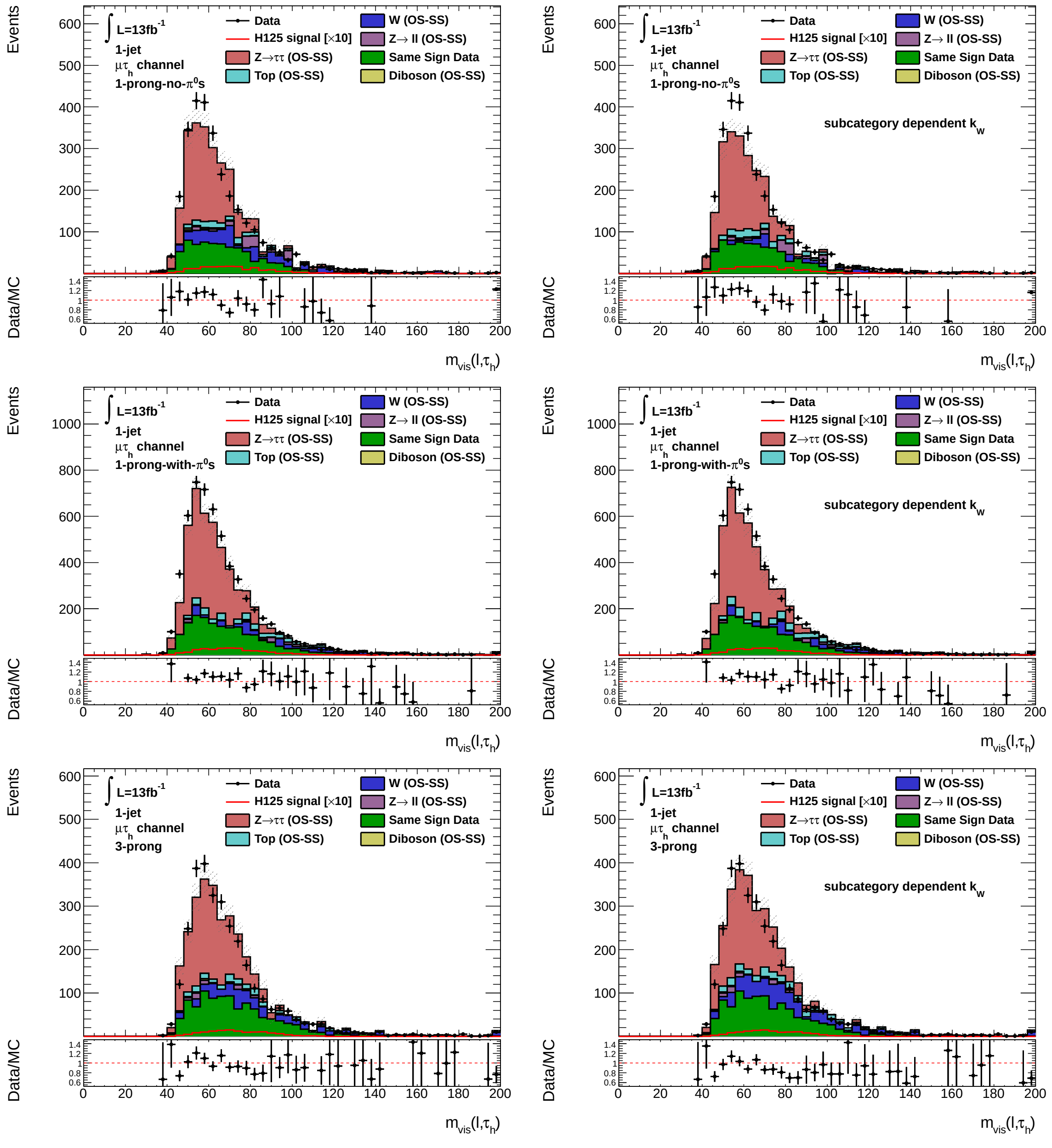

Figure A.7: Shown are the visible mass distributions of the lepton-τ_h system for the 1-jet $\mu\tau_h$ subcategories for different k_W factors. The m_{vis} distributions derived with the k_W factors taken from [33] are shown in the left column. In the right column the m_{vis} distributions derived with the subcategory dependent k_W factors are shown.

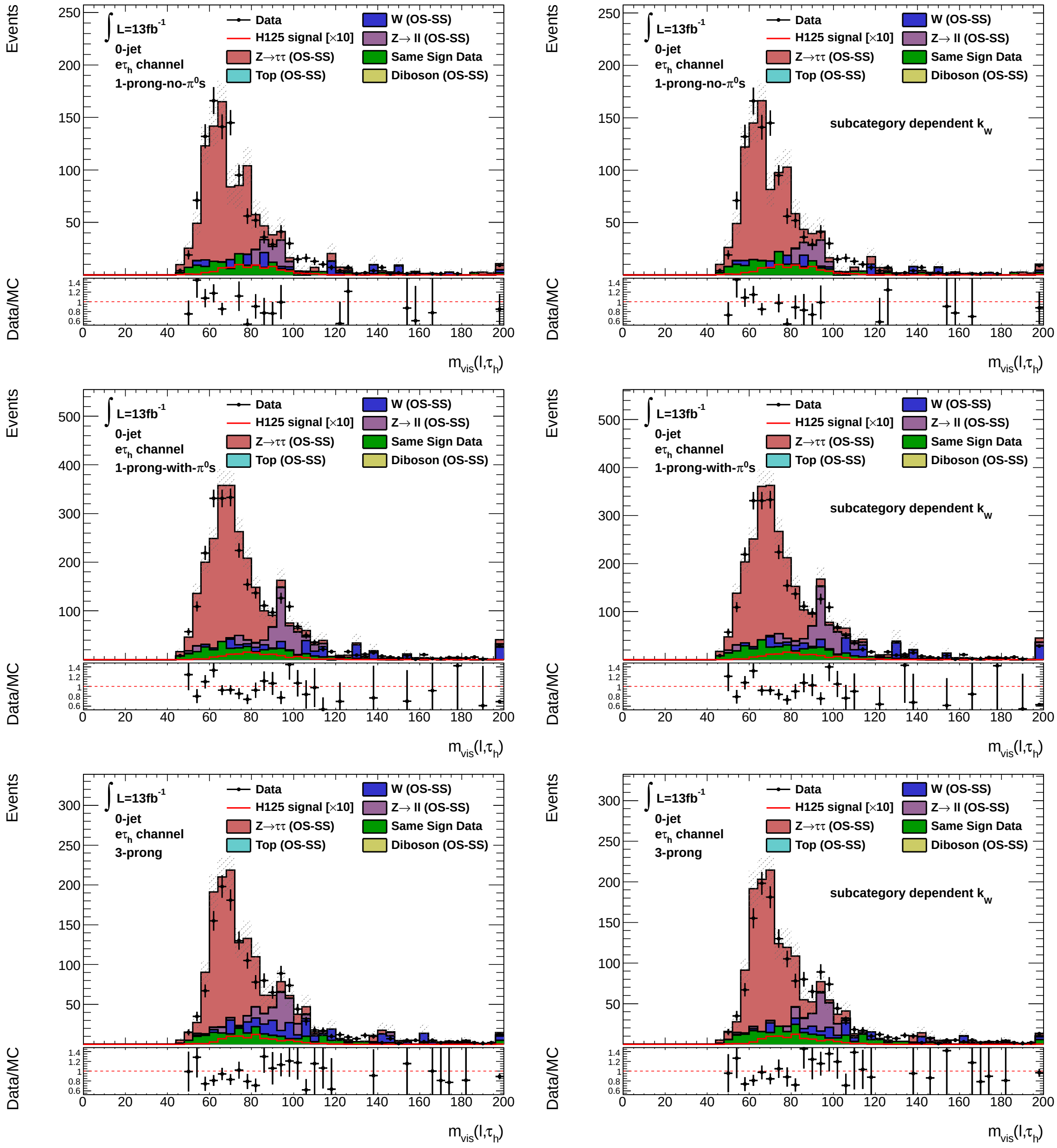

Figure A.8: Shown are the visible mass distributions of the lepton-τ_h system for the 0-jet $e\tau_h$ subcategories for different k_W factors. The m_{vis} distributions derived with the k_W factors taken from [33] are shown in the left column. In the right column the m_{vis} distributions derived with the subcategory dependent k_W factors are shown.

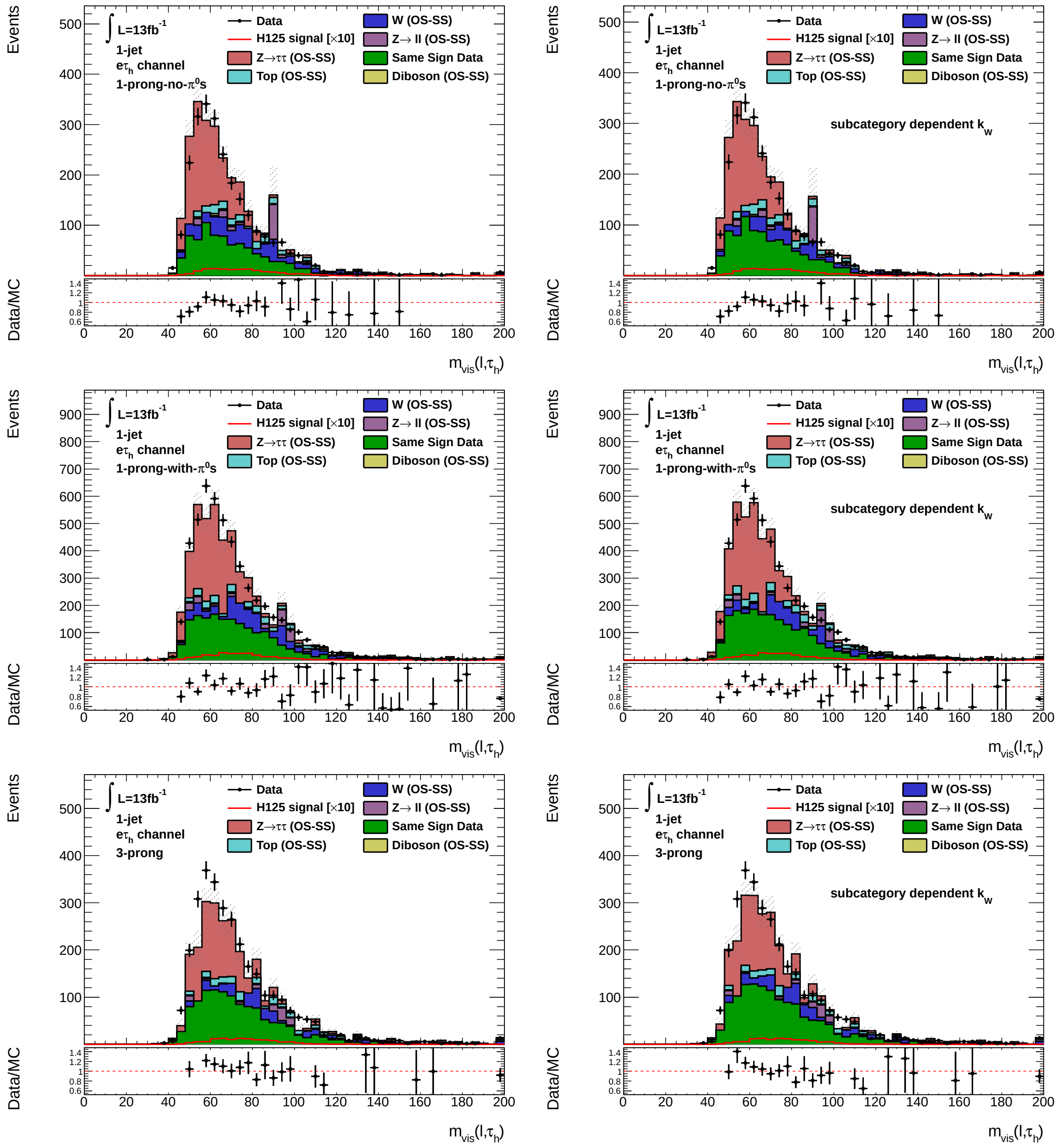

Figure A.9: Shown are the visible mass distributions of the lepton-τ_h system for the 1-jet $e\tau_h$ subcategories for different k_W factors. The m_{vis} distributions derived with the k_W factors taken from [33] are shown in the left column. In the right column the m_{vis} distributions derived with the subcategory dependent k_W factors are shown.

B Distributions of the π^0 based visible lepton-τ_h mass

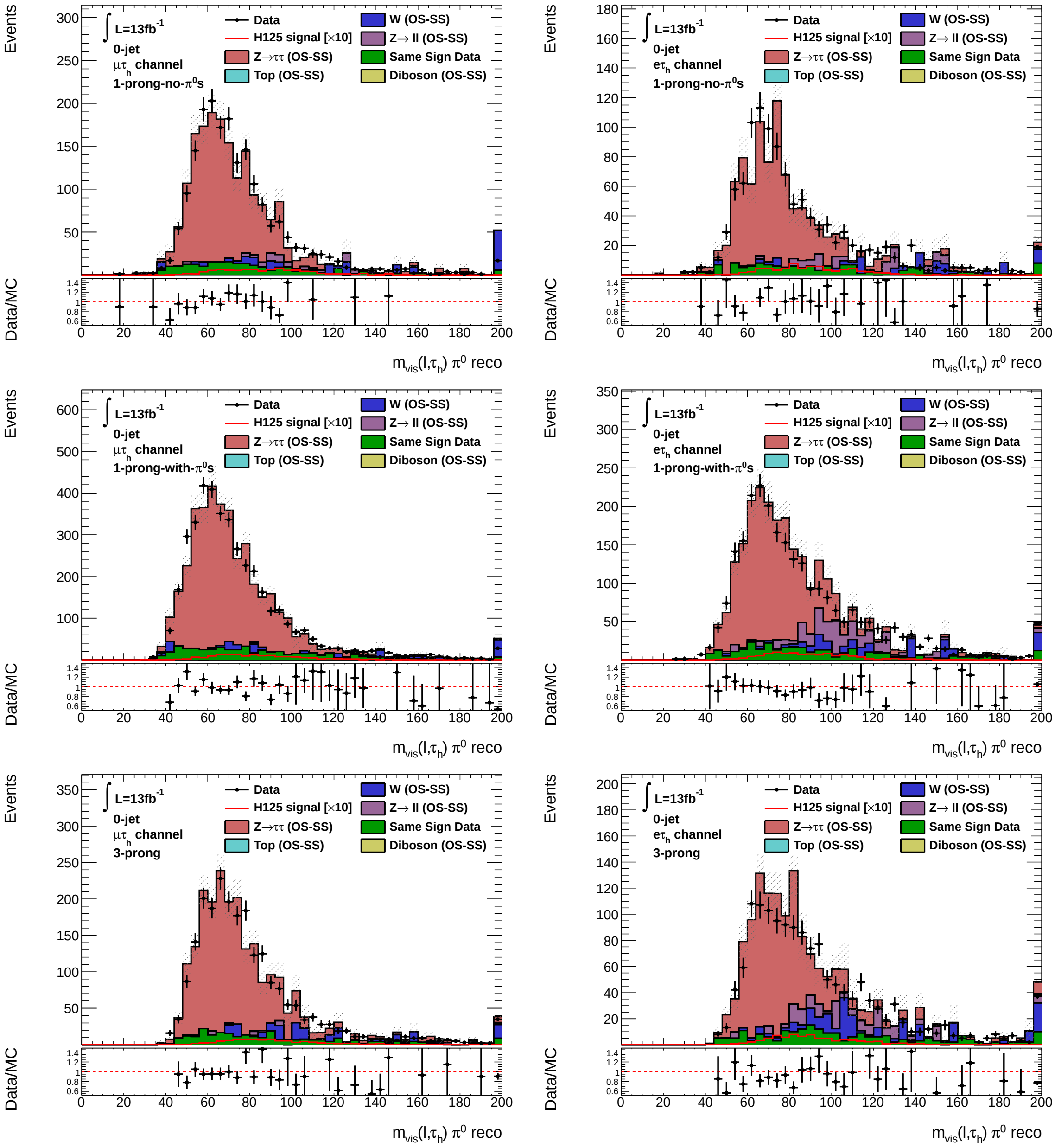

Figure B.1: Visible mass distributions for the 0-jet $\mu\tau_h$ (left column) and $e\tau_h$ (right column) subcategories, derived with the π^0 based transverse momentum of the τ_h ($m_{vis}^{\pi^0\ \mathrm{reco}}(l,\tau_h)$). $m_{vis}^{\pi^0\ \mathrm{reco}}$ is given in GeV.

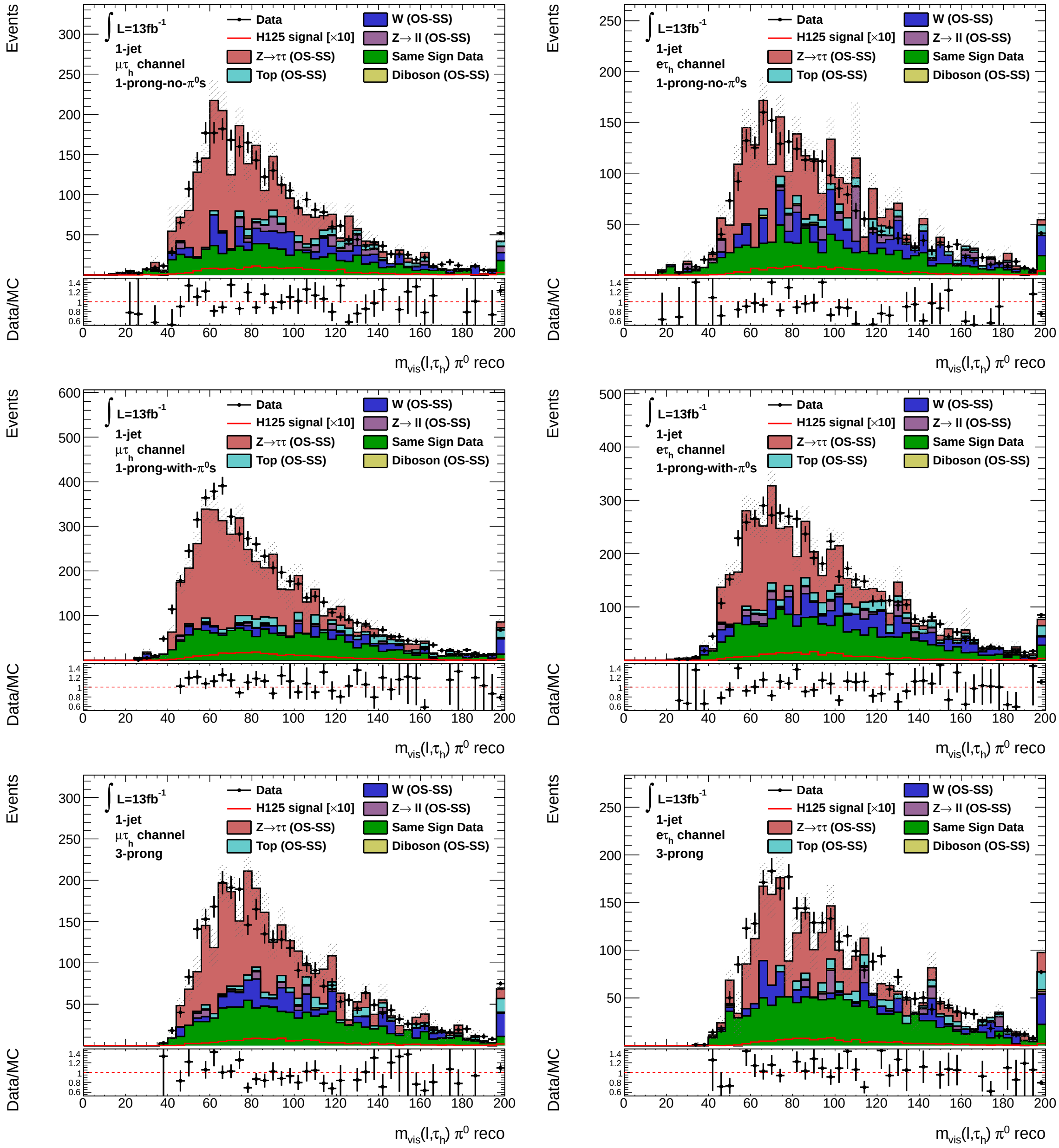

Figure B.2: Visible mass distributions for the 1-jet $\mu\tau_h$ (left column) and $e\tau_h$ (right column) subcategories, derived with the π^0 based transverse momentum of the τ_h ($m_{vis}^{\pi^0\text{ reco}}(l,\tau_h)$). $m_{vis}^{\pi^0\text{ reco}}$ is given in GeV.

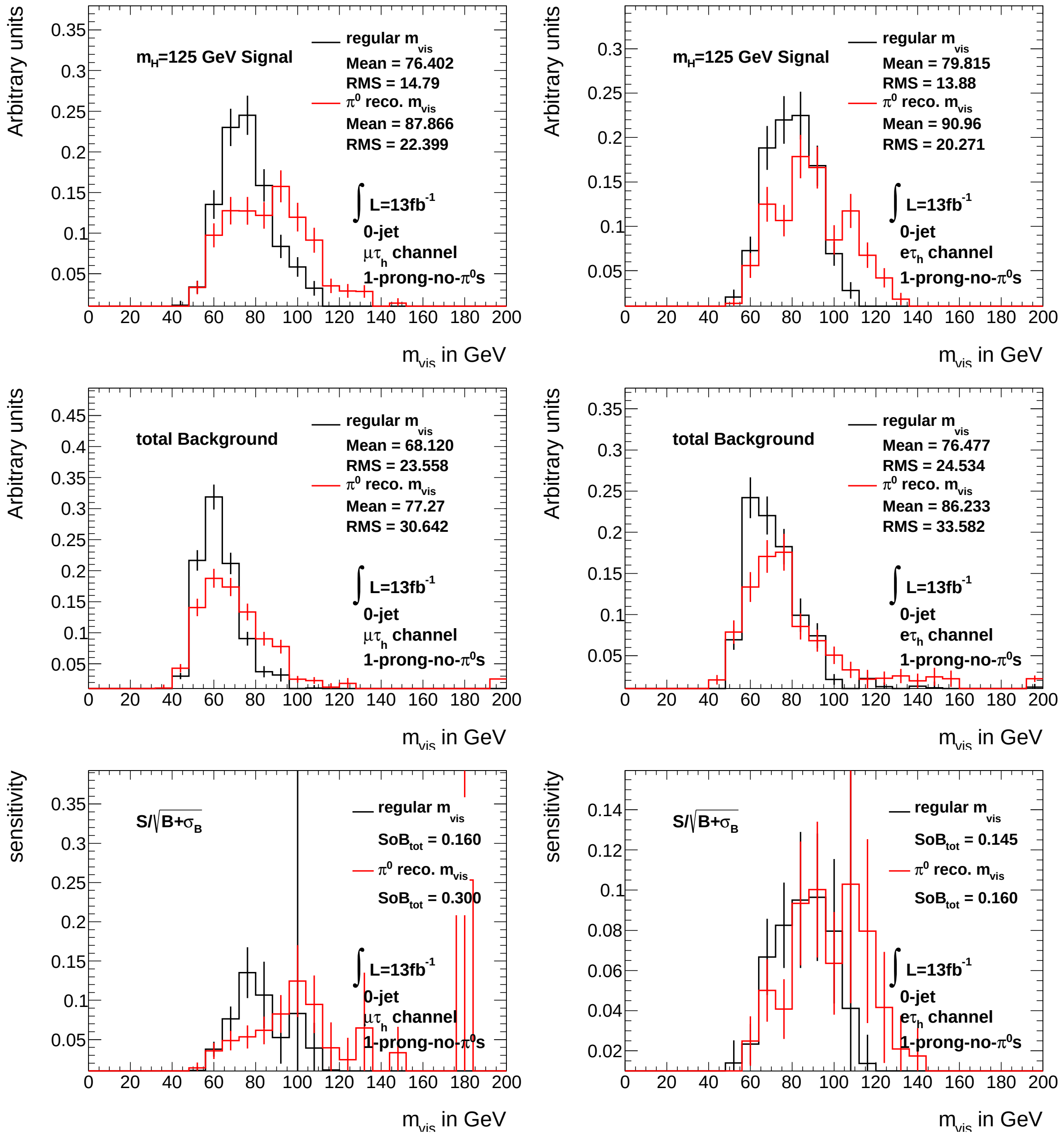

Figure B.3: Comparison of regular and with π^0 information reconstructed visible mass distributions of the $m_H = 125\,\mathrm{GeV}$ Higgs-boson signal (top row) and the total background (middle row). The corresponding expected sensitivity distributions are shown in the bottom row. All histograms are for the 0-jet 1-prong-no-π^0s category for the $\mu\tau_h$ channel (left column) and the $e\tau_h$ channel (right column).

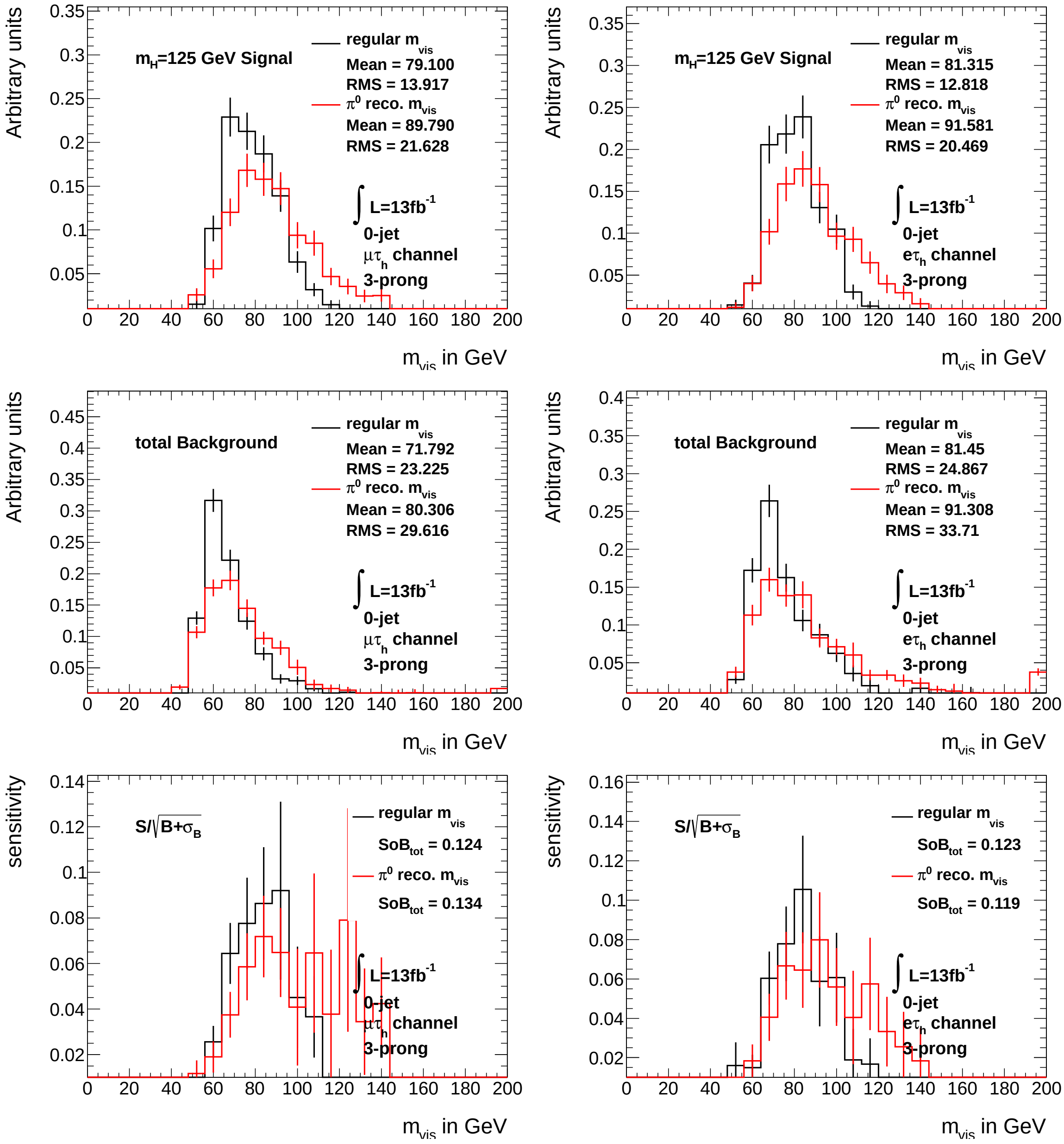

Figure B.4: Comparison of regular and with π^0 information reconstructed visible mass distributions of the $m_H = 125\,\text{GeV}$ Higgs-boson signal (top row) and the total background (middle row). The corresponding expected sensitivity distributions are shown in the bottom row. All histograms are for the 0-jet 3-prong category for the $\mu\tau_h$ channel (left column) and the $e\tau_h$ channel (right column).

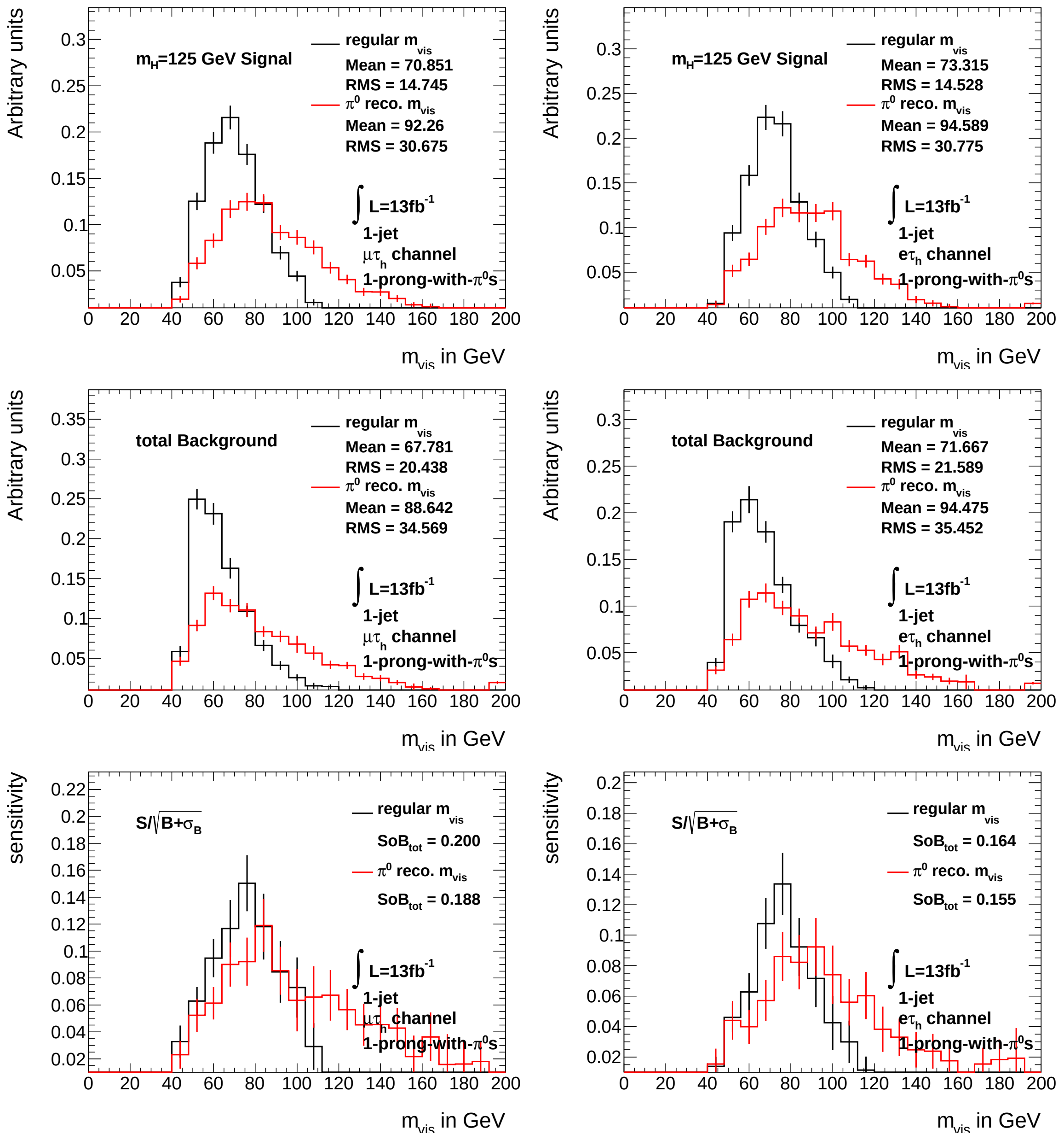

Figure B.5: Comparison of regular and with π^0 information reconstructed visible mass distributions of the $m_H = 125\,\text{GeV}$ Higgs-boson signal (top row) and the total background (middle row). The corresponding expected sensitivity distributions are shown in the bottom row. All histograms are for the 1-jet 1-prong-with-π^0s category for the $\mu\tau_h$ channel (left column) and the $e\tau_h$ channel (right column).

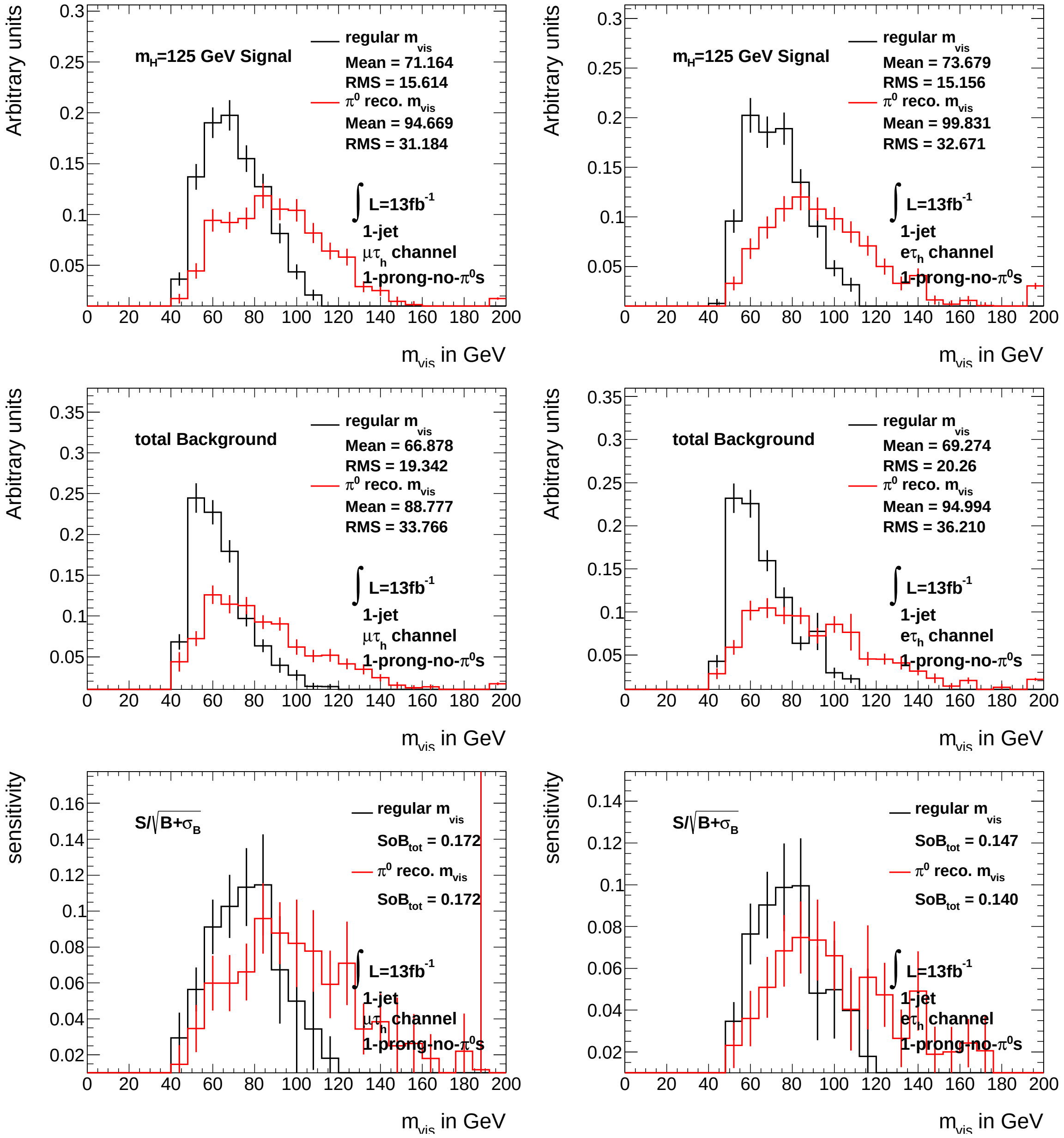

Figure B.6: Comparison of regular and with π^0 information reconstructed visible mass distributions of the $m_H = 125\,\mathrm{GeV}$ Higgs-boson signal (top row) and the total background (middle row). The corresponding expected sensitivity distributions are shown in the bottom row. All histograms are for the 1-jet 1-prong-no-π^0s category for the $\mu\tau_h$ channel (left column) and the $e\tau_h$ channel (right column).

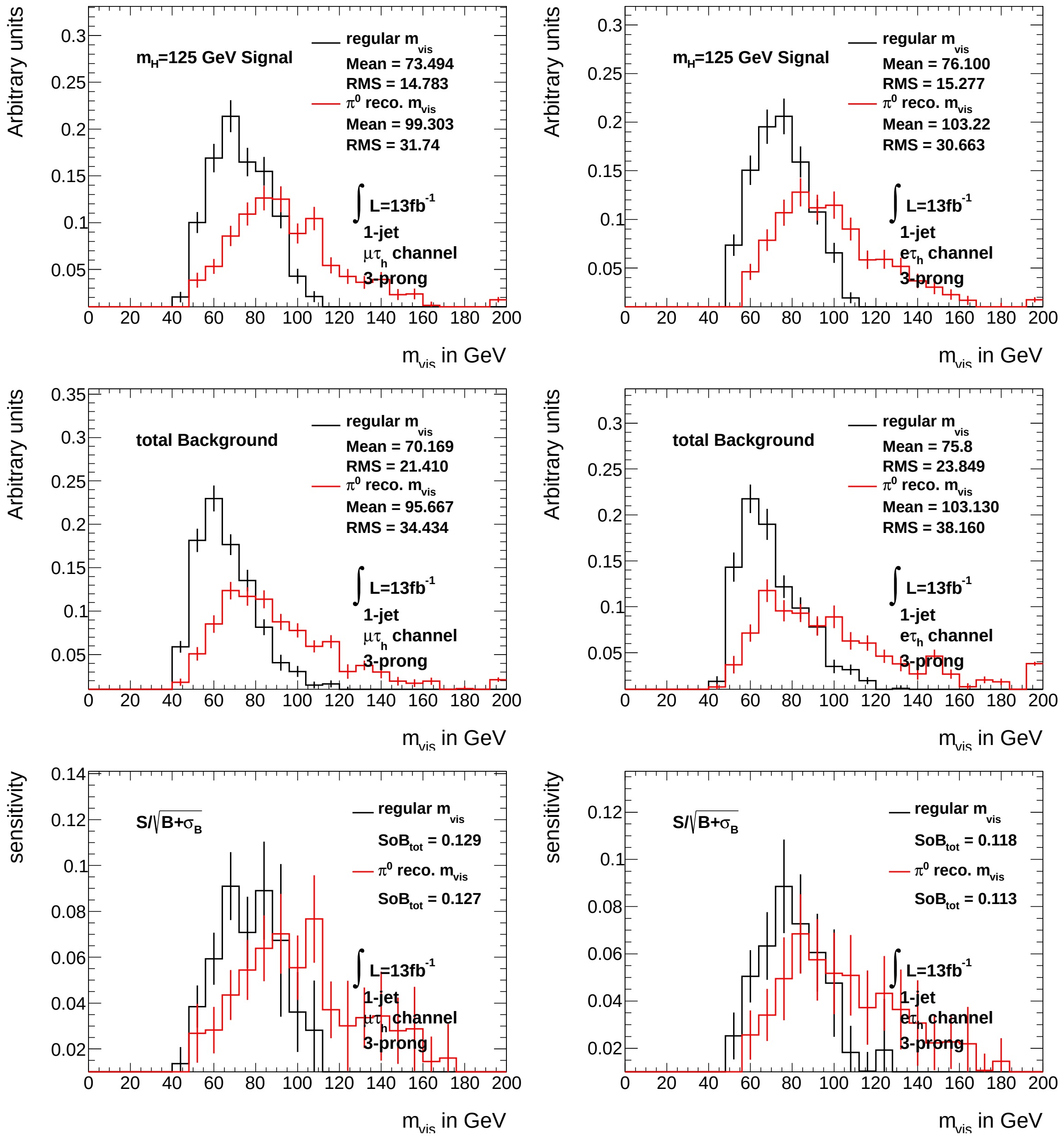

Figure B.7: Comparison of regular and with π^0 information reconstructed visible mass distributions of the $m_H = 125\,\text{GeV}$ Higgs-boson signal (top row) and the total background (middle row). The corresponding expected sensitivity distributions are shown in the bottom row. All histograms are for the 1-jet 3-prong category for the $\mu\tau_h$ channel (left column) and the $e\tau_h$ channel (right column).

C Sensitivity scans for $p_T(\tau)$

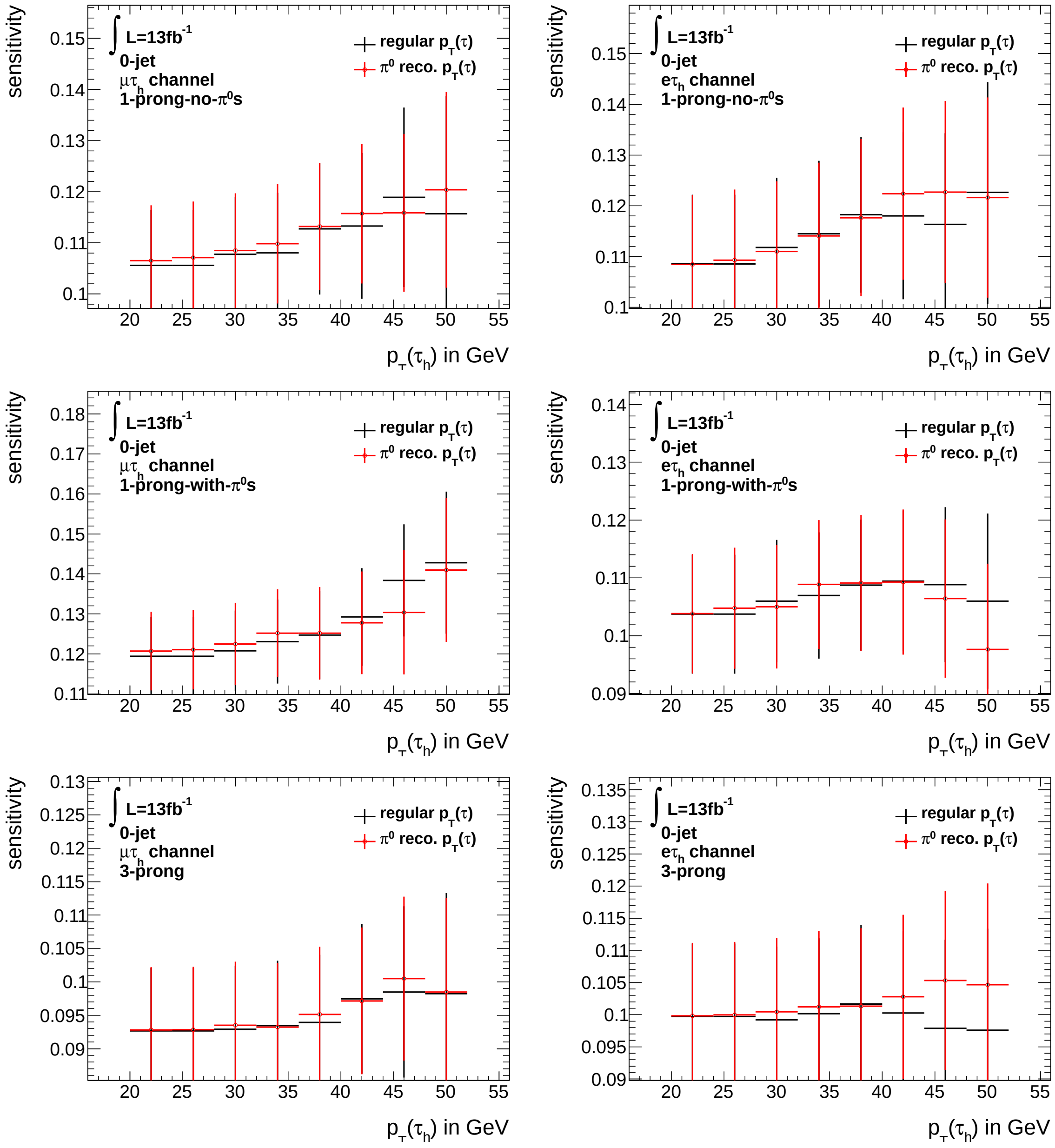

Figure C.1: Expected sensitivity scan for different cut values on $p_T(\tau)$ (black) and $p_T^{\pi^0\,\mathrm{reco}}(\tau)$ (red) for the 0-jet category. The plots shown correspond to $\mu\tau_h$ (left column) and $e\tau_h$ (right column); 1-prong-no-π^0s (first row); 1-prong-with-π^0s (second row); 3-prong (third row).

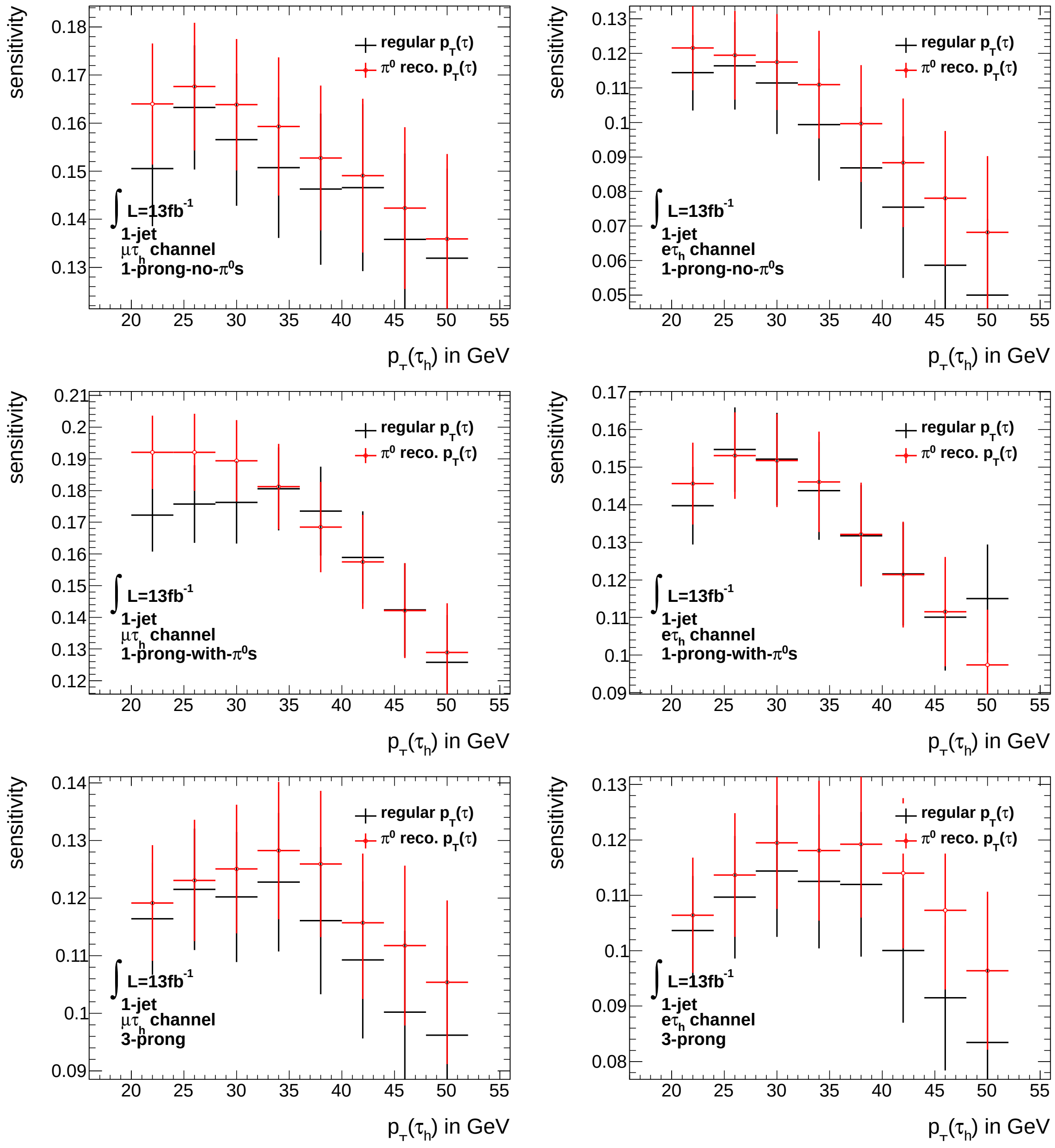

Figure C.2: Expected sensitivity scan for different cut values on $p_T(\tau)$ (black) and $p_T^{\pi^0\ \mathrm{reco}}(\tau)$ (red) for the 1-jet category. The plots shown correspond to $\mu\tau_h$ (left column) and $e\tau_h$ (right column); 1-prong-no-π^0s (first row); 1-prong-with-π^0s (second row); 3-prong (third row). The x-axis labels correspond to the cut on $p_T(\tau)$ that was applied on top of the selection.

List of Figures

List of Tables

Bibliography

[1] F. Halzen and A. D. Martin, *Quarks and Leptons: An Introductory Course in Modern Particle Physics*. Wiley, 1984.

[2] SNO Collaboration, Q. R. Ahmad *et al.*, *Measurement of the rate of* $\nu_e + d \to p + p + e^-$ *interactions produced by* ^8B *solar neutrinos at the Sudbury Neutrino Observatory*, Phys. Rev. Lett. **87** (2001) 071301, `arXiv:nucl-ex/0106015`.

[3] Super-Kamiokande Collaboration, Y. Fukuda *et al.*, *Evidence for oscillation of atmospheric neutrinos*, Phys.Rev.Lett. **81** (1998) 1562, `arXiv:hep-ex/9807003 [hep-ex]`.

[4] Particle Data Group, J. Beringer *et al.*, Phys. Rev. **D86** (010001 (2012)) .

[5] D. Griffiths, *Introduction to Elementary Particles*. Wiley, 1987.

[6] L. Álvarez-Gaumé and J. Ellis, *Eyes on a prize particle*, Nature Physics **7** (2011) , `http://www.nature.com/nphys/journal/v7/n1/full/nphys1874.html`.

[7] ATLAS Collaboration, G. Aad *et al.*, *Observation of a new particle in the search for the Standard Model Higgs boson with the ATLAS detector at the LHC.*, Phys.Lett. B **716** (2012) 24, `arXiv:1207.7214 [hep-ex]`.

[8] CMS Collaboration, S. Chatrchyan *et al.*, *Observation of a new boson at a mass of 125 GeV with the CMS experiment at the LHC.*, Phys.Lett. B **716** (2012) 59, `arXiv:1207.7235 [hep-ex]`.

[9] A. D. Martin, W. J. Stirling, R. S. Thorne, and G. Watt, *Parton distributions for the LHC*, Eur. Phys. J. **C63** (2009) 189, `arXiv:0901.0002 [hep-ph]`.

[10] J. M. Campbell, J. W. Huston, and W. J. Stirling, *Hard Interactions of Quarks and Gluons: A Primer for LHC Physics*, Rept. Prog. Phys. **70** (2007) 89, `arXiv:hep-ph/0611148`.

[11] T. Rias, `http://en.wikipedia.org/wiki/Higgs_boson`.

[12] LHC Higgs Cross Section Working Group, `https://twiki.cern.ch/twiki/bin/view/LHCPhysics/CrossSections`.

[13] A. Denner, S. Heinemeyer, I. Puljak, D. Rebuzzi, and M. Spira, *Standard Model Higgs-Boson Branching Ratios with Uncertainties*, Eur.Phy.J. **C71 1753** (2011) 32, `arXiv:1107.5909 [hep-ph]`.

[14] ALEPH, CDF, D0, DELPHI, L3, OPAL and SLD Collaborations and LEP, Tevatron and SLD Electroweak Working Groups, *Precision Electroweak Measurements and Constraints on the Standard Model*, `arXiv:1012.2367v2 [hep-ex]`.

[15] G. Cowan, K. Cranmer, E. Gross, and O. Vitells, *Asymptotic formulae for likelihood-based tests of new physics*, Eur.Phys.J. **C71 (2011)** (2011) 32, `arXiv:1007.1727 [hep-ex]`.

[16] CMS Collaboration, *Combination of Standard Model Higgs boson searches and measurements of the properties of the new boson with a mass near 125 GeV*, `https://twiki.cern.ch/twiki/bin/view/CMSPublic/Hig12045TWiki`, Nov 2012.

[17] ATLAS Collaboration, *Updated ATLAS results on the signal strength of the Higgs-like boson for decays into WW and heavy fermion final states*, `https://cdsweb.cern.ch/record/1494183`, 16 Nov 2012.

[18] ATLAS Collaboration, G. Aad *et al.*, *The ATLAS Experiment at the CERN Large Hadron Collider*, JINST **3** (2008) S08003.

[19] ATLAS Collaboration, G. Aad *et al.*, *Expected Performance of the ATLAS Experiment - Detector, Trigger and Physics*, `arXiv:0901.0512 [hep-ex]`.

[20] ATLAS Collaboration, *Search for the Standard Model Higgs boson in $H \rightarrow \tau^+\tau^-$ decays in proton-proton collisions with the ATLAS detector*, ATLAS note: ATLAS-CONF-2012-160, 13 Nov 2012.

[21] ATLAS Collaboration, *Reconstruction, Energy Calibration, and Identification of Hadronically Decaying Tau Leptons*, ATLAS note: ATLAS-CONF-2011-077, 1 August 2011.

[22] ATLAS Collaboration, *Performance of the Reconstruction and Identification of Hadronic τ Decays in ATLAS with 2011 Data*, ATLAS note: ATLAS-CONF-2012-142, 17 October 2012.

[23] ATLAS Collaboration, T. Carli and A. Schwarzman, *Jet energy measurement with the ATLAS detector in proton-proton collisions at $\sqrt{s}$ = 7TeV taken in 2010*, ATLAS note: ATL-COM-PHYS-2011-978, 2011.

[24] G. Aad *et al.*, *Electron performance measurements with the ATLAS detector using the 2010 LHC proton-proton collision data*, Eur.Phy.J. **C 72 1909** (2012) 45, `arXiv:1110.3174 [hep-ex]`.

[25] ATLAS Collaboration, G. Aad *et al.*, *Muon Momentum Resolution in First Pass Reconstruction of pp Collision Data Recorded by ATLAS in 2010.*

[26] ATLAS Collaboration, G. Aad *et al.*, *Jet energy scale and its systematic uncertainty in proton-proton collisions at sqrt(s)=7 TeV in ATLAS 2010 data.*

[27] ATLAS Collaboration, G. Aad *et al.*, *Determination of the tau energy scale and the associated systematic uncertainty in proton-proton collisions at sqrts= = 7 TeV with the ATLAS detector at the LHC in 2011.*

[28] ATLAS Collaboration, G. Aad *et al.*, *Performance of Missing Transverse Momentum Reconstruction in ATLAS with Proton-Proton Collisions at sqrt(s)=7 TeV.*

[29] *Cluster-based pi0 reconstruction*, `https://indico.cern.ch/contributionDisplay.py?sessionId=1&contribId=56&confId=172493`, 21 Mar 2012.

[30] π^0 *reconstruction performance*, `https://indico.cern.ch/getFile.py/access?contribId=1&resId=0&materialId=slides&confId=206197`, 4 Sep 2012.

[31] M. Trottier-McDonald, *Private communication.*

[32] P. Malecki, *Private communication.*

[33] ATLAS Collaboration, A. Andreazza *et al.*, *Search for the Standard Model Higgs Boson decaying to di-tau pair with a lepton and a hadronic tau in the final state with the ATLAS Detector in 8 TeV Proton-Proton Collisions*, ATLAS note: ATL-COM-PHYS-2012-1201, 2 Nov 2012.

[34] ATLAS Collaboration, S. Banerjee *et al.*, *Re-optimized Search for Standard Model* $H \rightarrow \tau^+\tau^- \rightarrow l\tau_h$ *with the ATLAS Detector in 7 TeV Proton-Proton Collisions*, ATLAS note: ATL-COM-PHYS-2012-1087, 24 Oct 2012.

[35] I. W. Stewart and F. J. Tackmann, *Theory Uncertainties for Higgs and Other Searches Using Jet Bins*, Phys.Rev. **D85 (2012)** (2012) 13, `arXiv:1107.2117 [hep-ph]`.

[36] G. Cowan, *Discovery sensitivity for a counting experiment with background uncertainty*, `http://www.pp.rhul.ac.uk/~cowan/stat/notes/medsigNote.pdf`, May 2012.

Erklärung der Selbstständigkeit

Hiermit versichere ich, dass ich die vorliegende Diplomarbeit selbstständig verfasst und keine anderen als die angegebenen Quellen und Hilfsmittel verwendet habe.

Freiburg, den _______________ __________________________
Johanna Nagel